NATIONAL TECHNICAL UNIVERSITY OF ATHENS
SCHOOL OF NAVAL ARCHITECTURE AND MARINE ENGINEERING
DIVISION OF MARINE ENGINEERING

DIPLOMA THESIS

KOUKOULOPOULOS ELEFTHERIOS

Software development for the solution of hydrodynamic lubrication problems in piston rings of two-stroke marine Diesel engines

Thesis Committee:

Supervisor:	**C. Papadopoulos, Assistant Professor NTUA**
Members:	**N. Kyrtatos, Professor NTUA**
	L. Kaiktsis, Associate Professor NTUA

Athens, March 2014

Acknowledgements

The present thesis is the final milestone of my studies in the School of Naval Architecture and Marine Engineering of the National Technical University of Athens (NTUA), and I would like to thank all my colleagues and professors with whom I shared these last years.

First of all, I would like to thank my family for their efforts and sacrifices to become a better person, and for supporting me throughout my studies. I would also like to offer my sincerest gratitude to my supervisor, Dr. Christos Papadopoulos, for developing a very good collaboration; without his motivation this thesis would not even have the half of the present content.

Furthermore, I would like to thank my fellow student and friend Mr. Leonidas Raptis for his decisive contribution and support during the whole year of work on the present study, and for all the great moments we have shared.

Many thanks are also owed to Mr. Panagiotis Kontoulis, Ph.D. candidate at NTUA, for his practical assistance in finding the details of the marine engine that was used in the present work.

Abstract

The propulsion system of conventional ships consists of one or more main engines (usually two- or four- stroke Diesel engines), coupled directly or by means of a reduction gearbox to the propeller. The shafting system of a ship transmits the main engine output power to the propeller, and, also, transmits the propeller thrust to the ship hull. Friction is a major cause of energy losses in marine propulsion systems.

In Diesel engines, substantial friction losses are present at the piston ring assembly, at the guide shoe bearings, at the main bearings and at the connecting rod bearings. Overall, approximately 3% of fuel energy is lost to friction; the corresponding cost is substantial, taken into account that the annual fuel cost of a typical cargo vessel is approximately 80-90% of its total running cost.

The piston rings of a Diesel engine are circular metallic rings, fitted into grooves at the outer diameter of the engine pistons. They are mainly used to isolate the combustion chamber from the crankcase. This is accomplished by development of hydrodynamic pressure in a thin film of oil that separates the ring face from the cylinder liner. Pressure is generated in the film due to the piston reciprocating motion. Friction losses in the piston ring pack correspond to approximately 26% of the total engine mechanical losses.

The aims of the present study are twofold: (a) to develop software tools for the solution of hydrodynamic lubrication problems in piston rings under transient loading conditions, and (b) to apply those tools for studying the performance of piston rings in large two-stroke marine Diesel engines.

Piston rings operate mainly in the regime of hydrodynamic lubrication, which is governed by the Reynolds equation. The tools developed in the course of the present study are capable of solving the Reynolds equation with two different types of boundary conditions. The first one is the simple Reynolds boundary condition, which provides accurate prediction of the lubricant pressure in the active film region, however, mass conservation is violated in the cavitating region. To alleviate this drawback, the Elrod-Adams mass conserving model is implemented, which predicts accurately the lubricant behavior in both the active and the cavitating regions of the ring. The tools have been properly extended to account for piston ring surface with hydrophobic characteristics. Numerical solution of the differential equations is performed using the Finite Difference Method (FDM), and the resulting calculations have been validated against results published in the literature.

The tools developed have been applied to compute the performance characteristics of the piston rings of a typical large two-stroke marine Diesel engine. Two loading conditions have been considered, corresponding to power output equal to 100% and 25% of the engine MCR. At first, calculations have been performed for a reference ring design, and a parametric analysis has been conducted to identify the effect of the main design parameters of the ring (face curvature / offset, lubricant properties) on its performance characteristics. Next, regions

of the ring face have been assumed to have undergone surface treatment in the form of hydrophobicity or artificial surface texturing. The effect of those surface treatment technologies on the reference design has been assessed, and a detailed parametric analysis has been performed to identify optimum design parameter values.

Σύνοψη

Το σύστημα πρόωσης συμβατικών πλοίων αποτελείται από μία ή περισσότερες κύριες μηχανές (συνήθως δίχρονους ή τετράχρονους κινητήρες Diesel), συζευγμένη/ες απευθείας ή μέσω μειωτήρα στροφών με την έλικα. Το αξονικό σύστημα του πλοίου μεταδίδει την περιστροφική ισχύ της κύριας μηχανής στην έλικα, και την ώση της έλικας στη γάστρα του πλοίου. Η τριβή αποτελεί σημαντική αιτία απωλειών ενέργειας στα συστήματα πρόωσης πλοίου.

Στους κινητήρες Diesel, σημαντικές απώλειες τριβής παρουσιάζονται στα ελατήρια του εμβόλου, στα έδρανα του σταυρού, στα έδρανα βάσης και στα έδρανα του διωστήρα. Συνολικά, περίπου το 3% της ενέργειας του καυσίμου χάνεται λόγω της τριβής. Το αντίστοιχο κόστος είναι σημαντικό, λαμβάνοντας υπόψη ότι το ετήσιο κόστος καυσίμου ενός τυπικού πλοίου ανέρχεται περίπου σε 80-90% του συνολικού κόστους λειτουργίας του.

Τα ελατήρια εμβόλου ενός κινητήρα Diesel είναι κυκλικά μεταλλικά δαχτυλίδια, που τοποθετούνται σε αύλακες στην εξωτερική διάμετρο των εμβόλων του κινητήρα. Χρησιμοποιούνται κυρίως προκειμένου να απομονώσουν τον θάλαμο καύσης από τον στροφαλοθάλαμο. Αυτό επιτυγχάνεται με την ανάπτυξη υδροδυναμικής πίεσης σε ένα λεπτό στρώμα λιπαντικού που διαχωρίζει την επιφάνεια του ελατηρίου από το χιτώνιο του κυλίνδρου. Πίεση αναπτύσσεται στο φιλμ, λόγω της παλινδρομικής κίνησης του εμβόλου. Οι απώλειες τριβής στα ελατήρια εμβόλου αντιστοιχούν στο 26% των συνολικών μηχανικών απωλειών.

Ο σκοπός της παρούσας διπλωματικής εργασίας είναι διττός: (α) η ανάπτυξη υπολογιστικών εργαλείων για την επίλυση του προβλήματος της υδροδυναμικής λίπανσης σε ελατήρια εμβόλου υπό χρονικά μεταβαλλόμενες συνθήκες φόρτισης, και (β) η εφαρμογή τους για τη μελέτη της απόδοσης των ελατηρίων εμβόλου σε μεγάλους δίχρονους ναυτικούς κινητήρες Diesel.

Τα ελατήρια εμβόλου λειτουργούν στην περιοχή της υδροδυναμικής λίπανσης, η οποία διέπεται από την εξίσωση Reynolds. Τα υπολογιστικά εργαλεία που αναπτύχθηκαν στο πλαίσιο της παρούσας εργασίας επιλύουν την εξίσωση Reynolds με δύο διαφορετικές οριακές συνθήκες. Η πρώτη είναι η απλή οριακή συνθήκη Reynolds, η οποία παρέχει ακριβή πρόβλεψη της πίεσης του λιπαντικού στην ενεργό περιοχή του φιλμ, παραβιάζοντας όμως τη διατήρησης της μάζας στην περιοχή της σπηλαίωσης. Προκειμένου να αμβλυνθεί αυτό το μειονέκτημα, χρησιμοποιήθηκε το μοντέλο διατήρησης της μάζας των Elrod-Adams, το οποίο προβλέπει με ακρίβεια τη συμπεριφορά του λιπαντικού και στην ενεργό αλλά και στη σπηλαιούμενη περιοχή του ελατηρίου. Εν συνεχεία, τα παραπάνω υπολογιστικά μοντέλα επεκτάθηκαν κατάλληλα ώστε να μπορούν να χρησιμοποιηθούν σε περιπτώσεις που η επιφάνεια του ελατηρίου έχει υδροφοβικές ιδιότητες. Οι προκύπτουσες διαφορικές εξισώσεις επιλύθηκαν με τη μέθοδο των πεπερασμένων διαφορών (Finite Difference Method - FDM), και οι υπολογισμοί επικυρώθηκαν με αποτελέσματα της διεθνούς βιβλιογραφίας.

Το αναπτυχθέν λογισμικό εφαρμόστηκε για τον υπολογισμό των χαρακτηριστικών λειτουργίας των ελατηρίων ενός τυπικού μεγάλου δίχρονου ναυτικού κινητήρα Diesel. Θεωρήθηκαν δύο καταστάσεις φόρτισης που αντιστοιχούν σε αποδιδόμενη ισχύ ίση με 100% και 25% της μέγιστης συνεχούς ισχύος του κινητήρα. Αρχικά, έγιναν υπολογισμοί για ένα ελατήριο αναφοράς, και διεξήχθη παραμετρική ανάλυση προκειμένου να προσδιοριστεί η επίδραση των βασικών σχεδιαστικών παραμέτρων του ελατηρίου (καμπυλότητα / εκκεντρότητα, ιδιότητες του λιπαντικού κ.λπ.) στα λειτουργικά χαρακτηριστικά του. Στη συνέχεια, θεωρήθηκε ότι ορισμένες περιοχές του ελατηρίου έχουν υποστεί επιφανειακή κατεργασία με τη μορφή υδροφοβικότητας ή τεχνητής τραχύτητας. Κατ' αρχάς, αξιολογήθηκε η επίδραση αυτών των κατεργασιών στη συμπεριφορά του ελατηρίου, και ακολούθησε λεπτομερής παραμετρική ανάλυση για τον προσδιορισμό των βέλτιστων τιμών των σχεδιαστικών παραμέτρων.

Table of Contents

Acknowledgements 2
Abstract 3
Σύνοψη 5
Nomenclature 10
List of Figures 12
List of Tables 17
1. Introduction 18
1.1 The significance of tribology in Diesel engines 18
1.2 Literature review-structure 18
2. Piston rings - theoretical approach 21
2.1 Diesel engine piston rings *(Based on [18]-[21])* 21
2.1.1 Piston ring main functions 21
2.1.2 Piston ring categories 22
2.1.3 Piston ring materials 24
2.1.4 Comparison between two-stroke and four-stroke Diesel engines concerning the lubrication method 24
2.1.5 Ways of lubrication, oils and material wear 25
2.2 Hydrodynamic lubrication *(based on [3])* 26
2.2.1 Introduction 26
2.2.2 Simplifying assumptions 27
2.2.3 Equilibrium of a finite volume of fluid 27
2.2.4 Continuity of flow in a column of finite width 30
2.2.5 Assumption of constant density 32
2.2.6 Performance parameters of piston rings 33
2.2.7 Boundary conditions 34
2.3 The problem of cavitation at piston rings *(based on [3], [22]-[24])* 36
2.3.1 Modification of Reynolds equation in the cavitation region 36
2.4 Hydrophobicity 37
2.4.1 The phenomenon of hydrophobicity 37
2.4.2 Mathematical equations for surfaces with slip properties 39
2.5 Artificial texturing 41

3. Numerical solution of Reynolds equation for hydrodynamic lubrication of piston ring . 43
3.1 Finite difference method . 43
3.2 Solution algorithm . 46
3.3 Algorithm solvers . 50
3.3.1 Reynolds equation with the Elrod-Adams mass conservation model . 51
3.3.2 Reynolds equation for hydrophobic surfaces with the Elrod-Adams mass conservation algorithm . 53
3.4 Validation of the solution algorithms . 53
3.4.1 Reynolds equation . 53
3.4.2 Reynolds equation with the Elrod-Adams cavitation model . 54
3.4.3 Reynolds equation for hydrophobic surfaces . 60
4. Computational Results . 66
4.1 Introduction . 66
4.2 Pressure and piston speed diagrams . 68
4.3 Reference case . 70
4.3.1 Mesh study . 70
4.3.2 Study of lubricant bulk modulus . 71
4.3.3 Comparison of computation with the classic Reynolds equation and the Reynolds equation with the Elrod-Adams mass conservation model . 73
4.3.4 Effect of time derivatives (squeeze film terms) . 74
4.3.5 Comparison of different engine cycles . 75
4.3.6 Reference piston ring design - 100% engine load . 76
4.3.7 Reference piston ring design - 25% engine load . 78
4.4 Parametric analysis of geometric and operational parameters . 80
4.4.1 Crown height . 81
4.4.2 Offset . 82
4.4.3 Pretension force . 84
4.4.4 Viscosity . 85
4.4.5 Pressure of area between first and second piston ring . 86
4.4.6 Composite roughness . 87
4.5 Effect of hydrophobicity at part of the ring surface . 88
4.5.1 Non-dimensional slip length, b* . 90
4.5.2 Bottom slip region: Variation of slip start location . 91
4.5.3 Bottom slip region: Variation of slip end location . 92

4.5.4 Top slip region: Variation of slip start location 93
4.5.5 Top slip region: Variation of slip end location 94
4.5.6 Optimal design with hydrophobicity at the bottom and the top part of the piston ring 95
4.6 Artificial surface texturing 99
4.6.1 Bottom textured region: Variation of texture start location 101
4.6.2 Bottom textured region: Variation of texture end location 102
4.6.3 Top textured region: Variation of texture start location 103
4.6.4 Top textured region: Variation of texturing end location 104
4.6.5 Texture depth 105
4.6.6 Optimal design with artificial surface texturing at the bottom and at the top part of the piston ring 107
5. Conclusions and future work 111
5.1 Conclusions 111
5.2 Future work 112
5. Literature 113
Appendix A 115
Appendix B 122

Nomenclature

a	Slip proportionality factor [m/ Pa·s]: $\alpha=b/\eta$
b	Ring width [m]
B	Bore diameter, [m]
b^*	Non-dimensional slip length: $b^*=b_s/r$
b_s	Slip length [m]
c	Crown height [m]
CA	Crank angle [degrees]
d_{cl}	Texture cell length [m]
$d_{density}$	Texture density
d_{depth}	Dimple depth [m]
d_{length}	Dimple length [m]
d_{num}	Number of dimples
E	Young's modulus of elasticity [Pa]
F	Friction force [N]
F_{ext}	Sum of external forces acting on the ring [N]
g	Cavitating factor
h	Film thickness [m]
h_{max}	Maximum film thickness [m]
h_{min}	Minimum film thickness [m]
l	Ring length along the peripheral [m]
l_s	Non-dimensional hydrophobic length, $l_s=L_s/b$
L_s	Ring hydrophobic length [m]
m	Grid points along the y direction
N	Rotational speed [RPM]
n	Grid points along the x direction
nc	Number of engine cycles
o	Offset [m]
p	Pressure of piston ring [Pa]
p_{1-2}	Pressure between the first and second compression rings [Pa]
P_{bk}	Force acting on the back face of ring from combustion gases[N]
p_c	Cavitation pressure [Pa]
p_{ch}	Pressure in the combustion chamber [Pa]
P_{el}	Pretension force acting against the liner [N]
PL	Power loss [W]
p_{max}	Maximum pressure of piston ring [Pa]
R	Rod length [m]
r	Composite roughness [m]
S	Engine stroke [m]
SBe	Bottom hydrophobic region: Non-dimensional x coordinate of slip end location

SBs	Bottom hydrophobic region: Non-dimensional x coordinate of slip start location
STe	Top hydrophobic region: Non-dimensional x coordinate of slip end location
STs	Top hydrophobic region: Non-dimensional x coordinate of slip start location
t	Time [s]
T	Tangential tension force of piston ring [N]
TB_e	Bottom textured region: Non-dimensional x coordinate of texture end location
TB_s	Bottom textured region: Non-dimensional x coordinate of texture start location
TT_e	Top textured region: Non-dimensional x coordinate of texture end location
TT_s	Top textured region: Non-dimensional x coordinate of texture start location
tp	Time points
U	Piston speed [m/s]
u	Fluid velocity in the x direction [m/s]
v	Fluid velocity in the y direction [m/s]
W	Load carrying capacity of fluid [N]
w	Fluid velocity in the z direction [m/s]
x	Direction along the piston ring profile (streamwise direction)
y	Direction along the piston ring circumference (spanwise direction)
z	Direction along the film thickness (crossflow direction)
β	Lubricant bulk modulus [Pa]
η	Lubricant viscosity [Pa·s]
θ	Lubricating film fraction
λ	Ring gap in the peripheral direction [m]
ρ	Lubricant density [kg/m^3]
τ_c	Critical shear stress [Pa]
τ	Shear stress [Pa]

List of Figures

Fig. 1. Piston and its components [19]. 21
Fig. 2. Gas forces acting on a piston ring [18]. 22
Fig. 3. (a) Compression and (b) compression-oil scrap piston ring profile geometries [20]. 23
Fig. 4. Oil ring profile geometries [20]. 24
Fig. 5. Cylinder bore microstructure where the black marks constitute the graphite flake [27]. 24
Fig. 6. Hydrodynamic pressure distribution between the inclined surfaces of a simple slider [3]. 26
Fig. 7. Force equilibrium of a finite volume of fluid. 27
Fig. 8. Profiles of the three separate velocity terms at the lubricant inflow region. 29
Fig. 9. Continuity of flow in a column of fluid. 31
Fig. 10. Sketch of a typical piston ring geometry. 33
Fig. 11. Sketch of a simple slider. 34
Fig. 12. Solution of the Reynolds equation with Full-Sommerfeld boundary conditions. 34
Fig. 13. Solution of the Reynolds equation with Half-Sommerfeld boundary conditions. 35
Fig. 14. Solution of the Reynolds equation with Reynolds boundary conditions. 35
Fig. 15. Liquid and gas streamers in the cavitation region. 36
Fig. 16. Measurement of contact angle of a liquid drop [30]. 37
Fig. 17. Liquid drops on a lotus leaf [30]. 37
Fig. 18. Lotus leaf under the microscope [30]. 37
Fig. 20. Velocity profiles: (a) no-slip condition, (b) slip conditions with slip length b_s. 38
Fig. 21. Velocity parabolic profile in the y-direction caused from the pressure derivative. 40
Fig. 22. Example of textured piston rings [29]. 42
Fig. 23. Sketch of a piston ring segment. 43
Fig. 24. Discretization details of the lubricant domain separating the ring from the cylinder liner. 44
Fig. 25. Transient hydrodynamic lubrication in piston rings: solution algorithm. 48
Fig. 26. (a) Minimum film thickness, (b) power loss, and (c) friction force against crank angle: Comparison between the present results, and those of Jeng et al. [4]. 54
Fig. 27. Converging-diverging slider with zero pressure at the slider boundaries: Film thickness shape and corresponding pressure distribution calculations by (a) Giacopini et al. [11], (b) the present Reynolds equation solver and (c) the present solver of the Reynolds equation with the Elrod-Adams mass conservation model. 55
Fig. 28. Converging-diverging slider with 1 MPa pressure at the slider boundaries: Film thickness shape and corresponding pressure distribution calculations by (a) Giacopini et al. [11], (b) the present Reynolds equation solver and (c) the present solver of the Reynolds equation with the Elrod-Adams mass conservation model. 56
Fig. 29. Diverging-converging slider with 1 MPa pressure at the slider boundaries: Film thickness shape and corresponding pressure distribution calculations by (a) Giacopini et al. [11], (b) the present Reynolds equation solver and (c) the present solver of the Reynolds equation with the Elrod-Adams mass conservation model. 56

Fig. 30. Sketch of parallel slider with a single microtexture pocket.....57
Fig. 31. Parallel slider with a single pocket and 0.1 MPa pressure at the boundaries: Film thickness shape and corresponding computed pressure distribution by (a) the present Reynolds equation solver, with the Elrod-Adams algorithm, and (b) Giacopini et al. [11]. ...58
Fig. 32. Parallel slider with a single pocket and 0.1 MPa pressure at the boundaries: Pocket depth, $h_{max}=2 \cdot h_{min}$: Film thickness shape and corresponding computed pressure distribution by (a) the present Reynolds equation solver, with the Elrod-Adams algorithm, and (b) Xiong et al. [17]. 59
Fig. 33. Parallel slider with a single pocket and 0.1 MPa pressure at the boundaries: Pocket depth, $h_{max}=4 \cdot h_{min}$: Film thickness shape and corresponding computed pressure distribution by (a) the present Reynolds equation solver, with the Elrod-Adams algorithm, and (b) Xiong et al. [17]. 59
Fig. 34. Streamwise pressure distribution of the slider: comparison between result of the present work and those of Pavlioglou et al [13]. The considered slider is parallel with hydrophobicity at 85% of the slider length, starting from inflow.....61
Fig. 35. Sketch of the two three-dimensional sliders with hydrophobicity at part of the stator, studied by GuoJun et al. [14]. 61
Fig. 36. Non-dimensional load capacity W^* against convergence ratio k for the cases depicted in the embodied sketches; comparison between the results of present study and those of GuoJun et al. [14].....62
Fig. 37. Non-dimensional friction force F* against convergence ratio k for the cases depicted in the embodied sketches; comparison between the results of present study and those of GuoJun et al. [14].....62
Fig. 38. Partially hydrophobic 3-D slider: Maximum pressure versus convergence ratio, for different values of non-dimensional slip length b^*. Comparisons between the computations of the present Reynolds equation solver and those with ANSYS CFX. 63
Fig. 39. Partially hydrophobic 3-D slider: Load capacity versus convergence ratio, for different values of non-dimensional slip length b^*. Comparisons between the computations of the present Reynolds equation solver and those with ANSYS CFX. 64
Fig. 40. Partially hydrophobic 3-D slider: Non-dimensional load carrying capacity versus convergence ratio. Comparison between CFD results and results of the present Reynolds equation solver. 64
Fig. 41. Partially hydrophobic 3-D slider: Non-dimensional friction force versus convergence ratio. Comparison between CFD results and results of the present Reynolds equation solver. 65
Fig. 42. Sketch of the first (top) compression piston ring. 67
Fig. 43. Sketch of a piston ring and radial load from the liner wall. 68
Fig. 44. Equilibrium of forces at half of the piston ring. 68
Fig. 45. Combustion chamber pressure versus crank angle for engine loads of 100% and 25%. 69
Fig. 46. Pressure in the space between the first and second piston rings versus crank angle for engine loads of 100% and 25%.....69
Fig. 47. Piston speed versus crank angle at 105 RPM (100% load) and 66.1 RPM (25% load). 70

Fig. 48. Mesh study of the plain piston ring at 100% engine load. The parameters evaluated are: minimum film thickness 'h_{min}', its percentage difference from the maximum grid size, friction force 'F', and maximum pressure 'p_{max}'. 71
Fig. 49. Pressure distribution at CA=450^o, for different values of bulk modulus, 'β'. 72
Fig. 50. Minimum film thickness 'h_{min}' versus crank angle for different values of bulk modulus, 'β'. 72
Fig. 51. (a) Minimum film thickness, (b) power loss, (c) maximum pressure and (d) percentage of cavitation area, against crank angle, for the two different solution algorithms. 73
Fig. 52. Pressure distribution for CA=405^o (downstroke) and CA=660^o (upstroke): Calculations with the classic Reynolds equation and the Elrod-Adams mass conservation model. 74
Fig. 53. Pressure and film thickness distribution at CA=539^o (approximately zero sliding velocity). Effect of the squeeze film term on the solution. 74
Fig. 54. Minimum film thickness versus crank angle: Comparison between simulation results corresponding to the first and the fourth engine cycle, and simulation results corresponding to the second and fourth engine cycle. 75
Fig. 55. Reference piston ring design, 100% engine load, 105 RPM: Operational indices versus engine crank angle. 77
Fig. 56. Reference piston ring design, 100% engine load, 105 RPM: Distributions of pressure 'p', film thickness 'h' and film fraction 'θ' for crank angle values: (a) CA=384^o, (b) CA=451^o, (c) CA=540^o, (d) CA=661^o. 78
Fig. 57. Reference piston ring design, 25% engine load, 66.1 RPM: Operational indices versus engine crank angle. 79
Fig. 58. Reference piston ring design, 25% engine load, 66.1 RPM: Distributions of pressure 'p', film thickness 'h' and film fraction 'θ' for crank angle values: (a) CA=384^o, (b) CA=451^o, (c) CA=540^o, (d) CA=661^o 80
Fig. 59. (a) Minimum film thickness, (b) power loss, (c) maximum pressure and (d) percentage of cavitation area, against crank angle, for different crown height values. 81
Fig. 60. (a) Minimum film thickness, (b) power loss, (c) maximum pressure and (d) percentage of cavitation area, against crank angle, for different positive offset values. 82
Fig. 61. (a) Minimum film thickness, (b) power loss, (c) maximum pressure and (d) percentage of cavitation area, against crank angle, for different negative offset values. 83
Fig. 62. (a) Minimum film thickness, (b) power loss, (c) maximum pressure and (d) percentage of cavitation area, against crank angle, for different ring pretension force values. 84
Fig. 63. (a) Minimum film thickness, (b) power loss, (c) maximum pressure and (d) percentage of cavitation area, against crank angle, for different values of viscosity. 85
Fig. 64. (a) Minimum film thickness, (b) power loss, (c) maximum pressure and (d) percentage of cavitation area, against crank angle, for different values of pressure between first and second piston ring. 86
Fig. 65. (a) Minimum film thickness against crank angle, for different values of pressure between first and second piston ring, (b) zoom of 20 first crank angles of engine cycle 87

Fig. 66. Piston ring face profile with the regions of hydrophobicity highlighted; the four dots mark the start and end of each hydrophobic area; SB_s: start of bottom slip region, SB_e: end of bottom slip region, ST_s: start of top slip region, ST_e: end of top slip region 88
Fig. 67. (a) Minimum film thickness, (b) power loss, (c) maximum pressure and (d) percentage of cavitation area for 100% engine load, against crank angle, for the reference piston ring, and the hydrophobic ring with parameters those of Table 5. 89
Fig. 68. (a) Minimum film thickness, (b) power loss, (c) maximum pressure and (d) percentage of cavitation area, against crank angle, for different values of non-dimensional slip length, b^* 90
Fig. 69. (a) Minimum film thickness, (b) power loss, (c) maximum pressure and (d) percentage of cavitation area, against crank angle, for different values of start of bottom slip region, SB_s 91
Fig. 70. (a) Minimum film thickness, (b) power loss, (c) maximum pressure and (d) percentage of cavitation area, against crank angle, for different values of the end of bottom slip region, SB_e. 92
Fig. 71. (a) Minimum film thickness, (b) power loss, (c) maximum pressure and (d) percentage of cavitation area, against crank angle, for different values of the start of top slip region, ST_s. 93
Fig. 72. (a) Minimum film thickness, (b) power loss, (c) maximum pressure and (d) percentage of cavitation area, against crank angle, for different values of end of top slip region, ST_e 94
Fig. 73. (a) Minimum film thickness, (b) power loss, (c) maximum pressure and (d) percentage of cavitation area against crank angle, for 100% engine load: Comparison between the reference case (no-slip) piston ring design and the optimal hydrophobic design. 95
Fig. 74. Operational indices of the optimal hydrophobic case against crank angle for 100% engine load and 105 RPM; hydrophobic region from 0%-30% and 70%-100% and non-dimensional slip length $b^*=10$. 96
Fig. 75. Optimal hydrophobic design: Distributions of pressure,p , film thickness, h , and film fraction, θ, at crank angles (a) CA=384^o, (b) CA=451^o, (c) CA=540^o and (d) CA=661^o. Here, 100% load is assumed. 97
Fig. 76. (a) Minimum film thickness, (b) power loss, (c) maximum pressure and (d) percentage of cavitation area against crank angle, for 25% engine load: Comparison between the reference (no-slip) piston ring design and the optimal hydrophobic design. 98
Fig. 77. Piston ring face profile including the geometry of the textured regions; the four dots mark the start and end of each hydrophobic area; TB_s: start of bottom textured region, TB_e: end of bottom textured region, TT_s: start of top textured region, TT_e: end of top textured region, d_{depth}: dimple depth, d_{cl}: length of each dimple cell, d_{length}: length of each dimple. .. 100
Fig. 78. (a) Minimum film thickness, (b) power loss, (c) maximum pressure and (d) percentage of cavitation area for 100% engine load, against crank angle, for the reference piston ring, and for the textured ring with parameters those of Table 6. 101
Fig. 79. (a) Minimum film thickness, (b) power loss, (c) maximum pressure and (d) percentage of cavitation area, against crank angle, for different values of the start of bottom textured region, TB_s. 102

Fig. 80. (a) Minimum film thickness, (b) power loss, (c) maximum pressure and (d) percentage of cavitation area, against crank angle, for different values of the end of bottom textured region, TB_e. 103
Fig. 81. (a) Minimum film thickness, (b) power loss, (c) maximum pressure and (d) percentage of cavitation area, against crank angle, for different values of the start of top textured region, TT_s. 104
Fig. 82. (a) Minimum film thickness, (b) power loss, (c) maximum pressure and (d) percentage of cavitation area, against crank angle, for different values of the end of top textured region, TT_e. 105
Fig. 83. (a) Minimum film thickness, (b) power loss, (c) maximum pressure and (d) percentage of cavitation area against crank angle, for different values of dimple depth. Here, the optimal textured ring is considered. 106
Fig. 84. (a) Minimum film thickness, (b) power loss, (c) maximum pressure and (d) percentage of cavitation area against crank angle, for 100% engine load: Comparison between the reference case (untextured) piston ring and the optimal textured design. 107
Fig. 85. Operational indices of the optimal texturing case against crank angle for 100% engine load and 105 RPM; textured region from 0%-30% and 70%-100% of the total ring length, and a dimple depth value of 10 μm. 108
Fig. 86. Optimal textured ring design: Distributions of pressure, p, film thickness, h, and film fraction, θ, at crank angle values (a) CA=384^o, (b) CA=451^o, (c) CA=540^o and (d) CA=661^o. Here, 100% engine load is assumed. 109
Fig. 87. (a) Minimum film thickness, (b) power loss, (c) maximum pressure and (d) percentage of cavitation area for against crank angle for 25% engine load: Comparison between the reference (untextured) piston ring and the optimally textured design. 110
Fig. 88. Velocity parabolic profile caused from the pressure derivative 118

List of Tables

Table 1. Geometrical and operational characteristics of the slider of Fig. 29. 57
Table 2. Geometric and operational parameters of the slider studied by Xiong et al. [17] 60
Table 3. Geometric and operational characteristics of the reference engine 66
Table 4. Geometric parameters and mechanical characteristics of the reference piston ring of the present study. 67
Table 5. Piston ring with hydrophobicity. Parameters controlling the location and extent of the hydrophobic regions of Fig. 65. 89
Table 6. Piston ring with artificial surface texturing: Parameters controlling the location and extent of the textured regions of Fig. 76, as well as the position, length and depth of the dimples. 99

1. Introduction

1.1 The significance of tribology in Diesel engines

The Diesel engine has been established as the main propulsion system for ships during the last 50 years. Nowadays, two-stroke marine Diesel engines have achieved an efficiency factor above 50%, and with the ability to burn fuel of the lowest quality, and hence low cost (Heavy Fuel Oil - HFO), they are the most reliable choice for overseas ships. Additionally, due to the remarkably long piston stroke, Diesel engines rotate the propeller with even lower speed, operating it more efficiently.

Because of the constantly increasing cost of fuel oil, it is of great importance to find ways to reduce the amount of energy loss. Energy losses in Diesel engines occur by rejected heat in the exhaust gases and the cooling system, by friction between moving parts and by radiation. Part of the exhaust gas power can be recovered by heat recovery systems, which have been vastly developed in the past years. As of the cooling system, the energy that is drained to cool the several components of the engine may be used to heat-up water with many onboard uses. Finally, friction losses are caused at several different parts of the engine; substantial losses are present at the crankshaft bearings, at the connecting rod bearings, at the cross-head shoe bearing and at the piston ring assembly. These losses cannot be easily recovered. Therefore, there is a lot of ongoing research aiming at design optimization of those components for reduced friction loss and, consequently, reduced fuel consumption.

Tribology is a scientific domain which is engaged with the research of friction, lubrication and wear of interacting surfaces in relative motion. The early aims of tribology were towards improvement of operation and extension of the useful lifetime of mechanical components. Today, tribology spans many different fields from macro-scale applications, like wind turbines, to nanotribology or biomedical tribology. Lubrication, a subdomain of tribology, is concerned with methods to separate two interacting surface by inserting a very thin film of a substance, called lubricant, between them, aiming at reduced friction losses and wear.

1.2 Literature review - Thesis outline

Tribology studies friction, wear and lubrication of mechanical parts. Friction and wear are substantially reduced when a thin layer (film) of material, usually liquid, but also gas and solid in several cases, separates two sliding surfaces [1],[2]. Hydrodynamic lubrication has been a subject of extensive research in recent decades, in order to study the behavior of mechanical components such as bearings, piston rings, camshafts, seals, etc. Each year, hundreds of new papers are published in the scientific domain of tribology, proving the importance of tribological optimization in contemporary machine design.

The theory introduced by Osborne-Reynolds in 1886 forms the basis of hydrodynamic lubrication. According to this theory, pressure can be transferred through a thin lubricating

film located between the two sliding surfaces, which should not be parallel in order to create the necessary geometry of hydrodynamic wedge. In piston rings, which are the main subject of the present study, such a geometry is created between the ring and the liner wall by allowing the proper gap between them, when the ring is placed around the piston. This method allows the creation of lubricating film between the ring and the liner, promoting the development of hydrodynamic pressure. [3]

A plurality of work has been reported in the international literature in the subject of piston ring tribology (e.g. [4]-[6]). The tribological behavior of piston rings can be efficiently predicted on the basis of the Reynolds equation. An important study on piston rings has been published by Jeng et al. in 1992 [4]. Jeng et al. solved the transient problem of hydrodynamic lubrication of piston ring with the use of Reynolds equation. An extension of the basic modeling of [4] to account for starvation oil conditions at the ring inlet has been published by the same group in [5]. A combined numerical and experimental work on piston ring friction in internal combustion engines has been presented by Wakuri and his co-workers in [6].

Regarding lubricant cavitation in hydrodynamic lubrication, it has been a common practice for years to alter the full film pressure results, by setting all predicted negative pressures equal to the cavitation pressure (half-Sommerfeld boundary condition) [3]. Although these methods produced reasonable load values, they violated the principle of mass conservation. To account for the abrupt change of pressure in the cavitation boundary, the assumption that the pressure derivative is zero at the film rupture boundary (Reynolds boundary condition) has been proposed and used extensively in the literature [3]. Still, the film reformation boundary could not be properly predicted, and mass conservation was violated. This is due to the fact that density in the cavitation region of the piston ring is not constant, but depends on the wedge geometry. In order to properly treat the cavitation region, various methods have been developed. ([7]-[10]). A major contribution was that of Elrod and Adams [7], [8], who suggested that the lubricant domain can be divided into two distinct zones. In the first zone, the lubricant creates a complete film and Reynolds equation along with the Reynolds boundary condition can be applied. In the second zone, only a fraction θ of the film thickness is occupied with lubricant, while the remaining film consists of multiple liquid-air striations. Concerning the analytical solution, Elrod proposed the employment of a "global" differential equation, as for θ, which is valid for both regions of the lubricant film and represents different quantities depending on the value of a cavitating factor (1 and 0 respectively). Vijayaraghavan and Keith [9] presented a numerically more stable development of the Elrod-Adams algorithm, by using half-step finite difference methods and deriving the shear and pressure flow terms in a more consistent way. The cavitating index used by Elrod-Adams cavitation algorithm, has been reported by several researchers to cause numerical oscillation and instabilities, due to its sudden change, while trying to predict the cavitation boundary. Fensanghary and Khonsari [10] proposed a modification of this switch function, which smoothens the transition between the full film and the cavitating region and accelerates the convergence speed. Giacopini et al [11], making an alternative formulation of the Elrod-Adams algorithm, presented consistent results in terms of pressure and film fraction

distribution for several typical cases, and therefore was used to validate the results of the developed algorithm.

The purpose of the present thesis is to study the tribological behavior of conventional piston rings, and of piston rings which have undergone surface treatment, including hydrophobicity ([12]-[14]) and artificial surface texturing ([11], [15]-[17]). Hydrophobic surfaces are wetting resistant, reducing the levels of friction during fluid flow. The modified Reynolds equation for slip surface properties was derived following the work of Fatu et al. [12], and the calculations were validated against the results of Pavlioglou et al. [13] and Guo Jun et al. [14]. The algorithms developed have been applied to study the operational characteristics of a piston ring of a typical large two-stroke marine Diesel engine. The results demonstrate that substantial friction reduction can be achieved by properly applying hydrophobicity at part of the ring surface. Further, artificial surface texturing has also been considered as a means of improving the frictional behavior of piston rings. Surface texturing refers to the introduction of small periodic irregularities of different shapes on a surface that may reduce frictional losses and increase load carrying capacity. Recent research by Etsion et al. [15], Papadopoulos et al. [16] and others has confirmed the above statement. In the present work, the proposed algorithm for solving piston ring geometries with artificial surface texturing has been validated against the results of Giacopini et al. [11] and Xiang et al. [17]. For the engine under consideration, implementation of texturing at certain parts of the ring surface substantially decreases friction losses and increases load carrying capacity.

In Chapter 2, the basic principles of the theory of hydrodynamic lubrication are presented, along with the formulation of the Reynolds equation for the plain piston ring surface, and of the modified Reynolds equation for hydrophobic surfaces. In Chapter 3, the utilized finite difference scheme and the developed solution algorithms are presented, followed by the corresponding validation examples. In Chapter 4, the reference engine and piston ring design are described, and the principal operational parameters of the engine are presented. An initial parametric analysis is performed in order to identify the effect of the piston ring design parameters on its performance characteristics. Next, the effects of introducing hydrophobicity and artificial texturing at part of the ring surface are assessed. Finally, in Chapter 5, the main findings of the present thesis are summarized and conclusions are drawn.

2. Piston rings - theoretical approach

2.1 Diesel engine piston rings *(Based on [18]-[21])*

Diesel engines are used to convert the chemical power of fuels into mechanical work in order to move a car, a ship or to operate an electric power generator. The assembly of components that receives the combustion pressure and converts it into torque at the crankshaft forms the power cylinder, and it consists of the cylinder liner, the piston and the connecting rod.

The piston is the component that neighbors directly to the combustion chamber and converts the combustion pressure into a downstroke motion, which is afterwards transferred through the piston pin to the connecting rod, and finally to the crankshaft.

Piston rings, which is the subject of the present work, are circular metallic rings placed around the piston with a certain pretension, and their main purpose is to isolate the combustion chamber volume with minimum friction. They also transfer heat from the piston to the liner and stabilize the piston so that it is supported symmetrically by the bore.

A typical sketch of a piston with its piston rings can be see

]n in Fig. 1.

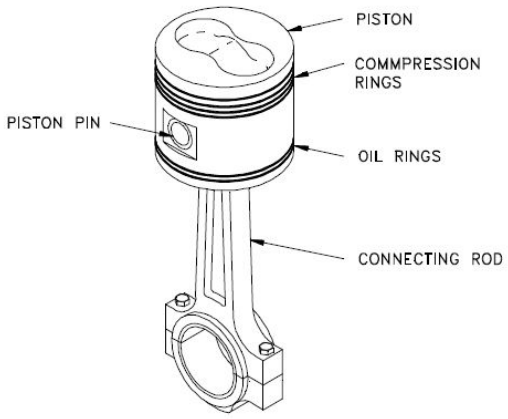

Fig. 1. Piston and its components [19].

In the very first steam engines no piston rings where used because the forces and the temperatures were not as high as those of today's engines. Throughout the evolution of internal combustion engines, these parameters have been considerably increased, leading to increased thermal expansion of the piston material. This is the main reason that made the invention of piston rings, as a sealing body between the piston and the liner, essential.

2.1.1 Piston ring main functions

The main purpose of piston rings is to keep gas blow-by from the combustion chamber to the crankcase to a minimum, because leakage will reduce compression pressure and power will be lost. The combustion gases can flow past the piston ring from three locations, the piston ring gap (the gap used to fit the ring around the piston), the front face of the ring and its

backside [20]. Piston rings seal the gas by expanding outwards towards the liner due to the gas pressure acting on their back and the pretension force.
Piston rings also spread the lubricating oil up and down the liner uniformly and at the same time scrape off the excessive oil and return it to the crankcase during the downstroke. These functions are carried out by specially designed oil rings that have different face profile geometry and are described in detail in Section 2.1.2.
Another function of piston rings is heat transfer from the piston to the liner. Through the cooling system of the piston head, a part of the combustion heat is transferred to the piston boundaries and from there to the piston rings and finally to the liner wall.
Piston rings also stabilize the piston, preventing it from coming in contact with the liner, especially during cold starts. While the piston moves along the liner, the piston ring creates a thin lubricating film between it and the liner preventing metal to metal contact. Film thickness is maximum when the piston speed is maximum (middle of a stroke), and minimum when the piston reaches the two centers (top dead center-TDC, bottom dead center-BDC), where contact between asperities may occur, making a certain amount of wear inevitable. This fact makes the need of self-lubrication properties of the piston ring and liner materials necessary, as explained in a next section.

2.1.2 Piston ring categories

Piston rings always come in a set of two to five rings, forming a ring pack. The ring pack mainly consists of compression rings (2-4) and oil control rings (0-3), depending on the type of the Diesel engine and its size. Four-stroke Diesel engines have 2 or 3 compression rings and only one oil ring, but large two-stroke Diesel engines have 4-6 rings of which 3-4 are compression ring and the rest oil rings .

Compression Rings

Compression rings are the seal that prevents gas blow-by from the combustion chamber to the crankcase. The combustion pressure thrusts the rings, and especially the top ring, downwards onto the piston groove, increasing the material wear, and at the same time creating a path for the gases to enter the groove and press the ring from the backside and against the liner, benefiting the sealing but increasing the mechanical load of the ring, see Fig. 2

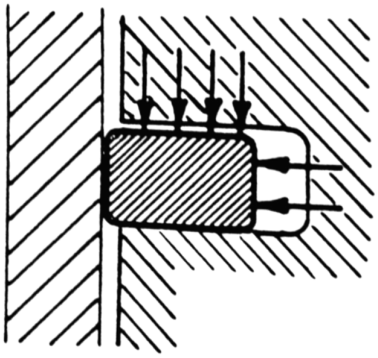

Fig. 2. Gas forces acting on a piston ring [18].

The geometry of the piston ring face profile can be roughly distinguished in three categories, each with its advantages and disadvantages, but combinations of them and more complex geometries also exist. The most common profile of compression rings is the plain rectangular-shaped cross section, which has the best sealing behavior. The barrel-shaped face profile comes to reduce that force and distribute it more uniformly along the width of the ring, but lacks a bit at sealing. Finally, there are the taper faced profile rings, which reduce the pressure of the ring against the liner by supporting a part of the gas pressure with the face profile itself. The sharp edge of this ring can scrape off the excess oil during the downstroke, therefore combining the job of second compression ring and oil-scrap ring [20], as seen in Fig. 3b).

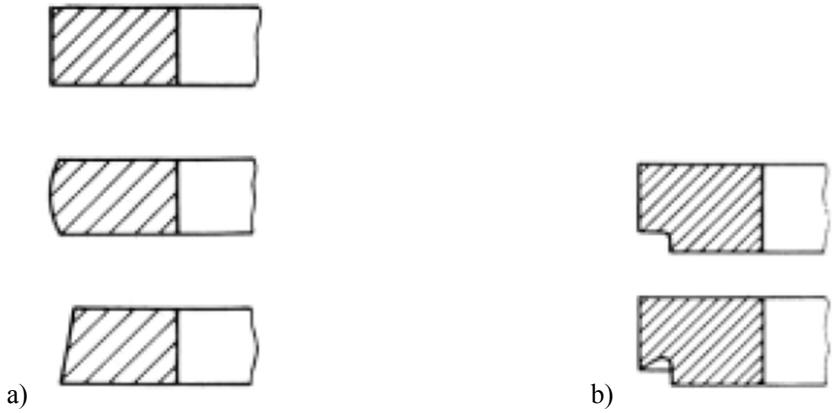

Fig. 3. (a) Compression and (b) compression-oil scrap piston ring profile geometries [20].

Oil Rings

During the first years of use of piston rings, the cylinder was lubricated with splash lubrication. This method was proved to be inadequate when the pressures and temperatures were further increased, because there was not a proper lubricating film to separate the ring from the liner; thus, high pressure could not be maintained, and severe damage occurred. Therefore, the oil control (oil scrap) rings were introduced, whose purpose is to maintain an appropriate oil film on the liner and to scrape off any surplus oil and return it to the crankcase.

The oil rings in a ring pack distribute the oil along the liner evenly, so that a proper lubrication film always exists between the ring and the liner. In most cases, only one oil ring is needed in the pack, and has a different face profile from compression rings, as seen in Fig. 4.

Fig. 4. Oil ring profile geometries [20].

The main characteristic of oil rings is the slots along the peripheral direction. This groove acts as a tank where the excess oil is accumulated and then a part of that is distributed evenly to the liner through the gap between the two edges and the liner and the rest is returned to the crankcase where it is cleaned and recycled. As mentioned above, oil rings are not always necessary, while the compression ones are. For example, two-stroke engines may not need oil rings [26], because the cylinder oil is mixed with the fuel and there is no surplus of oil. Such comparisons between four stroke and two stroke Diesel engines are presented in detail in section 2.1.4 of the present study.

2.1.3 Piston ring materials

Piston ring materials must satisfy certain demands, depending on the running conditions of the engine and its type. Some of them are elasticity/corrosion resistance and thermal conductivity. Piston rings are mainly manufactured from gray cast iron, whose main benefit is the graphite phase that can act as lubricant in the case of oil starvation, during the cold start of the engine, and at TDC and BDC where lubrication is not enough. In piston rings, graphite exists in the form of lustrous grains because of the resulting toughness, which is preferred due to the frequent contact of the ring with the liner and the subsequent wear. In liners, the graphite is in the form of flakes (see Fig. 5), which provides more effective lubrication than grain graphite.

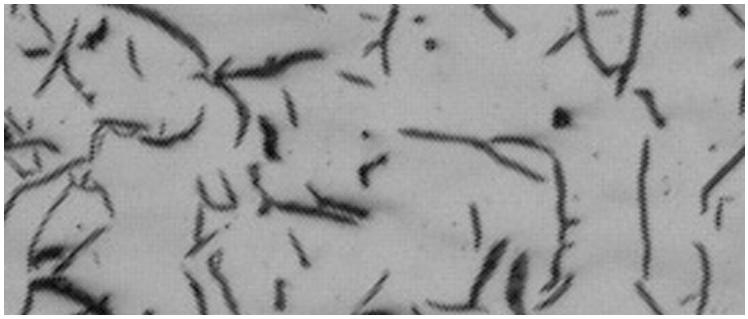

Fig. 5. Cylinder bore microstructure where the black marks constitute the graphite flake [27].

2.1.4 Lubrication of piston rings in two-stroke and four-stroke Diesel engines

In four stroke Diesel engines the oil used in the cylinder lubricating system is the same as that used in the bearing and the cooling system. The piston area and the crankcase communicate directly, so the surplus oil is scraped off, with an oil scrap ring, and returned to the crankcase, from where it is cleared, recycled and returned to the lubricating system.

On the other hand, in two stroke Diesel engines, which will be the main subject of the present work, the crosshead separates the space below the piston and the crankcase, in order to isolate the acidic products of the combustion, which are very corrosive, from the rest of the engine. So the cylinder lubricating system is completely separate from the lubricating system of the crankshaft and the other moving parts of the engine. These engines in some cases have no oil

scrap ring, because a part of the cylinder lubricating oil is burned in the combustion chamber [26]. On the other hand, sometimes the lowest ring of the ring pack is an oil scrap ring that scrapes off the surplus oil and returns it to the scavenge area, because if the excess oil is burned, it creates residuals that increase the material wear and demotes the sealing capability of the rings. Given that cylinder oil is expensive (around 1000$ per day of ship operation) reduction of cylinder oil consumption may contribute substantially to cost reduction.
The use of cylinder oil as sulphur remover is very beneficial, in two stroke marine Diesel engines, that burn Heavy Fuel Oil. HFO is produced from the residue of the distillation process and it includes sulphur in high proportions. Sulphur is extremely corrosive and can damage the material of the engine. Cylinder oil, burned in the combustion chamber, includes certain additives that react with the sulphur and remove it from the fuel mix.

2.1.5 Ways of lubrication, oils and material wear

In two stroke Diesel engines, the lubricant is supplied from external oil pumps, which also operate with pistons, and is channeled in the cylinder via quills on the periphery of the liner. The oil must have appropriate viscosity, in order to (a) spread to the whole liner during the downstroke and (b) create an adequate lubricating film between the piston ring and the liner. Consequently, the cylinder lubricants are most commonly SAE 50 and 60, to satisfy the above needs of viscosity at a temperature of about 200 ^{o}C, and with TBN values from 50 to 70. Certain additives are also required, especially these that react with the sulphur contained in HFO, such as EP additives and detergents.

The technology of base stocks and additives has undergone great evolution during the last 20 years and new products have been developed that meet the most complex needs of current engines. First of all, the viscosity must have a specific value; not too high because the flow of oil will decrease resulting in poor hydrodynamic lubrication and eventually increased wear and friction, and not too low because an oil film of proper thickness cannot be developed, leading again to wear (contact between ring and liner if no film exists) and high friction.
A very important category of additives is that of detergents, which neutralize any external impurities and prevent them from creating deposits (sludge) that affect ring and liner wear. More specifically, the alkaline detergent additives have a critical role because they neutralize and remove the corrosive acidic products of combustion, which are even higher at marine slow-speed two stroke engines because they burn HFO, which includes sulphur in great portions. They also clean the metal surface of the liner from deposits that may corrode the liner material. The areas that are cleaned (neutralized) most effectively are around the quill from where the oil is poured, creating the characteristic clover leaf pattern on the liner.

The wear of the piston rings and the liner is inevitable because the contact between these two and the corrosivity of the environment cannot be reduced to zero. Both the rings and the liners are parts of the engine that are replaced after a predefined period of time, with the rings being replaced more frequent than the liner. This justifies all the efforts that are being made

nowadays to reduce the wear and increase the lifetime of these components, taking into consideration the difficult economic environment in which the ships operate.
More specifically, the parameters that greatly affect the wear of piston rings (or liners) are the following: bore distortion, engine load with higher loads increasing wear and temperature which further increases wear because of oil film thinning. Piston speed is also a critical parameter, since it represents the frequency with which the piston reaches the TDC (Top Dead Center) and the BDC (Bottom Dead Center), where the speed becomes zero and hydrodynamic lubrication breaks down leading to metal to metal contact. In general, increased speed (RPM) leads to increased wear because of the increased number of contacts between the ring and the liner at TDC and BTC, but simultaneously it creates a more robust oil film of higher thickness.

2.2 Hydrodynamic lubrication *(based on [3])*

2.2.1 Introduction

Hydrodynamic lubrication is the ability of a viscous fluid to separate two inclined surfaces with relative motion, by developing hydrodynamic pressure in a thin lubricating film that separates the surfaces. This results to low friction forces, decrease of the surface temperatures and lower rate of material wear.
In order to achieve hydrodynamic lubrication, a moving surface is needed, as well as availability of oil at the gap entrance. The resulting pressure development is caused by the energy transferred from the moving surface to the lubricating oil, and satisfies the conservation of mass, because if no pressure was developed, the flow rate at the domain exit would be lower than the flow rate at the domain inlet.
A sketch of a simple two-dimensional slider is presented in Fig. 6. The bottom surface (rotor) moves with velocity U, while top surface (stator) is inclined and fixed, creating a wedge-like geometry.

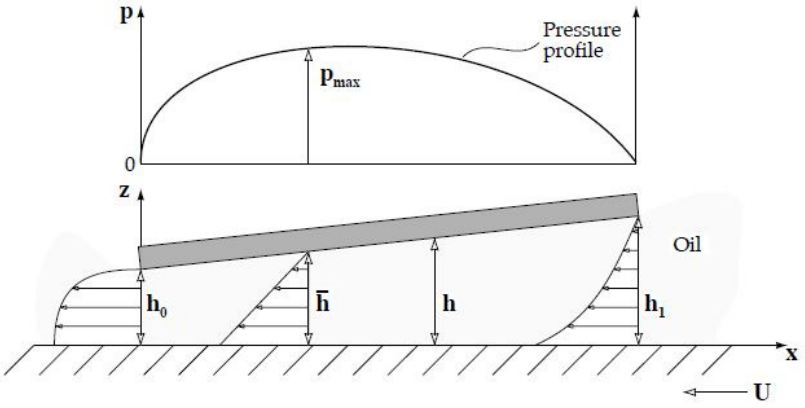

Fig. 6. Hydrodynamic pressure distribution between the inclined surfaces of a simple slider [3].

Lubricating oil is forced to enter the wedge-shaped gap, resulting in increase of its pressure. From the pressure profile of Fig. 6, it can be noted that pressure gradient is positive at the

inlet, allowing the flow of oil into the wedge, and negative at the outlet, allowing the exit of the oil. Finally, it must be remarked that the vertical profile of fluid velocity (in the 2-direction) depends on the spatial derivative of pressure; at the outlet region, it bends towards the outlet and at the inlet it bends towards the inlet.

The most suitable mathematical equation that can express this phenomenon is the Reynolds equation (Osborne Reynolds 1843-1912), which is a simplification of Navier-Stokes equations and can be derived by considering force equilibrium and continuity of flow of an elementary volume of fluid undergoing shear stress.

2.2.2 Simplifying assumptions

In most engineering problems, the processes are too complex and interconnected to be represented by simple mathematical equations. Computers were a real revolution in that respect, as mechanical systems could be analyzed with more detail, taking into account more and more factors.

However, limitations of computational power and time make the use of simpler models inevitable in many cases. In particular, the simplifying assumptions needed for the derivation of the Reynolds equation are the following:

1. The lubricant oil behaves as Newtonian fluid
2. Inertia forces of the lubricant are neglected
3. Pressure is constant along the thickness of the lubricant fluid
4. Flow is considered as laminar
5. Viscosity is constant in the lubricant domain
6. No-slip condition is valid at the fluid-wall interfaces
7. External body forces acting on the fluid film are neglected

2.2.3 Equilibrium of a finite volume of fluid

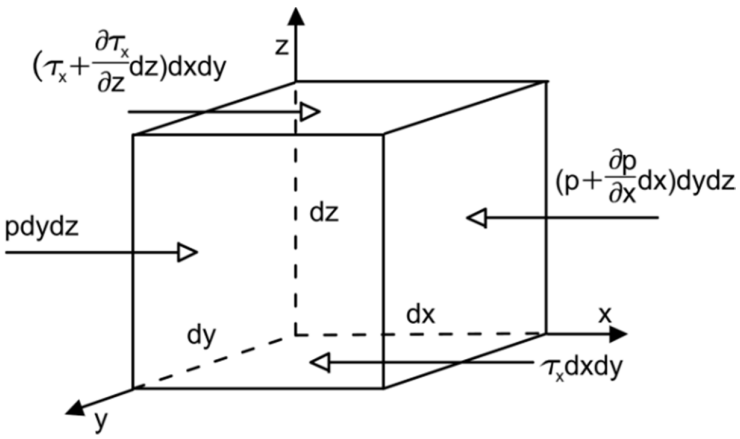

Fig. 7. Force equilibrium of a finite volume of fluid.

A small element of fluid from the lubricating film is considered, as seen in Fig. 7, and it is assumed that forces are applied only along the x direction. The same results can be extended for the other directions, if needed. Equilibrium of the element dictates that, the forces acting on at the left side of the volume must be equal to the forces acting on the right one:

$$pdxdz + \left(\tau_x + \frac{\partial \tau_x}{\partial z} dz \right) dxdz = \left(p + \frac{\partial p}{\partial x} dx \right) dydz + \tau_x dxdz \Rightarrow$$

$$\Rightarrow \frac{\partial \tau_x}{\partial z} dxdydz = \frac{\partial p}{\partial x} dxdydz \tag{1}$$

Considering dxdydz≠0, Eq. (1) can be divided by dxdydz, which yields:

$$\frac{\partial \tau_x}{\partial z} = \frac{\partial p}{\partial x} \tag{2}$$

A similar equation can be derived for the y direction:

$$\frac{\partial \tau_y}{\partial z} = \frac{\partial p}{\partial y} \tag{3}$$

Using assumption 4 of section 2.2.2, the pressure is constant along the z direction, thus:

$$\frac{\partial p}{\partial z} = 0 \tag{4}$$

The shear stress of the lubricant can be expressed with the use of dynamic viscosity η and the rate of shear along both the x and y directions as follows:

$$\tau_x = \eta \frac{\partial u}{\partial z} \tag{5}$$

$$\tau_y = \eta \frac{\partial v}{\partial z} \tag{6}$$

where, τ_x and τ_y are the shear stress acting along the x and y direction, respectively, whereas u, v are the corresponding fluid velocities.

Substituting Eq. (5) into Eq. (2) and Eq. (6) into Eq. (3):

$$\frac{\partial p}{\partial x} = \frac{\partial}{\partial z} \left(\eta \frac{\partial u}{\partial z} \right) \tag{7}$$

$$\frac{\partial p}{\partial y} = \frac{\partial}{\partial z} \left(\eta \frac{\partial v}{\partial z} \right) \tag{8}$$

Integrating Eq. (7) and using the assumption of no-slip conditions (assumption (6.)) of section 2.2.2:

$$\frac{\partial p}{\partial x} \frac{z^2}{2} + C_1 z + C_2 = \eta u \tag{9}$$

For the simple slider of Fig. 6, the following boundary conditions can be used:

$u = U_2$ at $z = 0$ (10)

$u = U_1$ at $z = h$ (11)

These conditions are for the general case where the two surfaces move with different velocities U_1 and U_2; later on, the proper conditions for the case of the present study will be applied.

Substituting the boundary conditions Eq. (10) and Eq. (11) into Eq. (9):

$$C_1 = (U_1 - U_2)\frac{\eta}{h} - \frac{\partial p}{\partial x}\frac{h}{2}$$

$$C_2 = \eta U_2$$

Finally, the equation of velocity results from Eq. (9), by substituting the above constants C_1 and C_2:

$$u = \left(\frac{z^2 - zh}{2\eta}\right)\frac{\partial p}{\partial x} + (U_1 - U_2)\frac{z}{h} + U_2 \tag{12}$$

The equation for the velocity along the y direction can be derived in a similar way:

$$v = \left(\frac{z^2 - zh}{2\eta}\right)\frac{\partial p}{\partial y} + (V_1 - V_2)\frac{z}{h} + V_2 \tag{13}$$

In Eq. (12) and Eq. (13), the three separate terms represent the three velocity profiles that, when combined, give the final velocity profile, see Fig. 8.

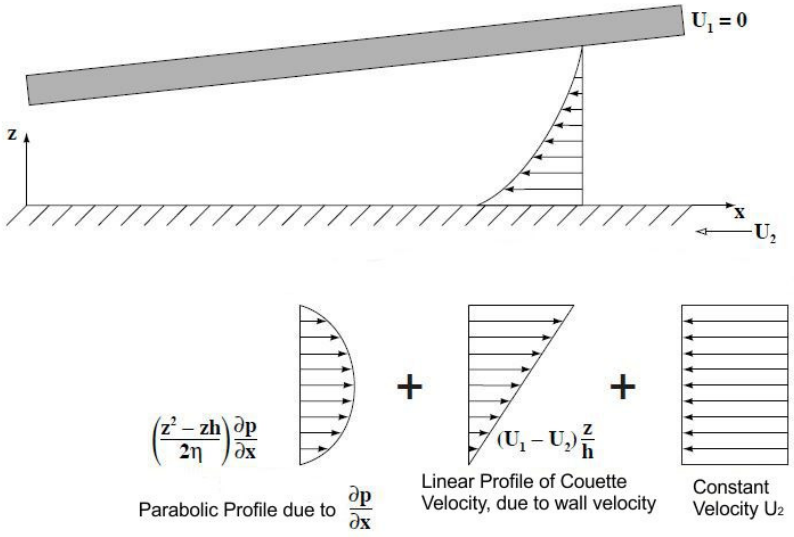

Fig. 8. Profiles of the three separate velocity terms at the lubricant inflow region.

Velocity Assumptions

In most hydrodynamic problems, one of the two surfaces can be considered stationary (stator) and the other one moving with speed U (or/and V) (rotor). Specifically, for the problem of a piston ring, the liner can be assumed to be the rotor and the piston ring the stator, which, according to Fig. 6, yields $U_1=0$ and $U_2=U$.

In the present problem, it is assumed that velocity is non-zero only in the x direction, meaning that the velocities V_1 and V_2 can be taken as zero.

As a result, the equations for the two velocities along the x and y directions, respectively, are:

$$u=\left(\frac{z^2-zh}{2\eta}\right)\frac{\partial p}{\partial x}+-U\frac{z}{h}+U \tag{14}$$

$$v=\left(\frac{z^2-zh}{2\eta}\right)\frac{\partial p}{\partial y} \tag{15}$$

2.2.4 Continuity of flow in a column of finite width

In this section, a infinitesimal volume of the fluid considered, and mass conservation is taken into account. The volume has hexahedron shape and dimensions dx, dy and dz along the three principal axes, as seen in Fig. 9. The mass conservation law can be expressed by means of Eq. (16):

$$\left\{\begin{matrix}\text{Accumulation Rate}\\ \text{of mass in the control}\\ \text{volume}\end{matrix}\right\}=\left\{\begin{matrix}\text{Inflow rate of}\\ \text{the control volume}\end{matrix}\right\}-\left\{\begin{matrix}\text{Outflow rate of}\\ \text{the control volume}\end{matrix}\right\} \tag{16}$$

The above values refer to a specific moment in time, so if at a next moment, t_0, the mass included in the control volume is ρdxdydz, the first term of Eq. (16) can be written as:

$$\frac{\partial \rho}{\partial t}dxdydz \tag{17}$$

Concerning the calculation of inflow and outflow rates, it is assumed that mass is entering the control volume from the left side (+) and exits from the right (-), as see in Fig. 9.

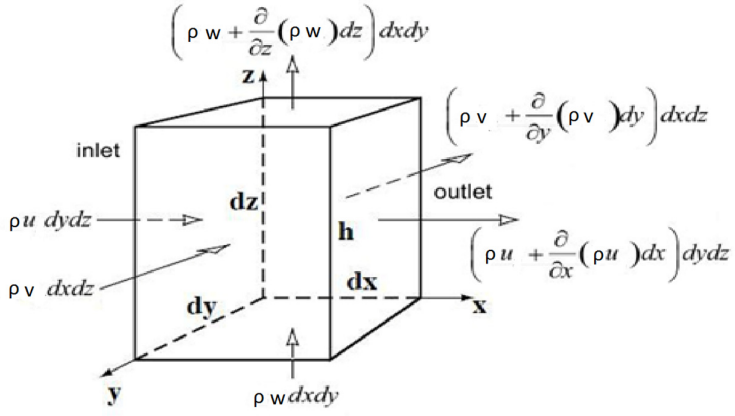

Fig. 9. Continuity of flow in a column of fluid.

So inflow rate, from the left side of the finite volume with area dydz, is equal to:

$$\dot{m}_{x,in} = \rho u dydz \tag{18}$$

The outflow rate, from the right side of the finite volume, is:

$$\dot{m}_{x,out} = \left(\rho u + \frac{\partial}{\partial x}(\rho u)dx\right)dydz \tag{19}$$

In a similar way, the equations for mass conservation in the y and z directions are:

$$\dot{m}_{y,in} = \rho v dxdz \tag{20}$$

$$\dot{m}_{y,out} = \left(\rho v + \frac{\partial}{\partial y}(\rho v)dy\right)dxdz \tag{21}$$

$$\dot{m}_{z,in} = \rho w dxdy \tag{22}$$

$$\dot{m}_{z,out} = \left(\rho w + \frac{\partial}{\partial z}(\rho w)dz\right)dxdy \tag{23}$$

From Eq. (18)-(23), the right part of Eq. (16) can be written as:

$$\left(\dot{m}_{x,in} + \dot{m}_{y,in} + \dot{m}_{z,in}\right) - \left(\dot{m}_{x,out} + \dot{m}_{y,out} + \dot{m}_{z,out}\right) =$$

$$= -\left(\frac{\partial}{\partial x}(\rho u) + \frac{\partial}{\partial y}(\rho v) + \frac{\partial}{\partial z}(\rho w)\right)dxdydz \tag{24}$$

Substituting Eq. (17) and (24) into Eq. (16) yields:

$$\left(\frac{\partial \rho}{\partial t} + \frac{\partial}{\partial x}(\rho u) + \frac{\partial}{\partial y}(\rho v) + \frac{\partial}{\partial z}(\rho w)\right)dxdydz = 0 \tag{25}$$

In Eq. (25), the finite volume dxdydz is non-zero, therefore it can be eliminated:

$$\frac{\partial \rho}{\partial t}+\frac{\partial}{\partial x}(\rho u)+\frac{\partial}{\partial y}(\rho v)+\frac{\partial}{\partial z}(\rho w)=0 \tag{26}$$

Each term of Eq. (26) will now be integrated along the z direction from 0 to h (film thickness) considering that way a column of fluid instead of a finite volume. The velocities substituted in these terms are taken from Eq. (14) and (15).

$$\int_0^h \frac{\partial}{\partial x}(\rho u)dz=\frac{\partial}{\partial x}\int_0^h \rho u dz-\rho u(h)\frac{\partial h}{\partial x}=\frac{\partial}{\partial x}\int_0^h \rho\left[\left(\frac{z^2-zh}{2\eta}\right)\frac{\partial p}{\partial x}-U\frac{z}{h}+U\right]dz-\rho\left[\left(\frac{h^2-h\cdot h}{2\eta}\right)\frac{\partial p}{\partial x}-U\frac{h}{h}+U\right]\frac{\partial h}{\partial x}=$$

$$=\frac{\partial}{\partial x}\int_0^h \rho\left[\left(\frac{z^2-zh}{2\eta}\right)\frac{\partial p}{\partial x}\right]dz-\frac{\partial}{\partial x}\int_0^h U\rho\frac{z}{h}dz+\frac{\partial}{\partial x}\int_0^h U\rho dz=-\frac{\partial^2 p}{\partial x^2}\frac{\rho}{12\eta}h^3+\frac{U}{2}\frac{\partial(\rho h)}{\partial x}$$

$$\int_0^h \frac{\partial}{\partial y}(\rho v)dz=\frac{\partial}{\partial y}\int_0^h \rho\left(\frac{z^2-zh}{2\eta}\right)\frac{\partial p}{\partial y}dz-\rho\left(\frac{h^2-h\cdot h}{2\eta}\right)\frac{\partial p}{\partial y}\frac{\partial h}{\partial y}=-\frac{\partial^2 p}{\partial y^2}\frac{\rho}{12\eta}h^3$$

$$\int_0^h \frac{\partial}{\partial z}(\rho w)dz=\rho w=\rho\frac{\partial h}{\partial t}$$

$$\int_0^h \frac{\partial \rho}{\partial t}dz=\frac{\partial \rho}{\partial t}h$$

Finally substituting the above terms in (26), results in Eq. (27) which is the Reynolds equation:

$$-\frac{\partial^2 p}{\partial x^2}\frac{\rho}{12\eta}h^3-\frac{\partial^2 p}{\partial y^2}\frac{\rho}{12\eta}h^3+\frac{U}{2}\frac{\partial(\rho h)}{\partial x}+\frac{\partial(\rho h)}{\partial t}=0 \tag{27}$$

2.2.5 Assumption of constant density

Considering that the fluid density is constant in the lubricant domain, with a value of ρ_0 Eq. (21) is simplified as follows:

$$\frac{\partial^2 p}{\partial x^2}\frac{h^3}{12\eta}+\frac{\partial^2 p}{\partial y^2}\frac{h^3}{12\eta}-\frac{U}{2}\frac{\partial h}{\partial x}-\frac{\partial h}{\partial t}=0 \tag{28}$$

2.2.6 Performance parameters of piston rings

In Fig. 10, a sketch of a typical piston ring geometry is presented. Using the Reynolds equation (Eq. (28)), the pressure distribution in the lubricant separating the ring from the liner can be calculated. Three important performance parameters of piston rings are load capacity (total force acting on the ring in the z-direction), friction force (total force acting on the ring in the x-direction), and friction coefficient, which by definition, is the ratio of friction force to load capacity. Formulae of calculating those quantities are presented hereinafter.

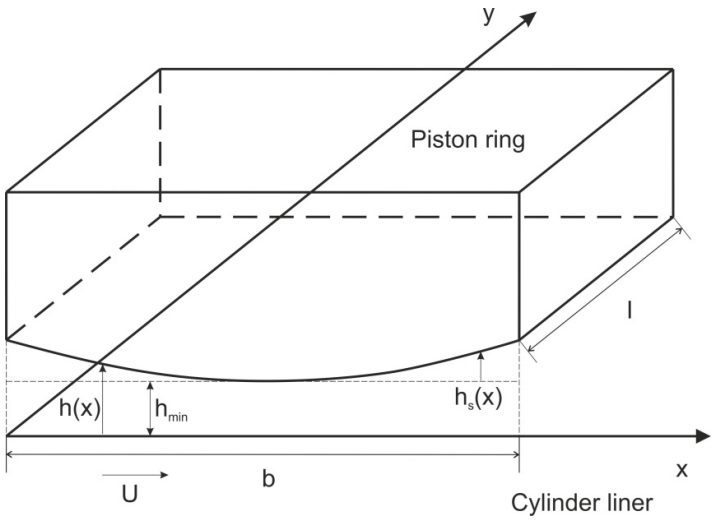

Fig. 10. Sketch of a typical piston ring geometry.

Load Capacity

The load capacity can be calculated by integrating pressure distribution over the ring area:

$$W = \int_0^l \int_0^b p dx dy \tag{29}$$

where, l and b are the length and width of the piston ring (see Fig. 10)

Friction Force

Friction force can be obtained by integrating the x-component of shear stress over the piston ring area

$$F = \int_0^l \int_0^b \tau_x dx dy \tag{30}$$

where τ_x at the ring-fluid interface can be taken from Eq. (5), and $\partial u / \partial z$ of Eq. (5) can be easily calculated by differentiating Eq. (12).

According to what it is mentioned during the derivation of the Reynolds equation, the shear stress, in terms of dynamic viscosity and velocity, takes the following form:

$$\tau = \eta \frac{du}{dz} \tag{31}$$

where du/dz is easily calculated by derivating Eq. (12) of velocity u.

Friction coefficient

Once the load capacity and friction force are known, the coefficient of friction, f, can be calculated as:

$$f = \frac{F}{W} \tag{32}$$

2.2.7 Boundary conditions

In Fig. 11, the geometry of a simple converging-diverging slider is presented. In order to solve the Reynolds equation in the lubricant domain, appropriate boundary conditions need to be described. In the following paragraphs, a description of the boundary conditions mostly used in lubrication problems is given.

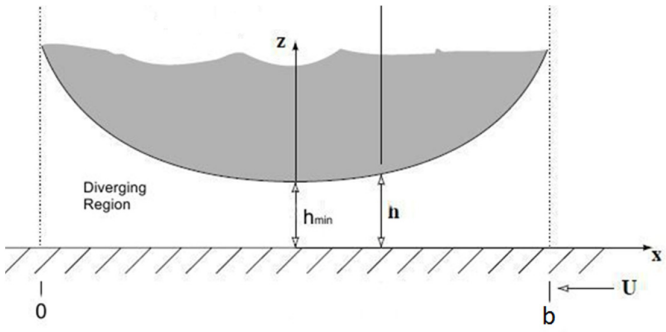

Fig. 11. Sketch of a simple slider.

Full-Sommerfeld Boundary Condition

This boundary condition assumes, that pressure is equal to zero at the slider inlet and outlet cross-sections. The pressure distribution for the Full-Sommerfeld boundary condition is presented in Fig. 12. Practically, the use of this boundary condition allows calculation of negative pressures at the diverging region of the slider. In particular, in the diverging part of the slider, pressure distribution is the mirror image of the positive pressure distribution of the converging part of the slider. Overall, the total hydrodynamic load exerted on the slider is zero, which is unrealistic.

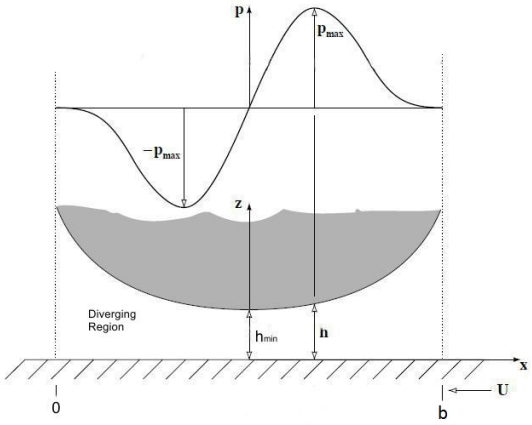

Fig. 12. Solution of the Reynolds equation with Full-Sommerfeld boundary conditions.

Half-Sommerfeld Boundary Condition

A simple remedy to correct the unrealistic results of the full-Sommerfeld condition, is by setting the negative pressures equal to zero. This is the half-Sommerfeld boundary condition and the respective pressure distribution has the form of Fig. 13.

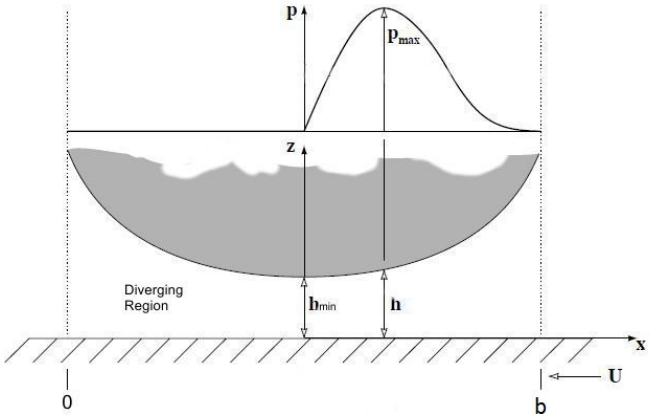

Fig. 13. Solution of the Reynolds equation with Half-Sommerfeld boundary conditions.

The disadvantage of this boundary condition is that it causes a discontinuity between the pressurized region and the region of zero pressure. Nonetheless, the use of this method is straight forward, and the obtained results are accurate enough for basic engineering use.

Reynolds boundary condition

A better solution to the problem of non realistic boundary conditions was given by Reynolds, who suggested that negative pressures should be set equal to zero and that at the boundary of non-zero and zero pressure the spatial derivative of pressure should be also equal to zero. The resulting pressure distribution is that of Fig. 14.

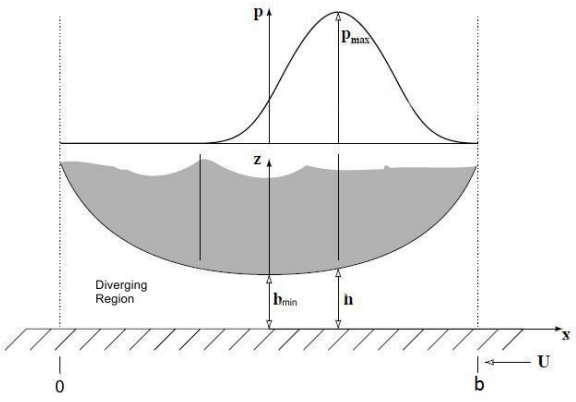

Fig. 14. Solution of the Reynolds equation with Reynolds boundary conditions.

2.3 The problem of cavitation at piston rings *(based on [3], [22]-[24])*

As analyzed previously, during hydrodynamic lubrication, a substantial drop of pressure may occur in the diverging part of the wedge created between the liner and the piston ring. Existence of very low pressure may trigger the phenomenon of cavitation in liquids, which is described below.

In general, two kinds of cavitation can be distinguished. Firstly, when the bubbles emanate from lubricant evaporation, the phenomenon is called *vaporous cavitation*. When liquid pressure is sufficiently low, the liquid evaporates (boils) generating vapor bubbles. When the liquid regains its pressure, these bubbles instantly collapse generating locally high values of pressure that wear and damage the material. This is the most dangerous type of cavitation, because the local pressures from vapor reliquification can reach the values of 0.5 GPa, causing damage and wear that can even suspend the functionality of the lubricated mechanical system. This phenomenon is similar to the cavitation encountered at the edges of ship propellers.

On the other hand, liquids contain dissolved air in low proportions (up to 10%). For a given percentage of air into oil, when pressure becomes lower than a certain value, the air dissolved in the fluid is partially released, generating air bubbles. If the pressure is suddenly raised, the air bubbles undergo a rapid (nearly isentropic) compression, which increases local temperature. This may seriously affect oil properties and possibly equipment. This phenomenon is called *gaseous cavitation.* In addition to this, when the fluid enters the diverging section, the existing lubricating film cannot cover the whole gap, and, as a result, the film ruptures and is separated in finger-like areas of gas and liquid. Gas enters the domain from the surrounding environment, and is sucked into the fluid area creating streamers of air inside the cavitation region. Reynolds has correctly assumed that, in the cavitation region, pressure and its spatial derivative are equal to zero.

The air appearing in the fluid, either in the form of bubbles or streamers, consequently reduces the part of the wedge geometry that is filled with lubricant, and increases the proportion of air. The fluid - gas ratio in the cavitation region may be calculated by considering mass conservation of the lubricant.

Fig. 15. Liquid and gas streamers in the cavitation region.

2.3.1 Modification of Reynolds equation in the cavitation region

The Reynolds equation in the cavitation region can be derived from Eq. (21) by considering that the spatial derivatives of pressure are equal to zero:

$$\frac{U}{2}\frac{\partial(\rho h)}{\partial x}+\frac{\partial(\rho h)}{\partial t}=0 \tag{33}$$

2.4 Hydrophobicity

2.4.1 The phenomenon of hydrophobicity

Hydrophobicity is the physical property of a surface to repel water. The molecules of these surfaces tend to be non polar, consequently preferring other neutral molecules. Water droplets on a hydrophobic surface will exhibit a high contact angle, which is a principal parameter for characterizing surface hydrophobicity.

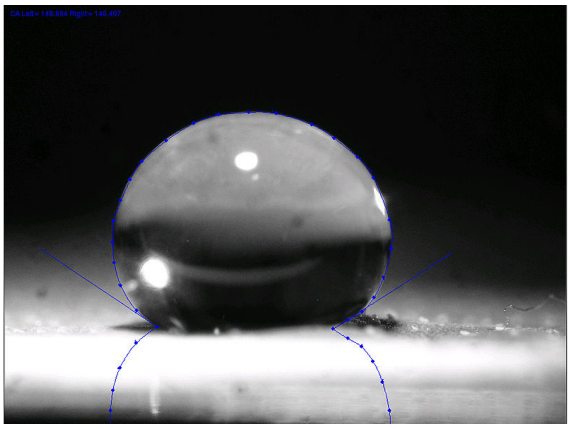

Fig. 16. Measurement of contact angle of a liquid drop [30].

As a result, friction between the liquid and a hydrophobic surface, is very low, allowing the liquid to slip on the surface and not wet it. Lotus leaf is an example of hydrophobic surfaces found in nature, which can even allow honey, a high viscosity liquid, to slip on its surface. By observing the detailed geometry of the surface of the lotus leaf, researchers were led to the conclusion that the nanostructure of the leaf is causing that behavior. This structure can be seen in Fig. 17and Fig. 18:

Fig. 17. Liquid drops on a lotus leaf [30].

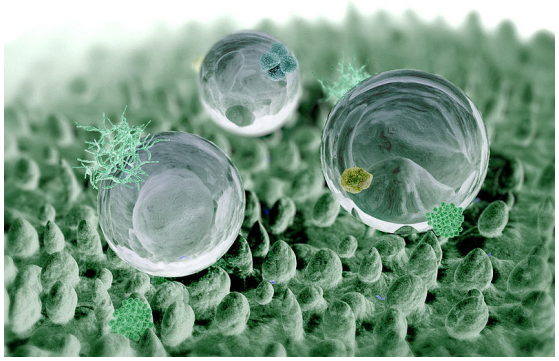

Fig. 18. Lotus leaf under the microscope [30].

Today, it is possible, to artificially create a hydrophobic surface in a laboratory, and several industrial applications have been proposed (e.g. ship hull coatings). As stated earlier, hydrophobicity of a surface can be measured by the shape of a droplet when placed on it. The corresponding parameter is the contact angle between the droplet and the surface.

To translate the phenomenon of hydrophobicity in mathematical equations, the slip conditions in the fluid-solid interface must be reconsidered. In the derivation of Reynolds equation, it was assumed that the in the fluid-solid interface the liquid has the same velocity as the velocity of the moving wall. In the case of hydrophobic surfaces, the liquid velocity is different from that of the solid boundary, and can be calculated from the following equation:

$$u_s = (\tau - \tau_c)\frac{b_s}{\eta} \tag{34}$$

where, τ: the shear stress of the fluid on the fluid-solid interface
τ_c: the critical shear stress, above which slip occurs
η: fluid viscosity
b_s: slip length

Slip length is a surface property that defines how slippery a surface is when interacting with a certain fluid. It is defined as the imaginary length below the surface where the fluid velocity would become zero, assuming linear velocity distribution and rate equal to the velocity derivative at the fluid-surface interface, see Fig. 19.

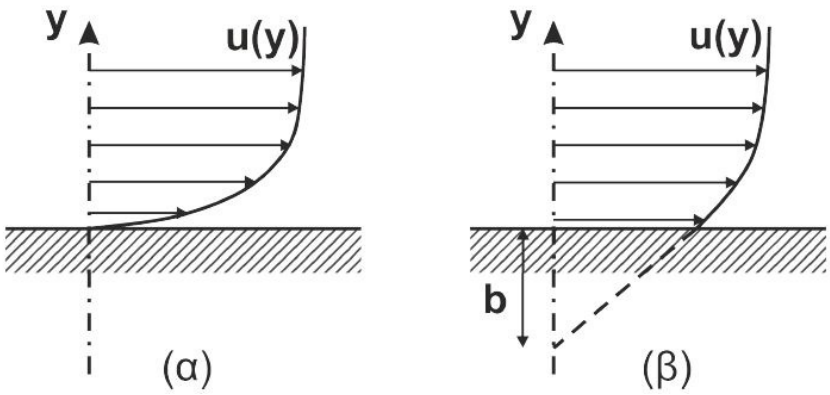

Fig. 19. Velocity profiles: (a) no-slip condition, (b) slip conditions with slip length b_s.

2.4.2 Mathematical equations for surfaces with slip properties

Here, the Reynolds equation for surfaces with slip properties is derived:

Starting from Eq. (9):

$$\frac{\partial p}{\partial x}=\frac{\partial}{\partial z}\left(\eta\frac{\partial u}{\partial z}\right)=>\left(\frac{\partial p}{\partial x}\right)\partial z=\partial\left(\eta\frac{\partial u}{\partial z}\right)=>\frac{\partial p}{\partial x}z+C_1=\eta\frac{\partial u}{\partial z}=>\left(\frac{\partial p}{\partial x}z+C_1\right)\partial z=\eta\partial u=>$$

$$\frac{\partial p}{\partial x}\frac{z^2}{2}+C_1z+C_2=\eta u=>u=\frac{\partial p}{\partial x}\frac{z^2}{2\eta}+\frac{C_1}{\eta}z+\frac{C_2}{\eta} \tag{35}$$

The first derivative of velocity in the x-direction is:

$$\frac{\partial p}{\partial x}z+C_1=\eta\frac{\partial u}{\partial z} \tag{36}$$

The boundary conditions are now different from those applied to the simple Reynolds equation. Slip will occur at the hydrophobic region of the surfaces if the local value of the shear stress is higher than the critical value, as described in Eq. (34). This equation suggests that slip velocity is proportional to the difference between the shear stress and the critical value, with proportionality factors a_l for the liner and a_r for the piston ring, which are equal to the ratio of slip length, b_l or b_r , and the lubricant viscosity, η.

$$a_r=\frac{b_r}{\eta},\ a_l=\frac{b_l}{\eta} \tag{37}$$

Here, critical shear stress values are $\tau_{C,l}$ for the liner surface and $\tau_{C,r}$ for the piston ring and Eq. (34) and Eq. (37) yield:

$$u_{z=0}=U-a_l\left(-\eta\left.\frac{\partial u}{\partial z}\right|_{z=0}-\tau_{C,l}\right) \tag{38}$$

$$u_{z=h}=a_r\left(-\eta\left.\frac{\partial u}{\partial z}\right|_{z=h}-\tau_{C,r}\right) \tag{39}$$

A similar procedure can be used for the derivation of velocity v along y direction.

$$v=\frac{\partial p}{\partial y}\frac{z^2}{2\eta}+\frac{C_1}{\eta}z+\frac{C_2}{\eta} \tag{40}$$

The first derivative of the fluid velocity in the y direction is:

$$\frac{\partial p}{\partial y}z+C_1=\eta\frac{\partial v}{\partial z} \tag{41}$$

The velocity boundary condition in the y-direction can be derived, taking into account that velocity v depends only on the pressure gradient dp/dy (see Fig. 20), since the wall velocity V is zero.

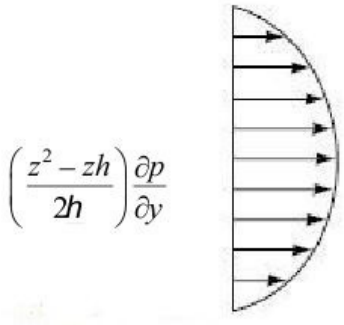

Fig. 20. Velocity parabolic profile in the y-direction caused from the pressure derivative.

$$v_{z=0} = a_l\left(\eta\left.\frac{\partial v}{\partial z}\right|_{z=0} - \tau_{C,l}\right) \tag{42}$$

$$v_{z=h} = a_r\left(-\eta\left.\frac{\partial v}{\partial z}\right|_{z=h} - \tau_{C,r}\right) \tag{43}$$

After presenting the new boundary conditions of velocity, the modified Reynolds equation for hydrophobic surfaces, Eq. (44) can be derived. The detailed derivation of Eq. (44) is presented in Appendix A.

$$\begin{aligned}
&\frac{\partial}{\partial x}\left(\frac{\rho h^2}{12\eta}\frac{\partial p}{\partial x}\frac{h^2 + 4\eta\left(a_l + a_r\right)h + 12\eta^2 a_l a_r}{h + \eta\left(a_l + a_r\right)}\right) + \frac{\partial}{\partial y}\left(\frac{\partial p}{\partial y}\frac{\rho h^2}{12\mu}\frac{h^2 + 4\eta h\left(a_r + a_l\right) + 12a_l a_r\eta^2}{h + \eta\left(a_r + a_l\right)}\right) = \\
&= \frac{U}{2}\frac{\partial}{\partial x}\left(\rho\frac{h^2 + 2\eta a_r h}{h + \eta\left(a_l + a_r\right)}\right) - U\rho\frac{\eta a_r}{h + \eta\left(a_l + a_r\right)}\frac{\partial h}{\partial x} + \frac{\rho h}{2\eta}\frac{\eta a_r h + 2a_l a_r\eta^2}{h + \eta\left(a_l + a_r\right)}\left(\frac{\partial h}{\partial x}\frac{\partial p}{\partial x} + \frac{\partial p}{\partial y}\frac{\partial h}{\partial y}\right) + \\
&+ \frac{\partial}{\partial x}\frac{1}{2}\left(\rho\frac{h^2\left(a_l\tau_{C,l} - a_r\tau_{C,r}\right) + 2a_l a_r\eta h\left(\tau_{C,l} - \tau_{C,r}\right)}{h + \eta\left(a_l + a_r\right)}\right) + \rho\frac{\eta a_r a_l\left(\tau_{C,r} - \tau_{C,l}\right) + a_r\tau_{C,r}h}{h + \eta\left(a_l + a_r\right)}\frac{\partial h}{\partial x} - \\
&- \frac{\partial}{\partial y}\left[\frac{\rho h}{2}\frac{\left(a_r\tau_{C,r} + a_l\tau_{C,l}\right)h + 2\eta a_r a_l\left(\tau_{C,r} + \tau_{C,l}\right)}{h + \eta\left(a_r + a_l\right)}\right] + \rho\frac{a_r\tau_{C,r}h + \eta a_r a_l\left(\tau_{C,r} + \tau_{C,l}\right)}{h + \eta\left(a_r + a_l\right)}\frac{\partial h}{\partial y} + \frac{\partial\left(\rho h\right)}{\partial t}
\end{aligned} \tag{44}$$

In the active region of the lubricant density is assumed constant, therefore Eq. (44) is simplified as follows:

$$\frac{\partial}{\partial x}\left(\frac{h^2}{12\mu}\frac{\partial p}{\partial x}\frac{h^2+4\eta\left(a_l+a_r\right)h+12\eta^2 a_l a_r}{h+\eta\left(a_l+a_r\right)}\right)+\frac{\partial}{\partial y}\left(\frac{\partial p}{\partial y}\frac{h^2}{12\eta}\frac{h^2+4\eta h\left(a_r+a_l\right)+12a_l a_r\eta^2}{h+\eta\left(a_r+a_l\right)}\right)=$$

$$=\frac{U}{2}\frac{\partial}{\partial x}\left(\frac{h^2+2\eta a_r h}{h+\eta\left(a_l+a_r\right)}\right)-U\frac{\eta a_r}{h+\eta\left(a_l+a_r\right)}\frac{\partial h}{\partial x}+\frac{h}{2\eta}\frac{\eta a_r h+2a_l a_r\eta^2}{h+\eta\left(a_l+a_r\right)}\left(\frac{\partial h}{\partial x}\frac{\partial p}{\partial x}+\frac{\partial p}{\partial y}\frac{\partial h}{\partial y}\right)+$$

$$+\frac{\partial}{\partial x}\frac{1}{2}\left(\frac{h^2\left(a_l\tau_{C,l}-a_r\tau_{C,r}\right)+2a_l a_r\eta h\left(\tau_{C,l}-\tau_{C,r}\right)}{h+\eta\left(a_l+a_r\right)}\right)+\frac{\eta a_r a_l\left(\tau_{C,r}-\tau_{C,l}\right)+a_r\tau_{C,r}h}{h+\eta\left(a_l+a_r\right)}\frac{\partial h}{\partial x}-$$

$$-\frac{\partial}{\partial y}\left[\frac{h}{2}\frac{\left(a_r\tau_{C,r}+a_l\tau_{C,l}\right)h+2\eta a_r a_l\left(\tau_{C,r}+\tau_{C,l}\right)}{h+\eta\left(a_r+a_l\right)}\right]+\frac{a_r\tau_{C,r}h+\eta a_r a_l\left(\tau_{C,r}+\tau_{C,l}\right)}{h+\eta\left(a_r+a_l\right)}\frac{\partial h}{\partial y}+\frac{\partial h}{\partial t} \tag{45}$$

In the cavitation region, the lubricant film breaks and streamers of oil and gas are formed. The balance between these two is determined by consideration of flow continuity, therefore density of the oil-gas mixture should be taken into account. If the pressure gradients of Eq. (44) are set to zero, Eq. (46) is derived.

$$\frac{U}{2}\frac{\partial}{\partial x}\left(\rho\frac{h^2+2\eta a_r h}{h+\eta\left(a_l+a_r\right)}\right)-U\rho\frac{\eta a_r}{h+\eta\left(a_l+a_r\right)}\frac{\partial h}{\partial x}+\frac{\partial}{\partial x}\frac{1}{2}\left(\rho\frac{h^2\left(a_l\tau_{C,l}-a_r\tau_{C,r}\right)+2a_l a_r\eta h\left(\tau_{C,l}-\tau_{C,r}\right)}{h+\eta\left(a_l+a_r\right)}\right)$$

$$+\rho\frac{\eta a_r a_l\left(\tau_{C,r}-\tau_{C,l}\right)+a_r\tau_{C,r}h}{h+\eta\left(a_l+a_r\right)}\frac{\partial h}{\partial x}-\frac{\partial}{\partial y}\left[\frac{\rho h}{2}\frac{\left(a_r\tau_{C,r}+a_l\tau_{C,l}\right)h+2\eta a_r a_l\left(\tau_{C,r}+\tau_{C,l}\right)}{h+\eta\left(a_r+a_l\right)}\right]$$

$$+\rho\frac{a_r\tau_{C,r}h+\eta a_r a_l\left(\tau_{C,r}+\tau_{C,l}\right)}{h+\eta\left(a_r+a_l\right)}\frac{\partial h}{\partial y}+\frac{\partial\left(\rho h\right)}{\partial t}=0 \tag{46}$$

2.5 Artificial texturing

Artificial surface texturing is the introduction of small geometric irregularities in the form of dimples of different shapes on the surface of mechanical components. This kind of surface treatment may improve the tribological behavior of sliding surfaces in terms of load capacity and friction force.

It is well known that two parallel sliders with a relative motion cannot develop a pressure field, because the theory of hydrodynamic lubrication requires the existence of a hydrodynamic wedge. However, proper introduction of texturing on the stator of a parallel slider enables pressure generation in the lubricant film, and support of external loads.

The positive effect of surface texturing, on thrust bearings and piston rings, has been demonstrated in recent literature results [13], [15] and [16]. Texturing comes in different shapes, such as rectangular, trapezoidal and spherical, and is characterized by several parameters, such as texture depth and texture density. A critical parameter that needs to be defined is the region of the slider that needs to be textured, for optimum slider performance.

In order to solve the problem of hydrodynamic lubrication in textured sliders, the Reynolds equation can be used without any particular alteration apart from that of the fluid film geometry, which should be properly modified to account for the texture geometry. However, since textures cause steep divergent and convergent geometries, the use of the Reynolds equation with Reynolds boundary conditions is not always recommended, because the cavitation region may not be properly defined. In general, several models have been developed, which are able to accurately identify the cavitation region, and one of these is the Elrod-Adams mass conserving model, which is also considered in the present study (see section 3.2).

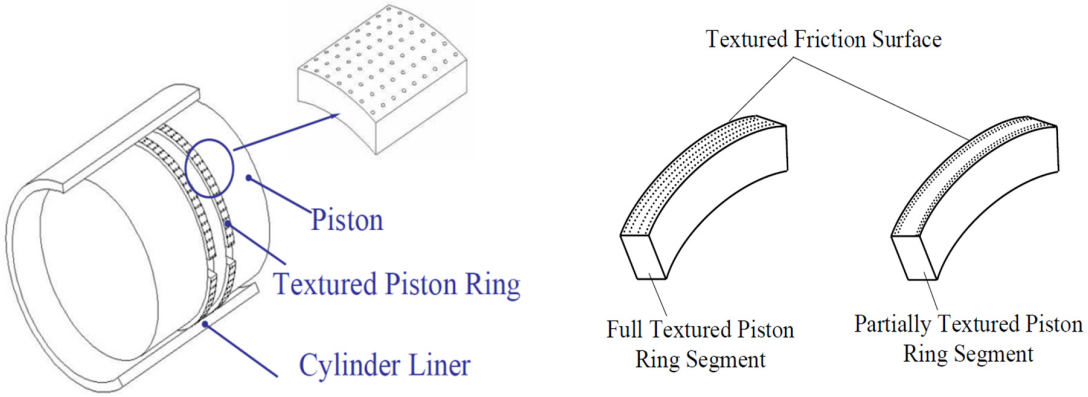

Fig. 21. Example of textured piston rings [29].

3. Numerical solution of Reynolds equation for hydrodynamic lubrication of piston ring

3.1 Finite difference method

In the present section, the Finite difference Method (FDM) will be used for solving the Reynolds equation (Eq. (28) of section 2.2.5) for piston rings. In Fig. 22, a typical geometry of a segment of a piston ring is presented. A three dimensional lubricant film separates the surfaces of the piston and the cylinder liner. The film spans in the x and y-axes of Fig. 22, along the ring profile and the ring circumference, respectively. At every point (x, y), the film is characterized by a thickness value h(x,y), which can be calculated by adding parameter $h_s(x,y)$, corresponding to the ring profile, to h_{min}, which represents the minimum gap between the piston ring and the liner:

$$h(x,y) = h_s(x,y) + h_{\min} \tag{47}$$

In the present work, the ring is assumed rigid; rotations about the x- and y-axes are not considered. Equilibrium of the ring is attained when external forces acting on the ring are balanced by hydrodynamic forces developed in the lubricant film, separating the ring and the liner. At high external loads the ring will move closer to the liner, decreasing h_{min}, whereas at low external loads the ring will move in the opposite direction, increasing h_{min}. Therefore, for transient ring loads, h_{min} will also be a function of time.

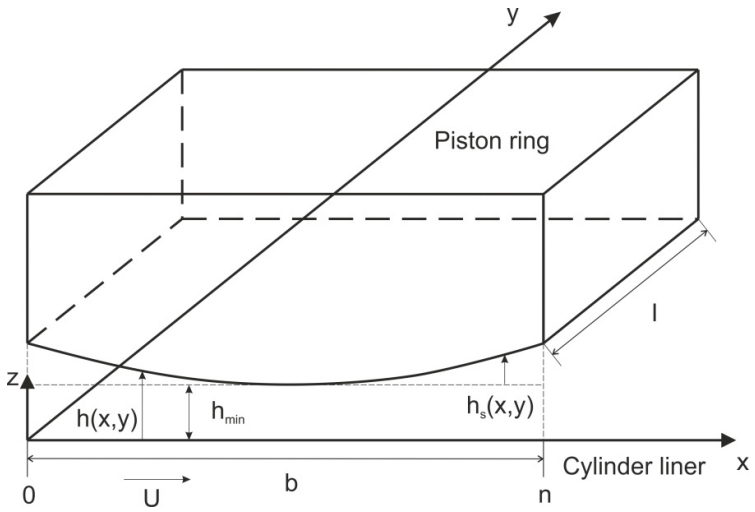

Fig. 22. Sketch of a piston ring segment.

Hydrodynamic pressure in the lubricant separating the ring and the liner is developed due to the reciprocating motion of the ring with (time-dependent) velocity U along the x-axis. Here, equivalently, the liner is considered to be moving with a velocity U and the piston ring is assumed stationary.

Viscosity is considered constant throughout the domain of the lubricating film (η(i,j)=η). Viscosity is, in general, a function of temperature. For a given lubricant, mean oil temperature can be calculated as the average of the combustion chamber and the crankcase temperatures. The corresponding viscosity can be computed by appropriate viscosity-temperature graphs.

In the present work, for the numerical solution of the Reynolds equation, a central finite differencing scheme is utilized. The lubricant domain, in the x- and y-directions is discretized with the use of a spatial grid, consisting of nxm points, respectively, see Fig. 23. At every point (i,j) of the domain (1≤i≤n, 1≤j≤m), film thickness h(i,j) is computed.

Finally the term dh/dt is the squeeze motion of the oil film. The way this value is calculated will be described in the algorithm Section 3.2, where the algorithm flowchart is presented, and for now it will be considered as a known parameter dhdt(i,j).

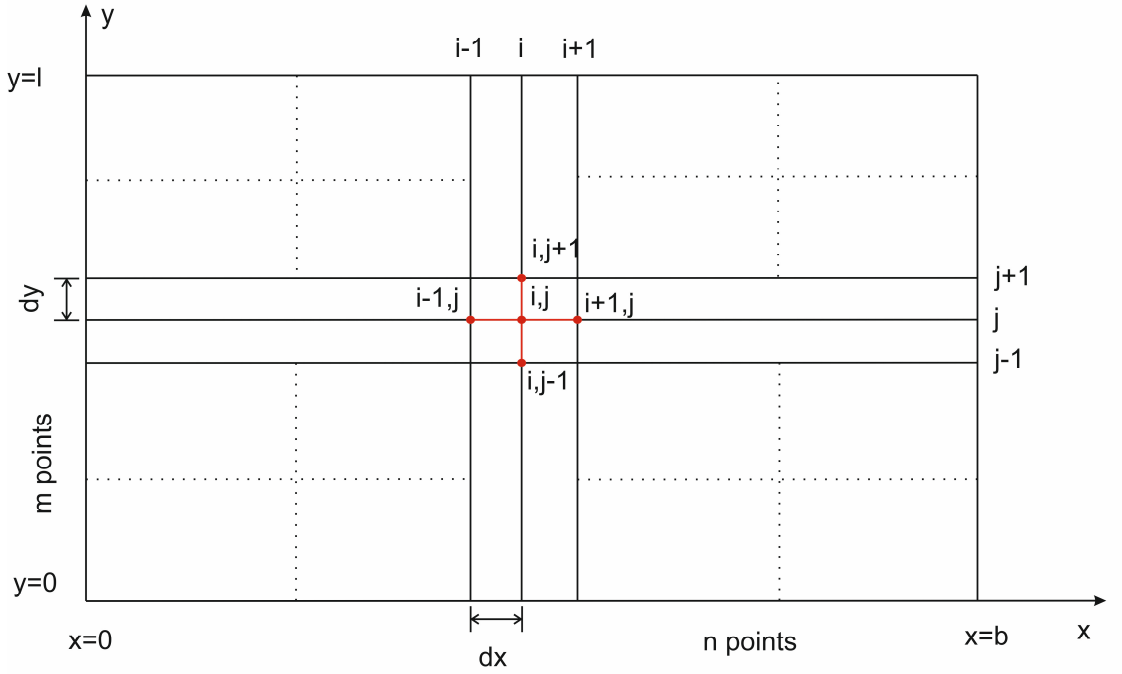

Fig. 23. Discretization details of the lubricant domain separating the ring from the cylinder liner.

Using the finite difference method, the spatial derivative of a generic variable u(i,j) in the x-direction can be approximated as follows:
From the development of Taylor series:

$$u_{i+1,j} = u_{i,j} + \frac{\partial u}{\partial x_{i,j}}\Delta x + \frac{\partial^2 u}{\partial x_{i,j}^{\,2}}\frac{(\Delta x)^2}{2!} + \frac{\partial^3 u}{\partial x_{i,j}^{\,3}}\frac{(\Delta x)^3}{3!} + \ldots + \frac{\partial^n u}{\partial x_{i,j}^{\,n}}\frac{(\Delta x)^n}{n!}$$

$$u_{i-1,j} = u_{i,j} + \frac{\partial u}{\partial x_{i,j}}\Delta x + \frac{\partial^2 u}{\partial x_{i,j}^{\,2}}\frac{(\Delta x)^2}{2!} - \frac{\partial^3 u}{\partial x_{i,j}^{\,3}}\frac{(\Delta x)^3}{3!} + \ldots$$

Considering a small value of Δx, the higher order terms of the previous equations can be neglected, and the derivative of u at (i,j) can be calculated as:

$$\frac{\partial u}{\partial x}(i,j)=\frac{u_{i+1,j}-u_{i-1,j}}{2\Delta x}=\frac{u_{i+1,j}-u_{i-1,j}}{x_{i+1}-x_{i-1}} \tag{48}$$

The neglected higher order terms form the error from the exact value (truncation error), therefore, for accurate calculations, an appropriately small value of Δx must be selected. Each term of the Reynolds equation Eq. (28) is written using central differences, as follows:

Pressure term along the x direction

$$\frac{\partial}{\partial x}\left(\frac{h^3}{12\eta}\frac{\partial p}{\partial x}\right)=\frac{\partial}{\partial x}\left(\frac{h^3}{12\eta}\right)\frac{\partial p}{\partial x}+\frac{h^3}{12\eta}\frac{\partial^2 p}{\partial x^2}=$$

$$=\frac{\frac{h^3(i+1,j)}{12\eta(i+1,j)}-\frac{h^3(i-1,j)}{12\eta(i-1,j)}}{x(i+1)-x(i-1)}\frac{p(i+1,j)-p(i-1,j)}{x(i+1)-x(i-1)}+\frac{h(i,j)^3}{12\eta(i,j)}\frac{p(i+1,j)-2p(i,j)+p(i-1,j)}{\left(x(i+1)-x(i)\right)\left(x(i)-x(i-1)\right)}$$

Pressure term along the y direction

$$\frac{\partial}{\partial x}\left(\frac{h^3}{12\eta}\frac{\partial p}{\partial y}\right)=\frac{\partial}{\partial x}\left(\frac{h^3}{12\eta}\right)\frac{\partial p}{\partial y}+\frac{h^3}{12\eta}\frac{\partial^2 p}{\partial y^2}=$$

$$\frac{\frac{h^3(i,j+1)}{12\eta(i,j+1)}-\frac{h^3(i,j-1)}{12\eta(i,j-1)}}{y(j+1)-y(j-1)}\frac{p(i,j+1)-p(i,j-1)}{y(j+1)-y(j-1)}+\frac{h(i,j)^3}{12\eta(i,j)}\frac{p(i,j+1)-2p(i,j)+p(i,j-1)}{\left(y(j+1)-y(j)\right)\left(y(j)-y(j-1)\right)}$$

Shear flow term

$$\frac{U}{2}\frac{\partial h}{\partial x}=\frac{U}{2}\frac{h(i+1,j)-h(i-1,j)}{x(i+1,j)-x(i-1,j)}$$

Squeeze motion term

$$\frac{\partial h}{\partial t}=\frac{h(i,j)-h_{prev}(i,j)}{\Delta t}=dhdt(i,j) \tag{49}$$

where $h_{prev}(i,j)$ is the value of film thickness at the previous time step (for transient solutions). Substituting all the above terms into Eq. (28), and setting the auxiliary variable $\mathrm{var}(i,j)=\frac{h^3(i,j)}{12\mu(i,j)}$, the following equation is derived:

$$\frac{\mathrm{var}(i+1,j)-\mathrm{var}(i-1,j)}{x(i+1)-x(i-1)}\frac{p(i+1,j)-p(i-1,j)}{x(i+1)-x(i-1)}+\mathrm{var}(i,j)\frac{p(i+1,j)-2p(i,j)+p(i-1,j)}{\big(x(i+1)-x(i)\big)\big(x(i)-x(i-1)\big)}+$$

$$+\frac{\mathrm{var}(i,j+1)-\mathrm{var}(i,j-1)}{y(j+1)-y(j-1)}\frac{p(i,j+1)-p(i,j-1)}{y(j+1)-y(j-1)}+\mathrm{var}(i,j)\frac{p(i,j+1)-2p(i,j)+p(i,j-1)}{\big(y(j+1)-y(j)\big)\big(y(j)-y(j-1)\big)}=$$

$$=\frac{U}{2}\frac{h(i+1,j)-h(i-1,j)}{x(i+1)-x(i-1)}+\frac{h(i,j)-h_{prev}(i,j)}{\Delta t} \tag{50}$$

The next step is to transform Eq. (50) in the following form:

$$Ap(i+1,j)+Bp(i-1,j)+Cp(i,j+1)+Dp(i,j-1)+Ep(i,j)=F \tag{51}$$

A, B, C, D, E and F are given by the following equations:

$$A(i,j)=\frac{\mathrm{var}(i+1,j)-\mathrm{var}(i-1,j)}{\big(x(i+1)-x(i-1)\big)\big(x(i+1)-x(i-1)\big)}+\frac{\mathrm{var}(i,j)}{\big(x(i+1)-x(i)\big)\big(x(i)-x(i-1)\big)}$$

$$B(i,j)=-\frac{\mathrm{var}(i+1,j)-\mathrm{var}(i-1,j)}{\big(x(i+1)-x(i-1)\big)\big(x(i+1)-x(i-1)\big)}+\frac{\mathrm{var}(i,j)}{\big(x(i+1)-x(i)\big)\big(x(i)-x(i-1)\big)}$$

$$C(i,j)=\frac{\mathrm{var}(i,j+1)-\mathrm{var}(i,j-1)}{\big(y(j+1)-y(j-1)\big)\big(y(j+1)-y(j-1)\big)}+\frac{\mathrm{var}(i,j)}{\big(y(j+1)-y(j)\big)\big(y(j)-y(j-1)\big)}$$

$$D(i,j)=-\frac{\mathrm{var}(i,j+1)-\mathrm{var}(i,j-1)}{\big(y(j+1)-y(j-1)\big)\big(y(j+1)-y(j-1)\big)}+\frac{\mathrm{var}(i,j)}{\big(y(j+1)-y(j)\big)\big(y(j)-y(j-1)\big)}$$

$$E(i,j)=-\frac{2\,\mathrm{var}(i,j)}{\big(x(i+1)-x(i)\big)\big(x(i)-x(i-1)\big)}-\frac{2\,\mathrm{var}(i,j)}{\big(y(i+1)-y(i)\big)\big(y(i)-y(i-1)\big)}$$

$$F(i,j)=\frac{U}{2}\frac{h(i+1,j)-h(i-1,j)}{x(i+1)-x(i-1)}+dhdt(i,j)$$

Finally, the pressure at the point (i,j) is calculated by solving Eq. (51) for p(i,j):

$$p(i,j)=\frac{F-Ap(i+1,j)-Bp(i-1,j)-Cp(i,j+1)-Dp(i,j-1)}{E} \tag{52}$$

3.2 Solution algorithm

The present study aims at developing and implementing an algorithm capable of solving the problem of hydrodynamic lubrication for the piston rings of internal combustion engines. At the start of the solution process, all the necessary details of the piston ring (geometry, operational conditions, solver details, discretization parameters, number of engine cycles, points per cycle etc) are read by an input file supplied by the user. At each time step, first, the external force acting on the piston rings needs to be calculated. To this end, the force due to

pressure acting on the back face of the piston ring, and the pretension force of the ring should be taken into account. Here, the pressure at the back face of the ring is assumed to be the maximum of the leading and trailing ring pressure values. Next, an initial estimation of minimum film thickness, h_{min}, is made, and the geometry of the lubricant domain is computed, using Eq. (47).

The Reynolds equation is solved over the lubricant domain with the Gauss-Seidel iterative method, and pressure distribution over the ring face is calculated. In the peripheral direction (direction y), symmetric conditions are assumed (one-dimensional problem). Using a second order Newton-Raphson method, an appropriate value of h_{min} is sought for which equilibrium is attained between the load capacity of the lubricating film (integration of pressure over the ring face) and the external ring force, which finally results in the minimum film thickness. In this way the piston ring motion in the z-direction (Fig. 22) is taken into consideration. At the first time step the squeeze film term of the Reynolds equation (dh/dt) is neglected, whereas at the next time steps, it is calculated by means of Eq. (49). Therefore, squeeze film motion is taken into account, and it is shown that it alters substantially the results compared to those obtained by considering the steady state phenomenon. After equilibrium has been reached for each time step, all the operational indices of the ring can be calculated, including friction force, power loss, friction coefficient, etc. A Simpons's integration rule is utilized here for maximum accuracy. The solution ends when all the time steps of the engine cycles that were selected by the users are solved.

For the solution of the Reynolds equation, four different solvers are developed in order to cover all the cases studied in the present work. The equations solved are the following: (a) Reynolds equation with Reynolds boundary condition (§2.2.5, Eq. (28)), (b) Reynolds equation for hydrophobic surface with Reynolds boundary condition (§2.4.2, Eq. (45)), (c) Reynolds equation with the Elrod-Adams mass conservation model (§3.2, Eq.(111)) and (d) Reynolds equation for hydrophobic surfaces with the Elrod-Adams mass conservation model (§3.3.2).

The algorithm of the present work was developed with the object oriented programming language C++ and the results were post processed with the MATLAB software.

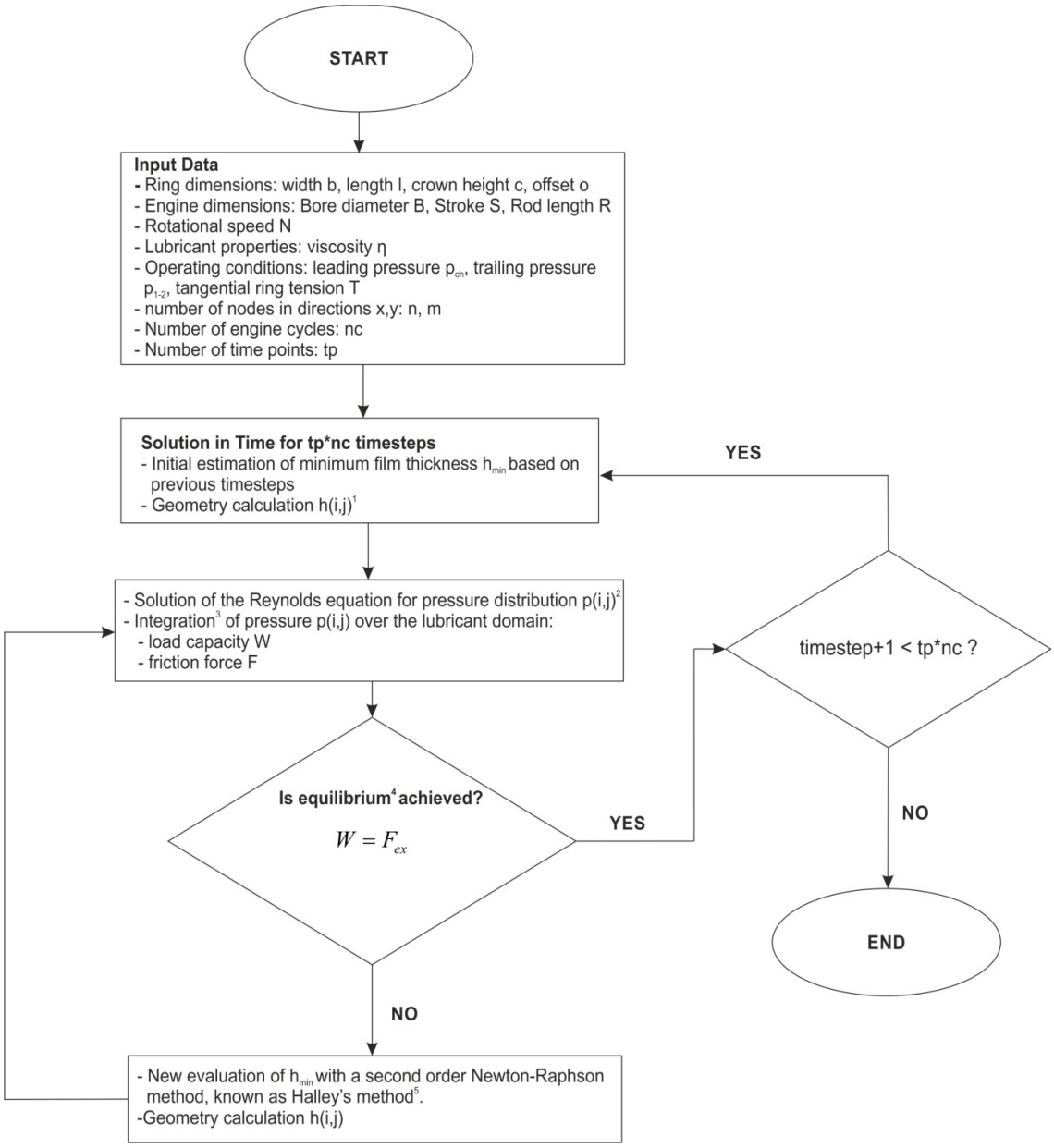

Fig. 24. Transient hydrodynamic lubrication in piston rings: solution algorithm.

Notes:

1. Based on the known piston ring profile geometry, film thickness is calculated:

$$h(i,j) = h_s(i,j) + h_{\min}$$

2. The Reynolds equation is solved for pressure with the Gauss-Seidel iterative numerical method.
3. Integration of quantities over the lubricant domain is performed using the Simpson rule. Load capacity and friction force are calculated by:

$$W = \int_0^l \int_0^b p\,dx\,dy$$

$$F = \int_0^l \int_0^b \left(\frac{h}{2}\frac{dp}{dx} - \frac{\eta U}{h} \right) dx\,dy$$

4. At each time step (crank angle), the external ring forces must be balanced by the hydrodynamic forces generated in the lubricating film. The external forces acting on the ring are the elastic pretension force and the force on the back face of the ring due to gas pressure:

$$P_{el} = \frac{2T}{b \cdot B}(b \cdot l)$$

$$P_{bk} = \max(p_{ch}, p_{1-2}) \cdot (b \cdot l)$$

$$F_{ext} = P_{el} + P_{bk}$$

where p_{ch} is the combustion chamber pressure and p_{1-2} is the pressure between the first and the second piston rings

5. At each time step, the value of h_{min} for which force equilibrium of the ring is reached is calculated by means of a second order Newton-Raphson method, also called Halley's method. Equilibrium is reached when:

$$f(h_{\min}) = \left| W(h_{\min}) - F_{ext} \right|$$

where $W(h_{min})$ is the hydrodynamic force acting on the ring at a value of minimum film thickness h_{min}, and F_{ext} is the external ring force.

The first and second derivatives of function $f(h_{min})$ are calculated as follows:

$$dh_{\min} = 0.05 h_{\min}$$

$$f(h_{\min} - dh_{\min}) = abs\left[W(h_{\min} - dh_{\min}) - F_{ext} \right]$$

$$f(h_{\min} + dh_{\min}) = abs\left[W(h_{\min} + dh_{\min}) - F_{ext} \right]$$

$$f'(h_{\min}) = \frac{f(h_{\min}) - f(h_{\min} - dh_{\min})}{dh_{\min}}$$

$$f''(h_{\min}) = \frac{f(h_{\min} + dh_{\min}) - 2f(h_{\min}) + f(h_{\min} + dh_{\min})}{dh_{\min}^{\,2}}$$

The new approximation of h_{min}, following the Halley's method, can be calculated as:

$$h_{\min,new} = h_{\min} - 2\frac{f(h_{\min})f'(h_{\min})}{2f'(h_{\min})^2 - f(h_{\min})f''(h_{\min})}$$

3.3 Algorithm solvers

As stated earlier, the C++ algorithm developed within the course of the present study, includes four different solvers. The equations solved are the following:

1. Reynolds equation with Reynolds boundary conditions
2. Reynolds equation for hydrophobic surfaces with Reynolds boundary conditions
3. Reynolds equation with the Elrod-Adams mass conservation model
4. Reynolds equation for hydrophobic surfaces with the Elrod-Adams mass conservation model

The solution algorithm presented in Fig. 24 is used by all solvers; the only difference is that for calculation of pressure in the lubricant domain, a different form of the Reynolds equation is utilized.

The simple Reynolds equation and the modified Reynolds equation to account for hydrophobic surfaces have been presented in sections 2.2.5 (Eq. (28)) and 2.4.2 (Eq. (45)), respectively. The latter is written in a general form to account for non-zero values of critical shear stress $\tau_{C,r}$ and $\tau_{C,l}$ of the ring and the liner. In the present work, these values have been taken as zero, therefore any non-zero local shear stress at the fluid-solid interface of a hydrophobic surface will include fluid slip over that surface. Taking this into account, Eq. (45) can be simplified as follows:

$$\frac{\partial}{\partial x}\left(\frac{h^2}{12\mu}\frac{\theta p}{\theta x}\frac{h^2+4\mu(a_l+a_r)h+12\mu^2 a_l a_r}{h+\mu(a_l+a_r)}\right)+\frac{\partial}{\partial y}\left(\frac{\partial p}{\partial y}\frac{h^2}{12\mu}\frac{h^2+4\mu h(a_r+a_l)+12a_l a_r\mu^2}{h+\mu(a_r+a_l)}\right)=$$

$$=\frac{U}{2}\frac{\partial}{\partial x}\left(\frac{h^2+2\mu a_r h}{h+\mu(a_l+a_r)}\right)-U\frac{\mu a_r}{h+\mu(a_l+a_r)}\frac{\partial h}{\partial x}+\frac{h}{2\mu}\frac{\mu a_r h+2a_l a_r\mu^2}{h+\mu(a_l+a_r)}\left(\frac{\partial h}{\partial x}\frac{\theta p}{\theta x}+\frac{\partial p}{\partial y}\frac{\partial h}{\partial y}\right)+\frac{\partial h}{\partial t} \quad (53)$$

The finite difference method, presented in section 3.1, can be used for the numerical solution of the two forms of the Reynolds equation.

3.3.1 Reynolds equation with the Elrod-Adams mass conservation model

Introduction

The problem of cavitation is a key concern in problems of hydrodynamic lubrication. Several researchers have worked on this subject, and many different numerical methods handling this phenomenon have been proposed. In the present work, the well-known Elrod's cavitation algorithm [8] has been used.

As mentioned in Section 2.3, the lubrication area is divided into two zones. The first one is the pressurized (active) zone, where the film is fully developed, and the Reynolds equation applies. The second is the cavitation (passive) zone, where only a fraction θ of the gap is occupied with oil, therefore finger-like striations of liquid and gas are observed.

Here, a universal equation for both the active and the passive zone is used, containing the fractional film content variable θ. In the active zone, the mass content per unit film area is $\rho_c h$, where ρ_c is the lubricant oil density at cavitation pressure p_c and h is the film thickness. In the passive zone, the lubricant density is constant and equal to ρ_c but the mass content is now $\rho_c \theta h$. In the active zone, density varies due to the pressure distribution, meaning that the oil is considered slightly compressible and the mass content is higher than that corresponding to cavitation pressure p_c. Consequently the fractional film content θ is equal to ρ/ρ_c.

Analytical Formulation

The two dimensional Reynolds equation can be written as follows, and it fully applies to the full film region:

$$\frac{\partial}{\partial x}\left(\frac{\rho h^3}{12\eta}\frac{\partial p}{\partial x}\right)+\frac{\partial}{\partial y}\left(\frac{\rho h^3}{12\eta}\frac{\partial p}{\partial y}\right)=\frac{U}{2}\frac{\partial(\rho h)}{\partial x}+\frac{\partial(\rho h)}{\partial t} \tag{54}$$

The lubricant oil density is related to the film pressure through the bulk modulus definition:

$$\beta=\rho\frac{\partial p}{\partial \rho} \tag{55}$$

It is easier to work with the universal variable θ, which is equal to the fractional film content (ratio of density along the film area and the density at the cavitation pressure). Variable θ takes values slightly above unity in the full film region, because of the relative compression of the lubricant as explained above. In the cavitation region, θ takes values below unity, as it further explained. The lubricant oil density in the cavitation region is constant and equal to ρ_c, but the liquid occupies only a portion of the gap, meaning that the actual mass content is $\rho_c \theta h$.

Consequently, variable θ can be defined as:

$$\theta=\frac{\rho}{\rho_c}\ ,\ \theta=\begin{cases}>1 \text{ in the full film region}\\ <1 \text{ in the cavitation region}\end{cases} \tag{56}$$

Due to the fact that the film pressure is constant in the cavitation region, a switch function is introduced in the pressure-density relation, in order to exclude the pressure terms in the cavitation region, and keep only the Couette flow term:

$$g\beta = \rho\frac{\partial p}{\partial \rho} = \theta\frac{\partial p}{\partial \theta},$$
$$g = \begin{cases} 1 \text{ in the full film region} \\ 0 \text{ in the cavitation region} \end{cases} \tag{57}$$

By directly integrating Eq. (57), the expression of pressure is yielded:

$$p = p_c + g\beta \ln\theta \tag{58}$$

Replacing Eq. (58) in Eq. (54) yields:

$$\frac{\partial}{\partial x}\left(\frac{g(\theta)\beta h^3}{12\eta}\frac{\partial \theta}{\partial x}\right) + \frac{\partial}{\partial y}\left(\frac{g(\theta)\beta h^3}{12\eta}\frac{\partial \theta}{\partial y}\right) = \frac{U}{2}\frac{\partial(\theta h)}{\partial x} + \frac{\partial(\theta h)}{\partial t} \tag{59}$$

The finite difference form of Eq. (59) is presented in Eq. (60). The derivation of Eq. (60) is presented in detail in Appendix B.

$$\begin{aligned}
&\left[\frac{\beta}{12\eta\Delta x^2}g(i+1,j)h\left(i+1/2,j\right)^3\right]\theta(i+1,j) + \left[\frac{\beta}{12\eta\Delta x^2}g(i-1,j)h\left(i-1/2,j\right)^3 + \frac{U}{2\Delta x}h(i-1,j)(1-g(i-1,j))\right]\theta(i-1,j) \\
&+\left[\frac{\beta}{12\eta\Delta y^2}g(i,j+1)h\left(i,j+1/2\right)^3\right]\theta(i,j+1) + \left[\frac{\beta}{12\eta\Delta y^2}g(i,j-1)h\left(i,j-1/2\right)^3\right]\theta(i,j-1) \\
&+\left[-\frac{\beta}{12\eta\Delta x^2}g(i,j)\left(h\left(i+1/2,j\right)^3 + h\left(i-1/2,j\right)^3\right) - \frac{\beta}{12\eta\Delta y^2}g(i,j)\left(h\left(i,j+1/2\right)^3 + h\left(i,j-1/2\right)^3\right) - \left(\frac{dh}{dt} + \frac{3h(i,j)}{2\Delta t}\right)\right]\theta(i,j) = \\
&= \frac{\beta}{12\eta\Delta x^2}\left(g(i+1,j)h\left(i+1/2,j\right)^3 - g(i,j)\left(h\left(i+1/2,j\right)^3 + h\left(i-1/2,j\right)^3\right) + g(i-1,j)h\left(i-1/2,j\right)^3\right) \\
&+\frac{\beta}{12\eta\Delta y^2}\left(g(i,j+1)h\left(i,j+1/2\right)^3 - g(i,j)\left(h\left(i,j+1/2\right)^3 + h\left(i,j-1/2\right)^3\right) + g(i,j-1)h\left(i,j-1/2\right)^3\right) \\
&-\frac{U}{2\Delta x}\left[\frac{g(i-1,j)h(i-1,j)}{2}\left(2-g(i,j)\right) + \frac{g(i,j)h(i,j)}{2}\left(g(i-1,j)-2+g(i+1,j)\right) - \frac{g(i+1,j)g(i,j)h(i+1,j)}{2}\right] \\
&+h(i,j)\frac{-4\theta(i,j)\big|_{t-1} + \theta(i,j)\big|_{t-2}}{2\Delta t}
\end{aligned} \tag{60}$$

3.3.2 Reynolds equation for hydrophobic surfaces with the Elrod-Adams mass conservation algorithm

This fourth solver developed within the course of the present study is a combination of the solver for the Reynolds equation for hydrophobic surfaces (section 3.3) and of the solver for the Elrod-Adams mass conservation model (section 3.3.1). In brief the equation was derived starting from Eq. (111), and modifying it appropriately to account for hydrophobicty at the stator and rotor surfaces, see Eq. (38) and (39). The derived equation was solved with the same finite differencing scheme as that used in 3.3.1, which is central difference in the pressure region and backward difference in the cavitation region.

3.4 Validation of the solution algorithms

The solution algorithms presented in the previous sections are now validated against numerical results published in the international literature. In order to validate all the features of the present development, different sets of geometries and boundary conditions have been considered. These are presented in the following sections:

3.4.1 Reynolds equation

The results of the Reynolds equation algorithm are validated by comparing the calculated operational characteristics of a piston ring with those published by Jeng et al. [4]. In particular, calculations have been performed for the first compression ring of a four-stroke Diesel engine, using the Reynolds equation. The engine geometric and operational characteristics are:

- Bore, B= 88.9 mm
- Stroke, S= 80 mm
- Rod length, R= 141.9 mm
- Composite roughness, r= 0.37 mm
- Viscosity, η= 0.00689 Pa·s
- Speed, N= 2000 rpm
- Dry friction coefficient (metal to metal), f= 0.08
- First compression ring details
    - Width, b= 1.47 mm
    - Crown height, c= 14.9 μm
    - Offset, o= 0 μm
    - Tangential ring tension force, T= 14.05 N

In Fig. 25, the computed performance parameters (minimum film thickness, friction force and power loss) are plotted against the corresponding results of Jeng et al. A very good agreement is observed for all the presented comparisons. The maximum deviation in minimum film thickness is 4%, mainly observed for values of crank angle (CA) less than 180^o. At higher CA

values, the deviation is less than 0.7%. The same trend is observed for the other two plotted quantities (power loss and friction force), with maximum deviation at values of CA higher than 180^o being less than 3%.

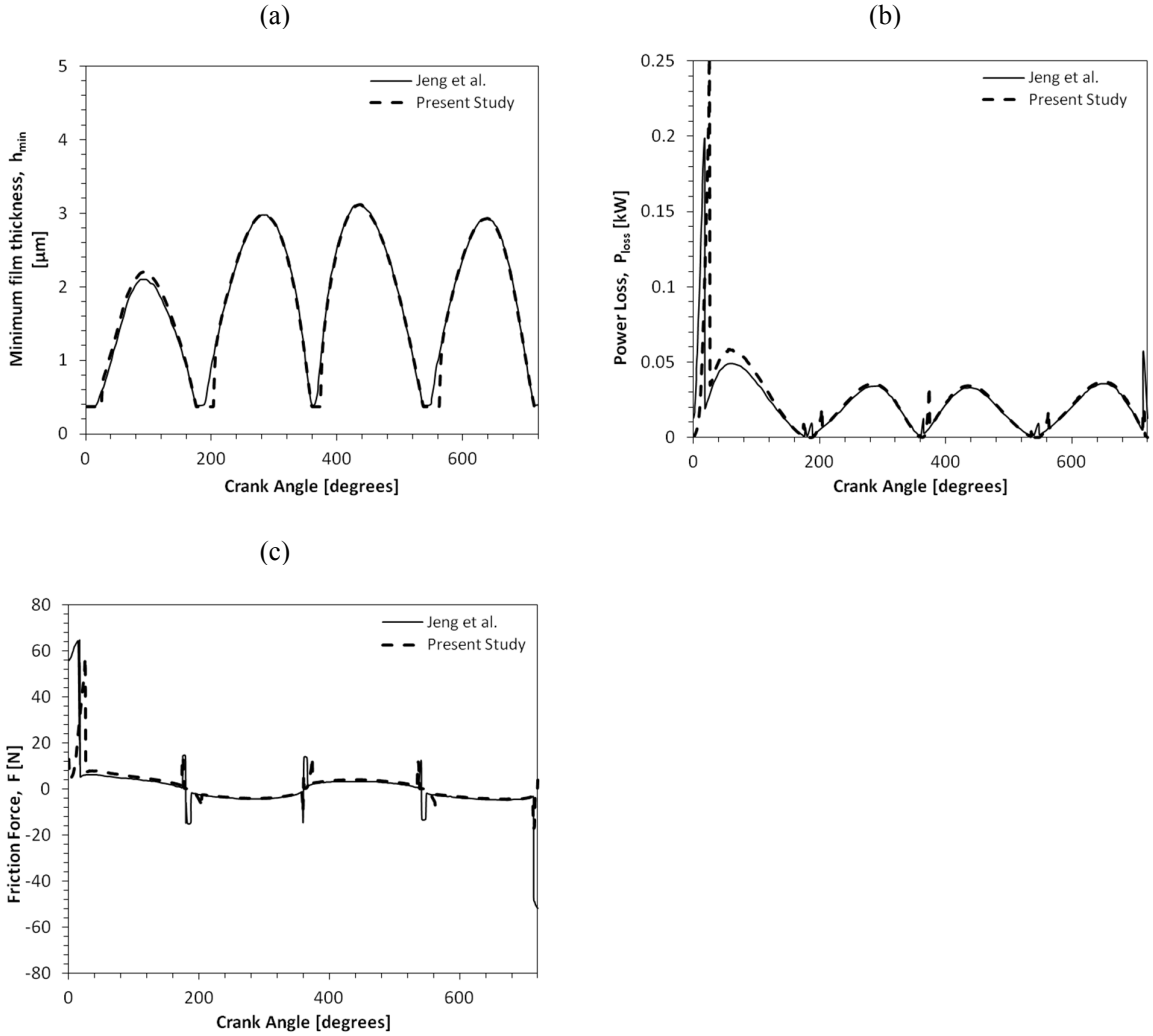

Fig. 25. (a) Minimum film thickness, (b) power loss, and (c) friction force against crank angle: Comparison between the present results, and those of Jeng et al. [4].

3.4.2 Reynolds equation with the Elrod-Adams cavitation model

The developed solution algorithm of the Reynolds equation using the Elrod-Adams mass conservation model is validated against the results of two publications, namely those of Giacopini et al. [11] and Xiong et al. [17].

Models by Giacopini et al. [11]

The first three validation cases refer to a pure slider with a sinusoid varying geometry. In particular, the first slider has a converging-diverging geometry with zero pressure at both boundaries, the second one is of the same geometry, but with pressure of 1 MPa at the slider

boundaries, whereas the third slider has a diverging-converging geometry and pressure of 1 MPa at the slider boundaries. Hereinafter, the basic geometric and operational characteristics of the sliders are presented:

- Slider length, b= 125 mm
- Maximum film thickness, h_{max}= 0.025 mm
- Minimum film thickness, h_{min}= 0.015 mm
- Viscosity, η= 0.015 Pa·s
- Speed, U= 4 m/s

In Fig. 26, the film thickness of each slider is presented along with the corresponding pressure distribution, using both the Reynolds equation and the Reynolds equation in conjunction with the Elrod mass conservation model.

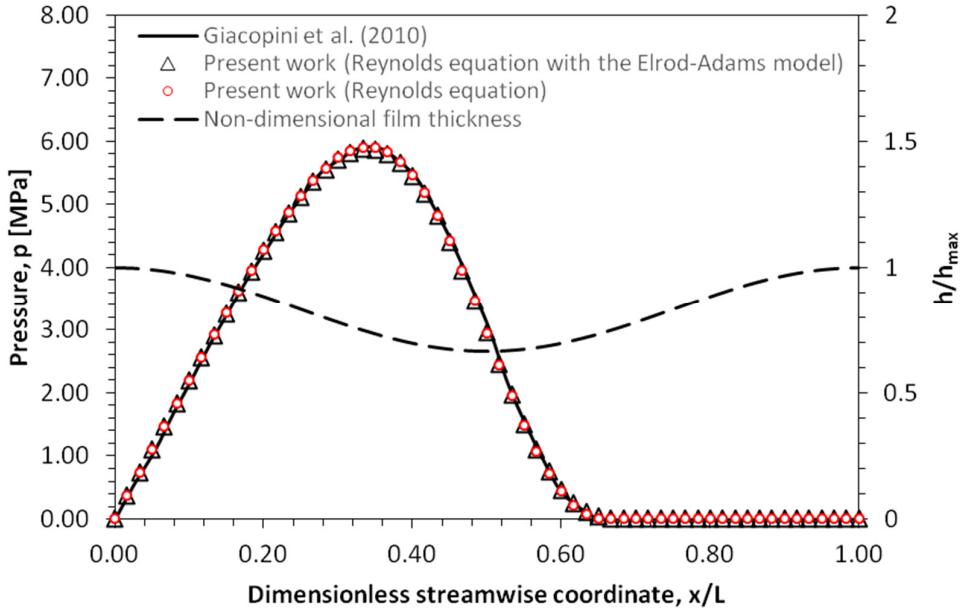

Fig. 26. Converging-diverging slider with zero pressure at the slider boundaries: Film thickness shape and corresponding pressure distribution calculations by (a) Giacopini et al. [11], (b) the present Reynolds equation solver and (c) the present solver of the Reynolds equation with the Elrod-Adams mass conservation model.

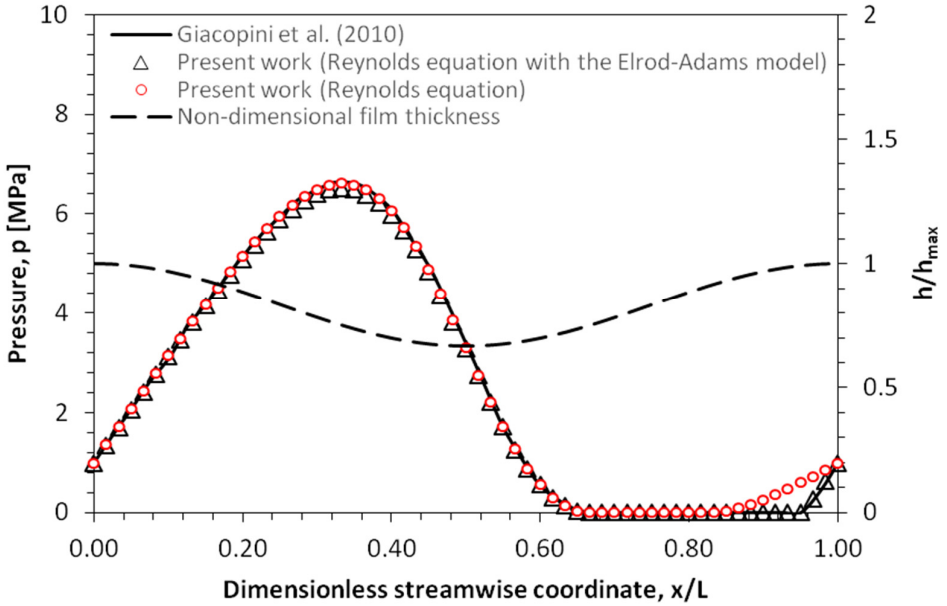

Fig. 27. Converging-diverging slider with 1 MPa pressure at the slider boundaries: Film thickness shape and corresponding pressure distribution calculations by (a) Giacopini et al. [11], (b) the present Reynolds equation solver and (c) the present solver of the Reynolds equation with the Elrod-Adams mass conservation model.

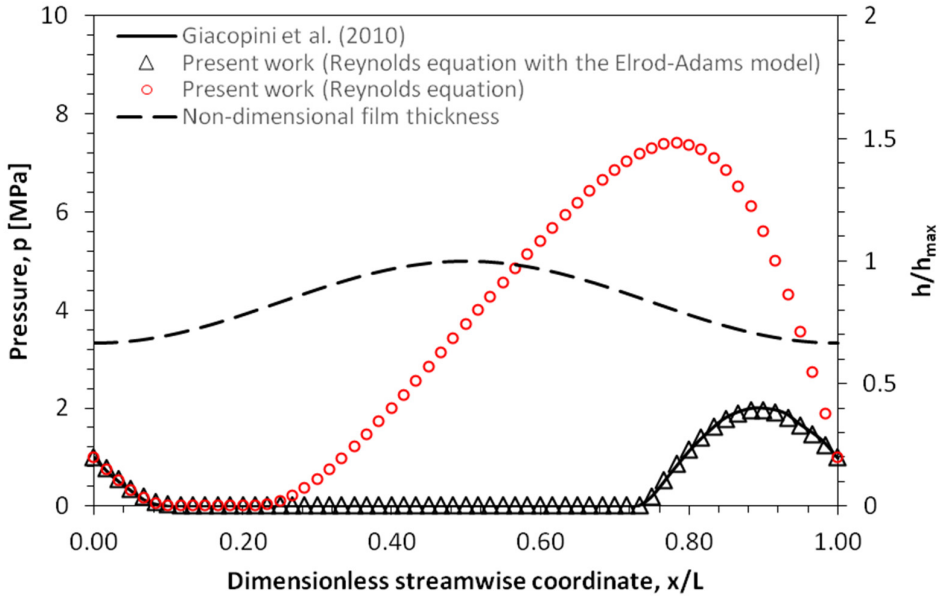

Fig. 28. Diverging-converging slider with 1 MPa pressure at the slider boundaries: Film thickness shape and corresponding pressure distribution calculations by (a) Giacopini et al. [11], (b) the present Reynolds equation solver and (c) the present solver of the Reynolds equation with the Elrod-Adams mass conservation model.

A very good agreement can be observed between the computations of the present Elrod-Adams mass conservation model and the corresponding results of Giacopini et al., for all the sliders considered. The Reynolds equation making use of the Reynolds boundary conditions is only suitable for the first case (Fig. 26). As for the second case, the classic Reynolds equation underestimates the extent of the cavitation region, while the Elrod-Adams algorithm properly predicts the instant pressure regain at the outflow region (Fig. 27). Finally, in the third test case, computations with the use of the Reynolds equation are totally different in comparison to those made with the Elrod-Adams model; the pressure distribution computed with the use of the Reynolds equation develops very early, which is unrealistic, because the lubricant still cavitates even if it enters a converging geometry (Fig. 28). Consequently, in some cases, the use of the Elrod-Adams mass conservation model is imperative, because the classic Reynolds equation cannot properly predict the exact location of film rupture and reformation.

In all three cases, the deviations between computations with the present Elrod-Adams model and that of Giacopini et al. are less than 1%.

The next considered test case refers to a parallel slider containing a single pocket near the inflow region. In Fig. 29, a sketch of the slider is shown, and in Table 1, the corresponding geometric and operational characteristics are presented.

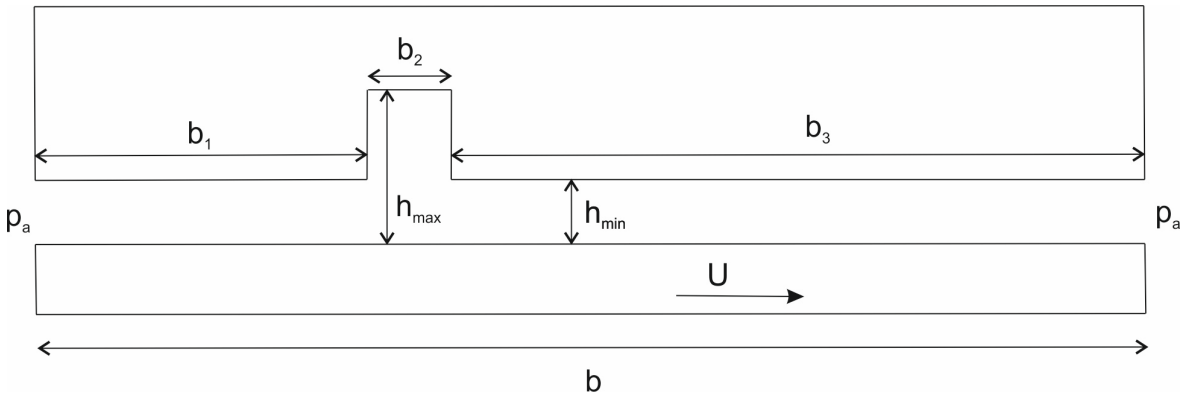

Fig. 29. Sketch of parallel slider with a single microtexture pocket.

b (mm)	b_1 (mm)	b_2 (mm)	b_3 (mm)	h_{max} (mm)	h_{min} (mm)	η (Pa·s)	U (m/s)	p_a (MPa)
20	2	3	15	0.010	0.001	0.01	1	0.1

Table 1. Geometrical and operational characteristics of the slider of Fig. 29.

In Fig. 30, the computed pressure profiles for this case is presented, where a very good agreement can be seen between the computations of the present work and those of Giacopini et al.

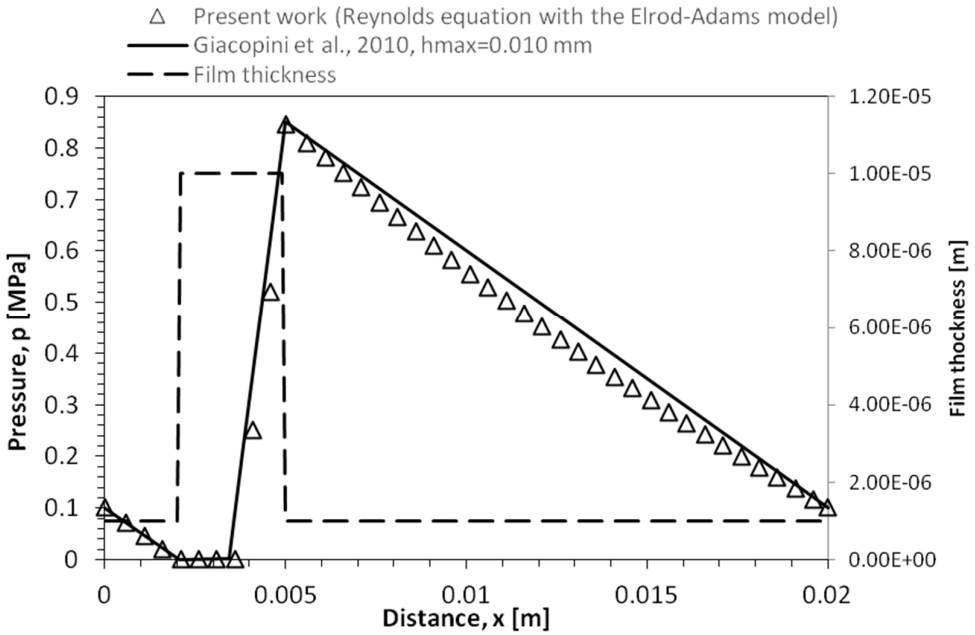

Fig. 30. Parallel slider with a single pocket and 0.1 MPa pressure at the boundaries: Film thickness shape and corresponding computed pressure distribution by (a) the present Reynolds equation solver, with the Elrod-Adams algorithm, and (b) Giacopini et al. [11].

Models by Xiong et al. [17]

A more detailed validation is needed for textured surfaces, because the film geometry variation is notably abrupt. To this end, two additional test cases where considered derived from the publication of Xiong et al. [17]. The utilized slider geometry is similar to that of the microtextured slider of Giacopini et al., see also Fig. 29. All the parameters are summarized in Table 2; they are exactly the same, except for texture depth. In the first test case of Xiong et al., the texture depth is two times the minimum film thickness, and the corresponding pressure distribution is shown in Fig. 31. In the second test case, the texture depth is four times the minimum film thickness, and the calculated pressure is shown in Fig. 32. The resulting pressure distribution of the present model is very close to those computed by Xiong et al., exhibiting a maximum deviation of approximately 0.7%.

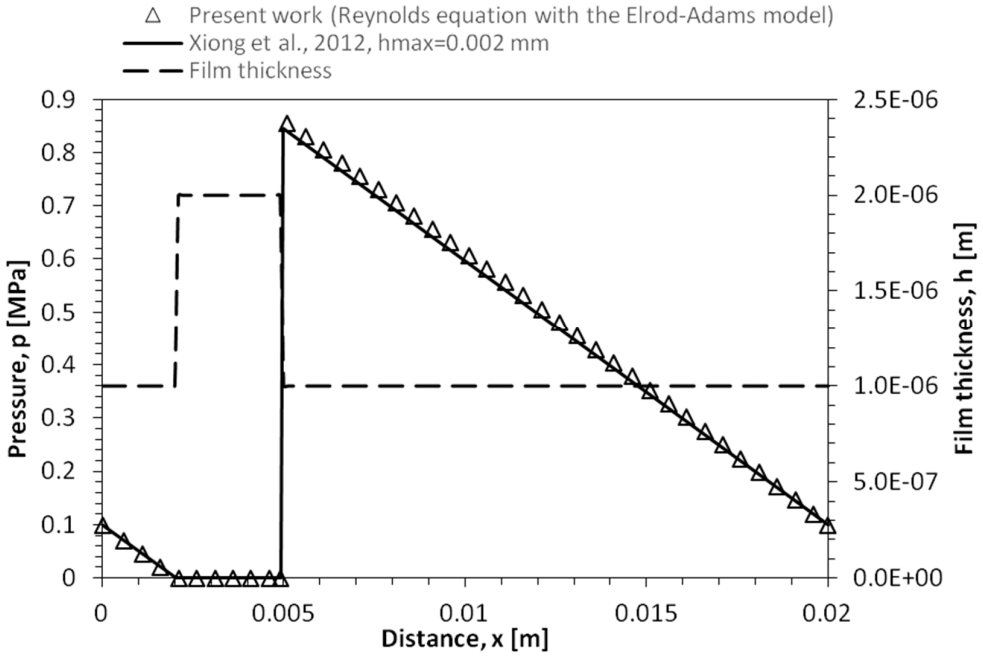

Fig. 31. Parallel slider with a single pocket and 0.1 MPa pressure at the boundaries: Pocket depth, $h_{max}=2 \cdot h_{min}$: Film thickness shape and corresponding computed pressure distribution by (a) the present Reynolds equation solver, with the Elrod-Adams algorithm, and (b) Xiong et al. [17].

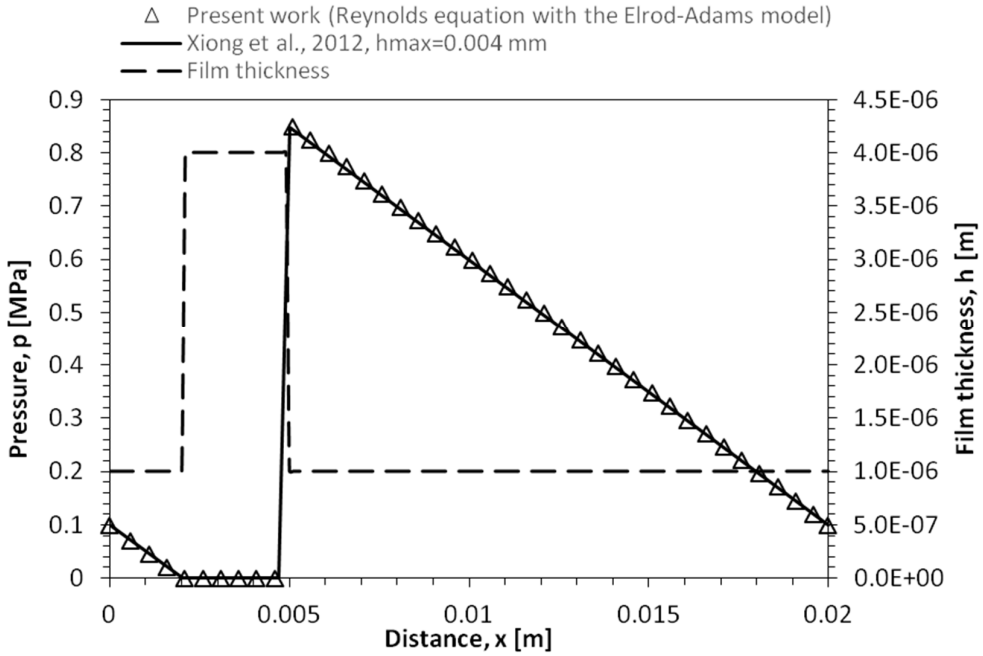

Fig. 32. Parallel slider with a single pocket and 0.1 MPa pressure at the boundaries: Pocket depth, $h_{max}=4 \cdot h_{min}$: Film thickness shape and corresponding computed pressure distribution by (a) the present Reynolds equation solver, with the Elrod-Adams algorithm, and (b) Xiong et al. [17].

Case	b (mm)	b_1 (mm)	b_2 (mm)	b_3 (mm)	h_{max} (mm)	h_{min} (mm)	η (Pa·s)	U (m/s)	p_a (MPa)
a.	20	2	3	15	0.002	0.001	0.01	1	0.1
b.	20	2	3	15	0.004	0.001	0.01	1	0.1

Table 2. Geometric and operational parameters of the slider studied by Xiong et al. [17].

3.4.3 Reynolds equation for hydrophobic surfaces

The Reynolds equation solver for hydrophobic surfaces was validated against three cases. The first test case corresponds to the one-dimensional slider of Pavlioglou et al. [13], the second one refers to the cases III and VII of the publication of GuoJun et al. [14], and the last one refers to two three-dimensional models solved with the ANSYS CFX software.

The basic parameter needed to define a slip surface is the non-dimensional slip length b^*, which is defined here as:

$b^* = \frac{b}{h_{\min}}$, where b is the slip length and h_{min} the minimum film thickness

The part of the stator with hydrophobic properties may be calculated if the non-dimensional parameter l_s is given, which is defined here as:

$l_s = \frac{L_s}{L}$, where L_s is the length of the hydrophobic part of the stator and L the slider length.

Model by Pavlioglou et al. [13]

The model of Pavliogou et al. [13] corresponds to a parallel slider with hydrophobicity at the inflow part of the stator. The slider has the following geometric and operational parameters:

- Slider length, b= 50 mm
- Film thickness, h= 0.05 mm
- Viscosity, η= 0.037 Pa·s
- Speed, U= 12 m/s
- Non-dimensional hydrophobic length, l_s= 0.85
- Non-dimensional slip length, b^*= 10

In Fig. 33, the pressure distribution of the slider, calculated with the model of the present study is validated against the calculations of Pavlioglou et al., exhibiting a very good agreement.

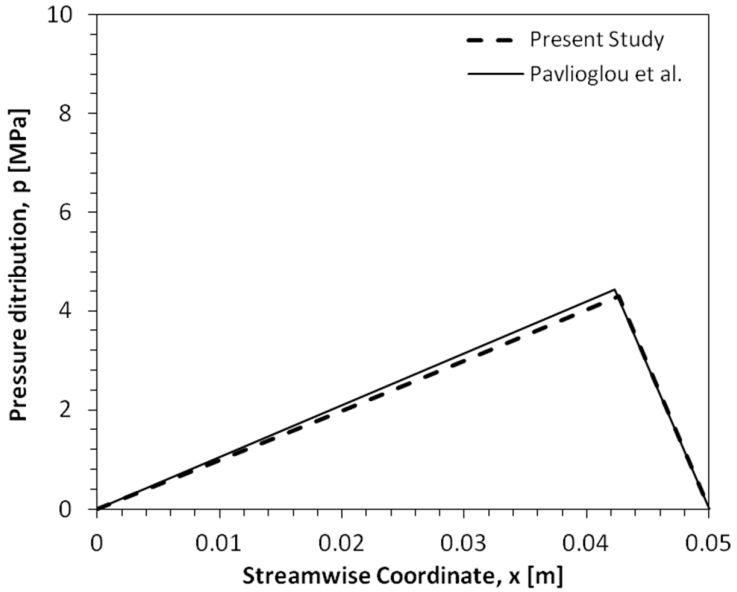

Fig. 33. Streamwise pressure distribution of the slider: comparison between result of the present work and those of Pavlioglou et al [13]. The considered slider is parallel with hydrophobicity at 85% of the slider length, starting from inflow.

Models by GuoJun et al. [14]

GuoJun et al., performed calculations for a two-dimensional converging slider with slip properties at a part of the stator surface. Two of their cases are selected in order to compare the results of the present study, case III and VII (see Fig. 34). In case III the slider has hydrophobic properties along the entire width and for a length of 55% of the slider length, starting from inflow. The slider corresponding to case VII has hydrophobic properties in a trapezoidal shape, defined by a length of 70% of the slider length and a transverse angle equal to 70°.

Case III

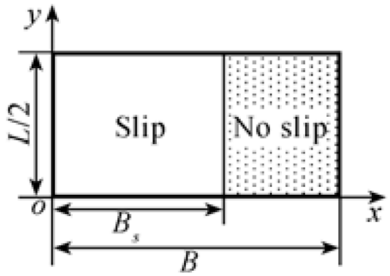

- $l_s = B_s/B = 0.55$
- $b^* = 100$

Case VII

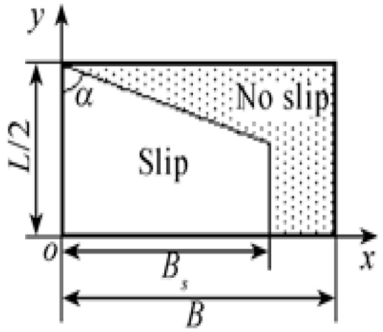

- $l_s = B_s/B = 0.7$
- $b^* = 100$
- $\alpha = 70^o$

Fig. 34. Sketch of the two three-dimensional sliders with hydrophobicity at part of the stator, studied by GuoJun et al. [14].

For the above two cases, the results of dimensionless load carrying capacity $\left(W^* = Wh_{\min} / (U\eta BL)\right)$ and dimensionless friction force $\left(F^* = Fh_{\min} / (U\eta BL)\right)$ are presented in Fig. 35 and Fig. 36 against convergence ratio $\left(k = h_{\max} / h_{\min} - 1\right)$. A very good agreement can be observed between the results of the present study and these of GuoJun et al., with deviation being less than 1% for W^* and 3% for F^*.

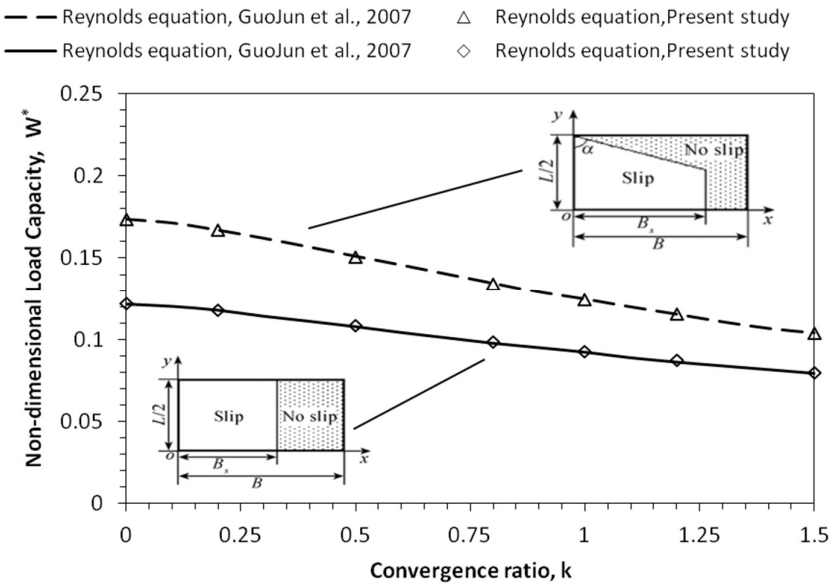

Fig. 35. Non-dimensional load capacity W^* against convergence ratio k for the cases depicted in the embodied sketches; comparison between the results of present study and those of GuoJun et al. [14].

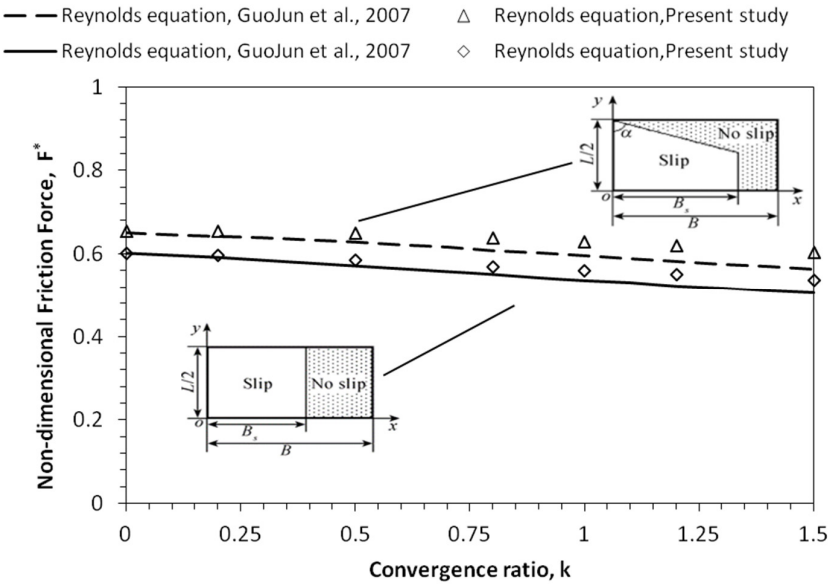

Fig. 36. Non-dimensional friction force F* against convergence ratio k for the cases depicted in the embodied sketches; comparison between the results of present study and those of GuoJun et al. [14].

ANSYS CFX models

In order to further examine the validity of the present algorithm solvers, two additional cases were studied, previously solved with the ANSYS CFX software. The first one is an alteration of the model used by Pavlioglou et al. [13] and refers to a 3-D converging slider with a value of b/l=1 and minimum film thickness h_{min}= 50 μm. The remaining parameters have been presented in detail in the paragraph where the models of Pavlioglou et al. have been considered. In Fig. 37 and Fig. 38, computations of maximum pressure and load carrying capacity with the solver of the present work are plotted against the CFX calculations for three different values of b^*. A very good agreement can be observed between the results of the present model and the CFD results.

The second model is also three-dimensional and corresponds to the case III of GuoJun et al. [14], which was also discussed previously. An identical model was introduced in CFX and calculations were performed for the non-dimensional load carrying capacity 'W^*' and the non-dimensional friction force 'F^*'. The CFD results were compared with calculations with the solver of the present study, and a very good agreement was observed, as seen in Fig. 39 and Fig. 40.

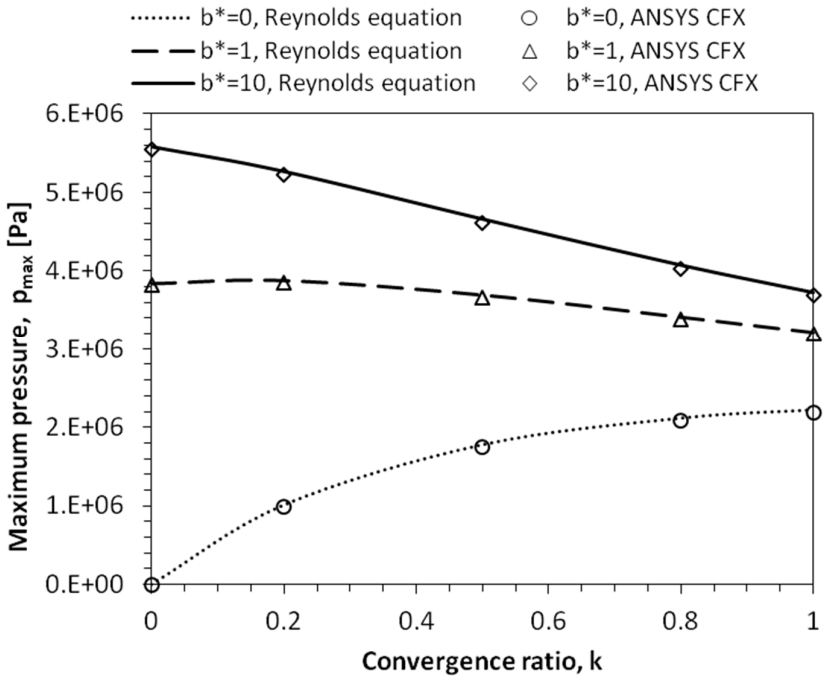

Fig. 37. Partially hydrophobic 3-D slider: Maximum pressure versus convergence ratio, for different values of non-dimensional slip length b^*. Comparisons between the computations of the present Reynolds equation solver and those with ANSYS CFX.

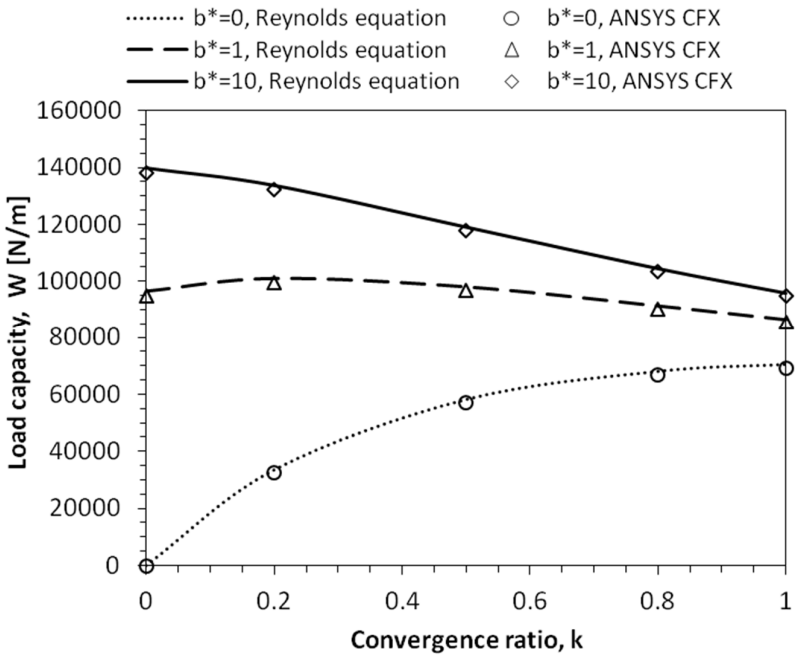

Fig. 38. Partially hydrophobic 3-D slider: Load capacity versus convergence ratio, for different values of non-dimensional slip length b^*. Comparisons between the computations of the present Reynolds equation solver and those with ANSYS CFX.

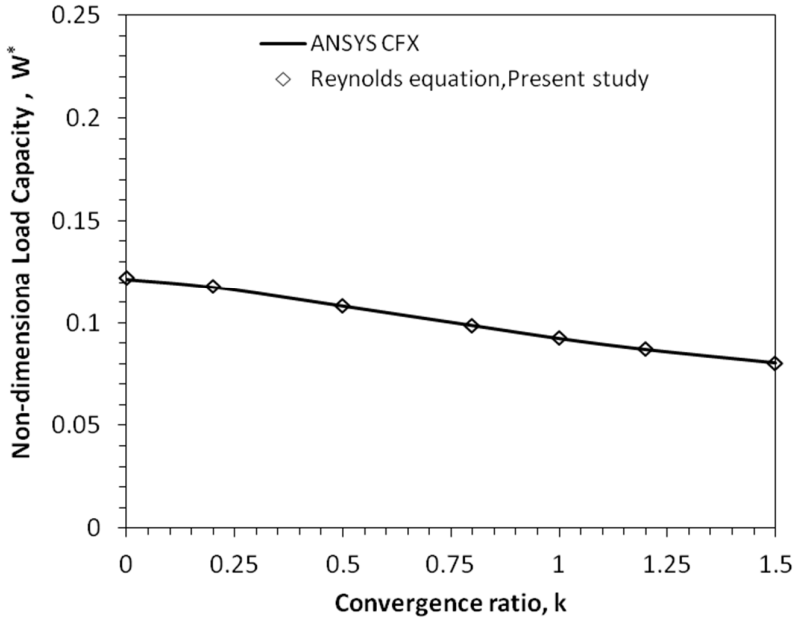

Fig. 39. Partially hydrophobic 3-D slider: Non-dimensional load carrying capacity versus convergence ratio. Comparison between CFD results and results of the present Reynolds equation solver.

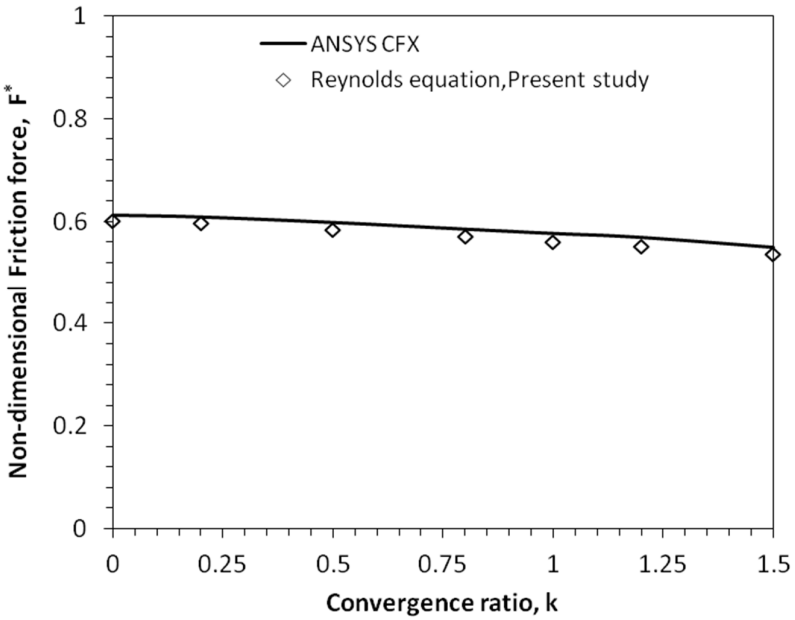

Fig. 40. Partially hydrophobic 3-D slider: Non-dimensional friction force versus convergence ratio. Comparison between CFD results and results of the present Reynolds equation solver.

4. Computational Results

4.1 Introduction

The algorithms developed within the present thesis are applied to compute the performance parameters of the first compression ring of a piston of a large two-stroke marine Diesel engine. The reference engine in this work is similar to the RT-flex58T-B engine by Wärtsilä. The principal characteristics of the engine are given in Table 3. For this engine two loading conditions are considered, one corresponding to power output equal to 100% of the engine MCR at the rotational speed of 105 RPM, and a second corresponding to power output equal to 25% of the engine MCR at a rotational speed of 66.1 RPM.

In Fig. 41, a sketch of the reference piston ring geometry studied in the present work is depicted. The geometry of the ring face is part of a parabola, characterized by the ring thickness, b, the crown height, c, and the offset value, o. The geometric parameters and mechanical characteristics of the reference piston ring are presented in Table 4. The top edge of the reference ring is assumed to be at a pressure equal to the combustion pressure of the engine. Pressure at the bottom edge of the ring (pressure between the first and the second ring) is assumed to be half of the combustion pressure.

At first, in section 4.2, the combustion chamber pressure history of the reference engine at the two engine loading conditions is presented, along with calculations of the piston speed. Next, calculations are performed for the reference piston ring design of Table 4. and a parametric analysis is performed, to identify the effect of the main design parameters of the ring on its performance characteristics.

Subsequently, part of the piston ring surface is assumed to have undergone surface treatment in the form of hydrophobicity or artificial surface texturing. The effect of those surface treatment technologies on the performance of the piston ring is computed for a reference design, and a detailed parametric analysis is performed to identify the optimum design parameter values. Finally, the results are analyzed and conclusions are drawn.

Reference engine	
Bore, B	580 mm
Stroke, S	2416 mm
Connecting rod length, R	2241 mm
Revolution speed, N • load 100% • load 25%	 105 RPM 66.1 RPM
Viscosity[1], η	0.19 Pa·s

Table 3. Geometric and operational characteristics of the reference engine

1. The cylinder oil of the reference engine is assumed to have a dynamic viscosity of 0.19 Pa·s at working conditions of the engine.

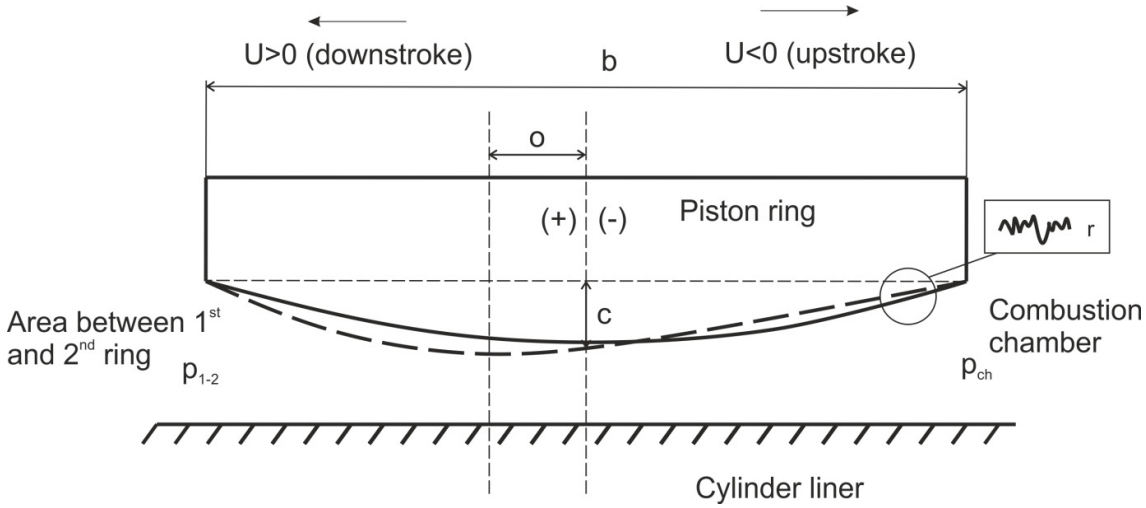

Fig. 41. Sketch of the first (top) compression piston ring.

First (top) compression piston ring	
Radial width	28 mm
Ring thickness, b	16 mm
Crown height[2], c	3 μm
Offset[2], o	0 μm
Composite roughness, r	0.2 μμ
Pretension force[3], T	49744 N

Table 4. Geometric parameters and mechanical characteristics of the reference piston ring of the present study.

2. The piston ring profile is assumed to be a parabola with offset, which is considered to describe adequately the profile after a certain period of engine running [4]. So the ring profile is represented by the following function:

$$h_s(x) = \frac{c}{\left(\frac{b}{2}+o\right)^2}(x-o)^2$$

3. According to [25] p.373, when the ring is slipped on the piston, stress in section AB (Fig. 42) can be calculated as:

$$\sigma_b' = 1.6E\left(\frac{h}{D-h+\frac{\lambda}{\pi}}\right) = 13.8 \text{ GPa}$$

where,

D≈ B= 580 mm

E= 170 GPa (Young's modulus of elasticity for cast iron)

λ≈ 0 mm, ring gap when the ring is slipped on the piston, which is practically zero, because the two ring ends are in contact.

The specific pressure acting on the liner walls is calculated from equation (342) of [114] and is considered to be uniformly distributed at the ring circumference (Fig. 42).

$$P_{sp} = \frac{\sigma_b' h^2}{3D^2} = 10.7 \text{ MPa}$$

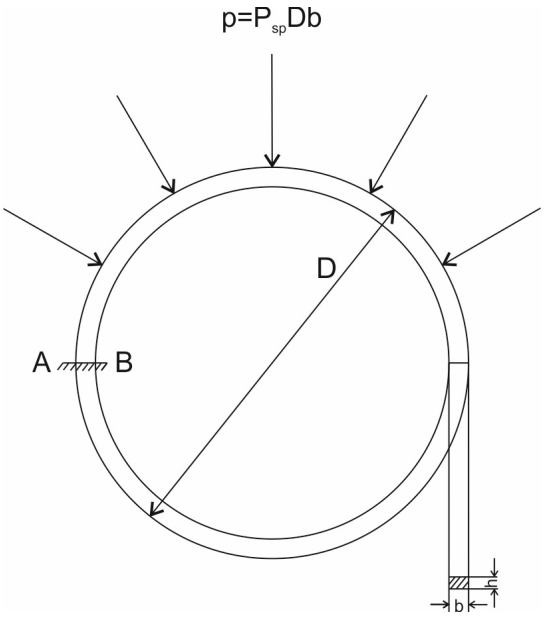

Fig. 42. Sketch of a piston ring and radial load from the liner wall.

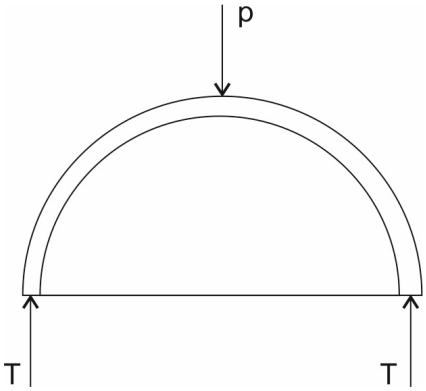

Fig. 43. Equilibrium of forces at half of the piston ring.

Considering the half ring as a simple beam the pretension force acting on the section AB is the result of force equilibrium in the model of Fig. 43:

$$T = \frac{p}{2} = \frac{P_{sp} Db}{2} = 49744 \text{ N}$$

4.2 Pressure and piston speed diagrams

The combustion chamber pressure over a full engine cycle is taken from Kontoulis et al. [28] and takes the values shown in Fig. 44, for two different engine operating conditions, one corresponding to engine load of 100% at a rotational speed of 105 RPM, and a second, corresponding to engine load of 25% at a rotational speed of 66.1 RPM. For the reference piston ring, the pressure between the first and second ring is assumed to be equal to the half of the combustion chamber pressure, according to Jeng et al. [4], and takes the values shown in Fig. 45. Fig. 46 presents the piston speed for the two different engine operating conditions mentioned above.

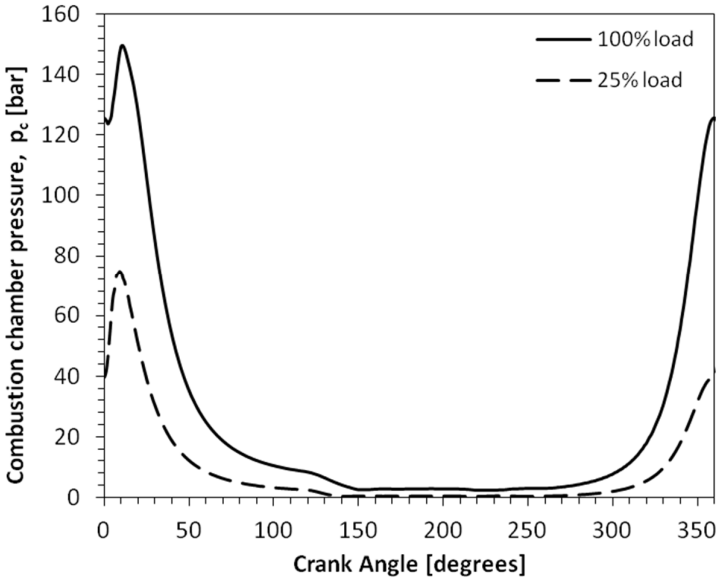

Fig. 44. Combustion chamber pressure versus crank angle for engine loads of 100% and 25%.

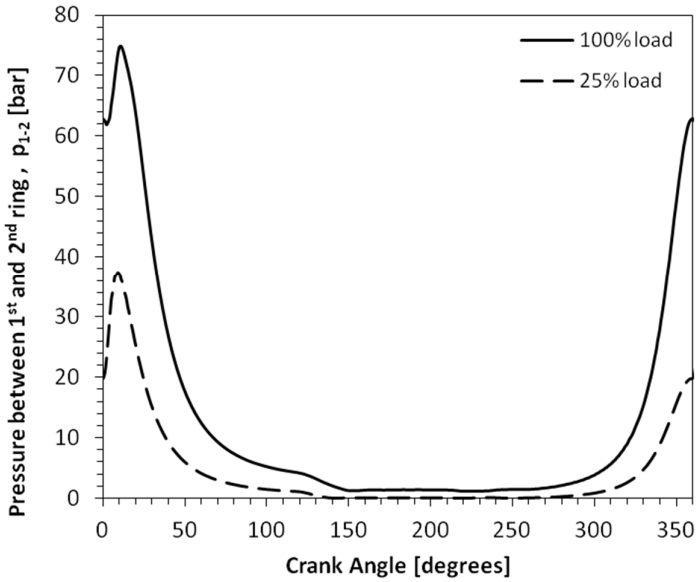

Fig. 45. Pressure in the space between the first and second piston rings versus crank angle for engine loads of 100% and 25%.

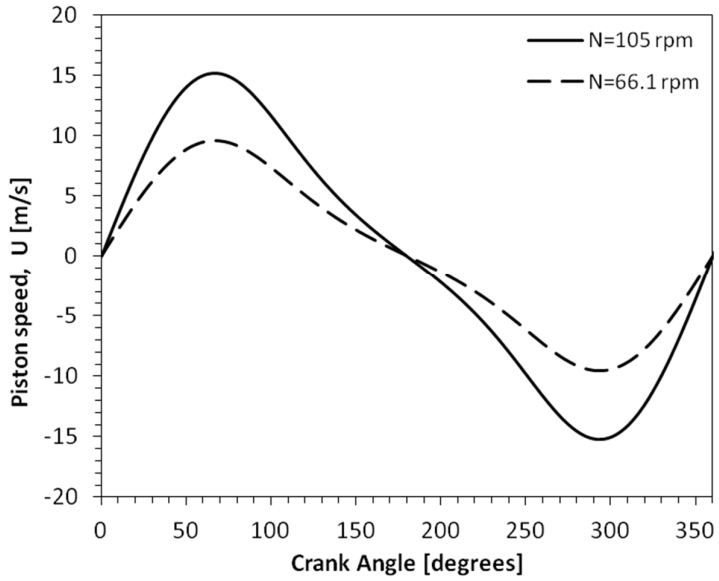

Fig. 46. Piston speed versus crank angle at 105 RPM (100% load) and 66.1 RPM (25% load).

4.3 Reference case

In the present section, the developed model is applied for the computation of the operational characteristics of the first compression ring of the reference engine of the present study. Two different loads are considered, namely that of 100% and that of 25% of the engine MCR. The geometrical and operational characteristics of both the engine and the piston ring have been presented in Table 3 and Table 4, respectively.

The developed algorithm solves the problem of hydrodynamic lubrication, making use of the Reynolds equation in conjunction with the Elrod-Adams mass conservation model. Firstly, a mesh study is performed to determine the appropriate grid details that yield mesh independent solution. Further, a study of the bulk modulus value is performed to identify its effect on the results, when the Elrod-Adams mass conservation model is used. Next, variation of the main geometrical and operational parameters of the reference piston ring is performed, and comparisons of the computed results are made. Finally, emphasis is given on the squeeze film terms of the Reynolds equation, which significantly affect the computational results.

4.3.1 Mesh study

In this section a mesh study is performed for the reference piston ring design, in order to choose the required number of grid points. The chosen grid size should provide results with negligible deviation from those computed with a very fine grid, and at the same time reasonable duration of solution. In the present study, following the results presented in Fig. 47, the selected mesh grid consists of 201 points along the x direction.

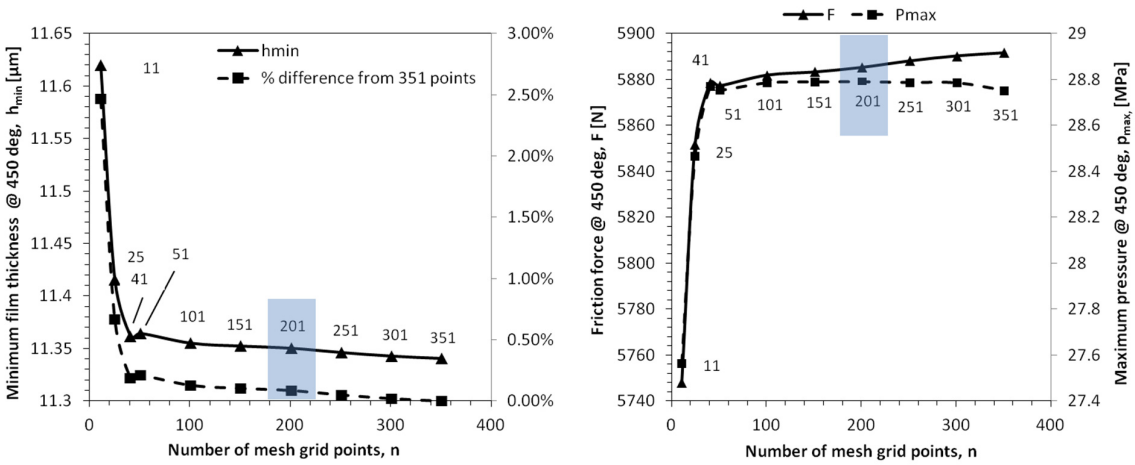

Fig. 47. Mesh study of the plain piston ring at 100% engine load. The parameters evaluated are: minimum film thickness 'h_{min}', its percentage difference from the maximum grid size, friction force 'F', and maximum pressure 'p_{max}'.

4.3.2 Study of lubricant bulk modulus

As described in section 3.3, the Elrod-Adams mass conservation model makes use of the bulk modulus, which introduces compressibility to the fluid and expresses the relation between the variation of lubricant pressure and density. However, after discussions with Professor M. Fillon, it was ascertained that bulk modulus does not necessarily correspond to a physical parameter of the lubricant. The selected bulk modulus should be the minimum value, above which the computed pressure differences are negligible. In addition to this, it was noted that high values of bulk modulus cause numerical instabilities and oscillations. The bulk modulus value that was selected for the present study is equal to 10^9 Pa , for which the calculated maximum pressure for the reference engine load is different by only 0.22% from the corresponding maximum pressure in the case of a bulk modulus value equal to $9 \cdot 10^9$ Pa. In Fig. 48 and Fig. 49 a detailed view of the peak of the pressure distribution against different values of bulk modulus is shown, along with the minimum film thickness for two engine cycles.

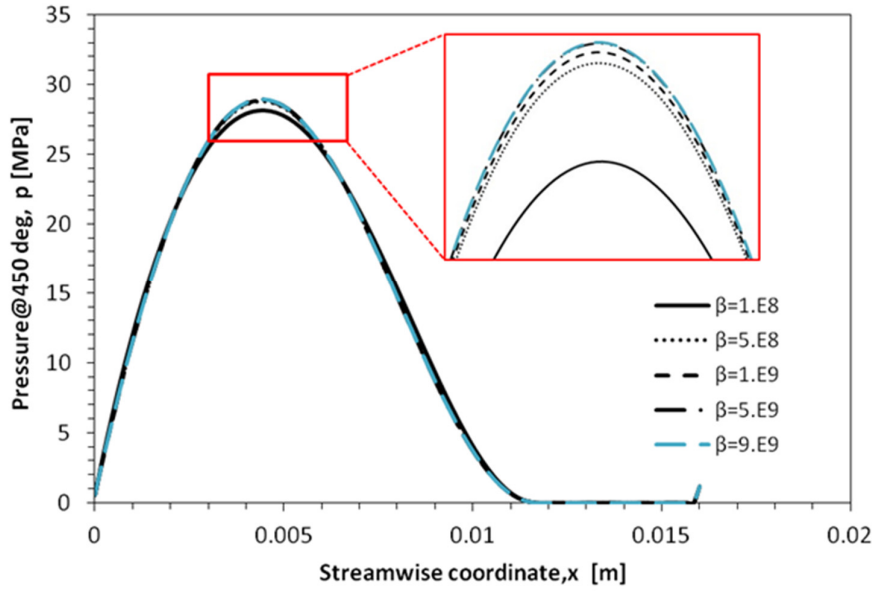

Fig. 48. Pressure distribution at CA=450º, for different values of bulk modulus, 'β'.

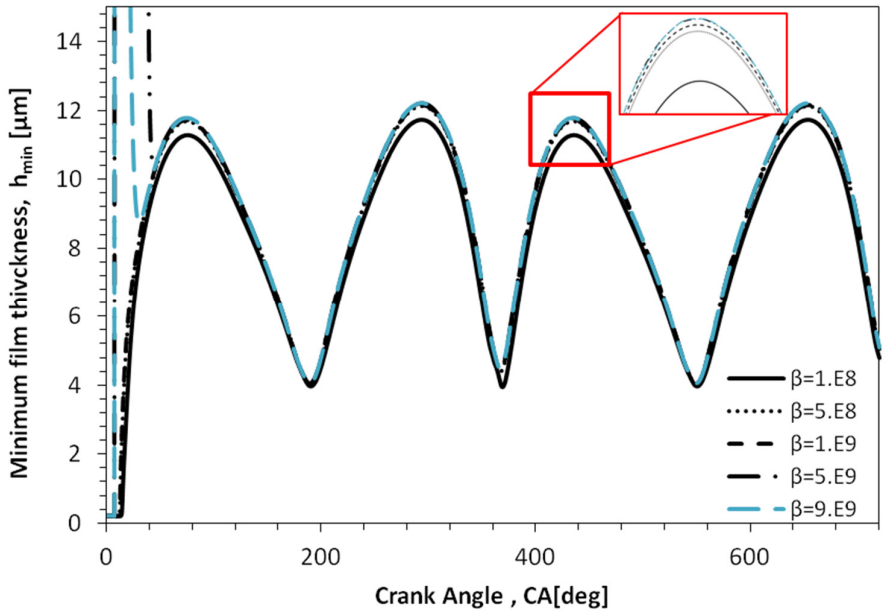

Fig. 49. Minimum film thickness 'h_{min}' versus crank angle for different values of bulk modulus, 'β'.

4.3.3 Comparison of computation with the classic Reynolds equation and the Reynolds equation with the Elrod-Adams mass conservation model

In this section, the performance of the reference piston ring is computed by means of the two solution algorithms, namely (a) by solution of the Reynolds equation with Reynolds boundary conditions, and (b) by solution of the Reynolds equation with the Elrod-Adams mass conservation model. As mentioned in Section 3.2, the Elrod-Adams model can predict the cavitation and reformation boundaries of the fluid more precisely than the simple Reynolds model.

In Fig. 50 several ring operational parameters (minimum film thickness, friction force, maximum pressure and cavitation area) are plotted against crank angle, for the two different solution algorithms. From Fig. 50 it is observed that the differences of minimum film thickness, power loss and maximum pressure are very small, regardless of the solution algorithm used. The only notable difference is that of the extent of the cavitation area, which is underestimated when the Reynolds boundary condition is utilized.

In Fig. 51 two examples of pressure distribution at two different crank angles are presented. Fig. 51 clarifies the difference between the way the two methods handle the reformation boundary at the fluid outflow. When the Reynolds boundary condition is utilized, pressure starts to build up gradually almost before the outlet, while the Elrod model defines that the pressure is regained almost instantly when the fluid meets the ambient pressure.

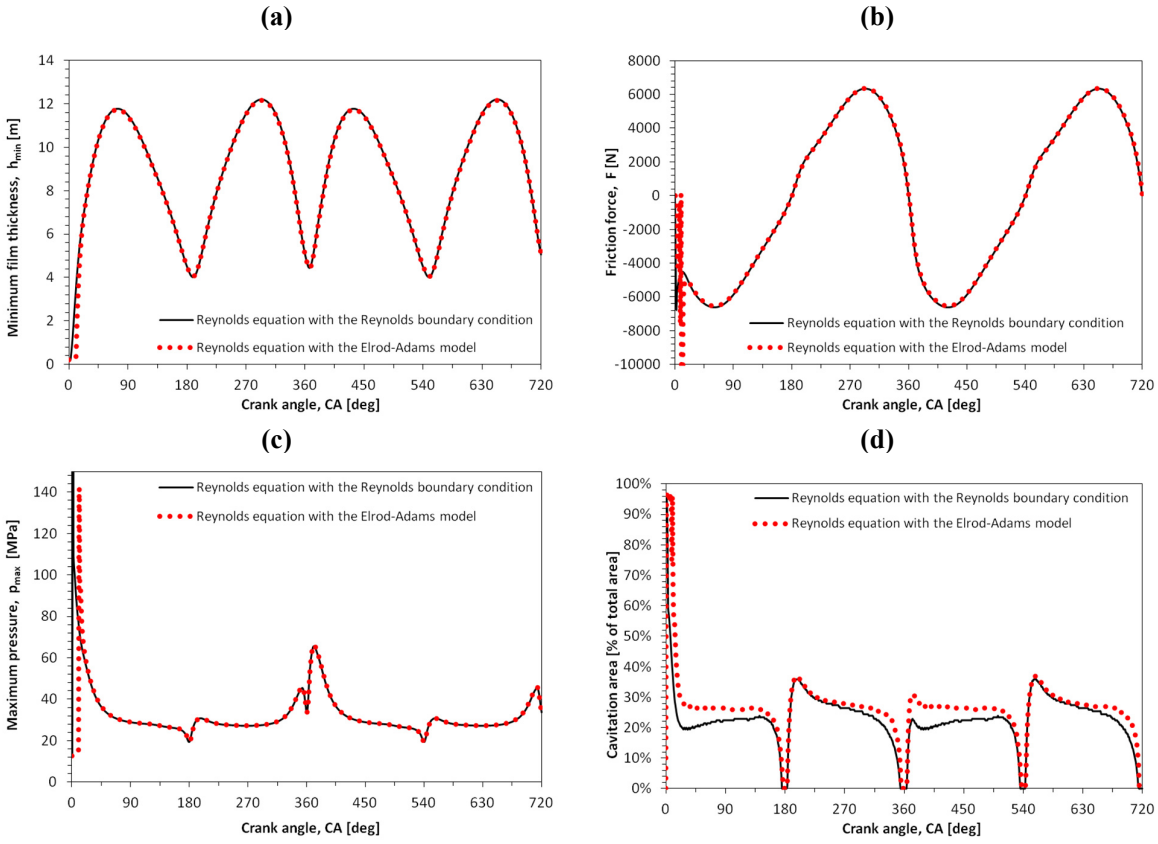

Fig. 50. (a) Minimum film thickness, (b) power loss, (c) maximum pressure and (d) percentage of cavitation area, against crank angle, for the two different solution algorithms.

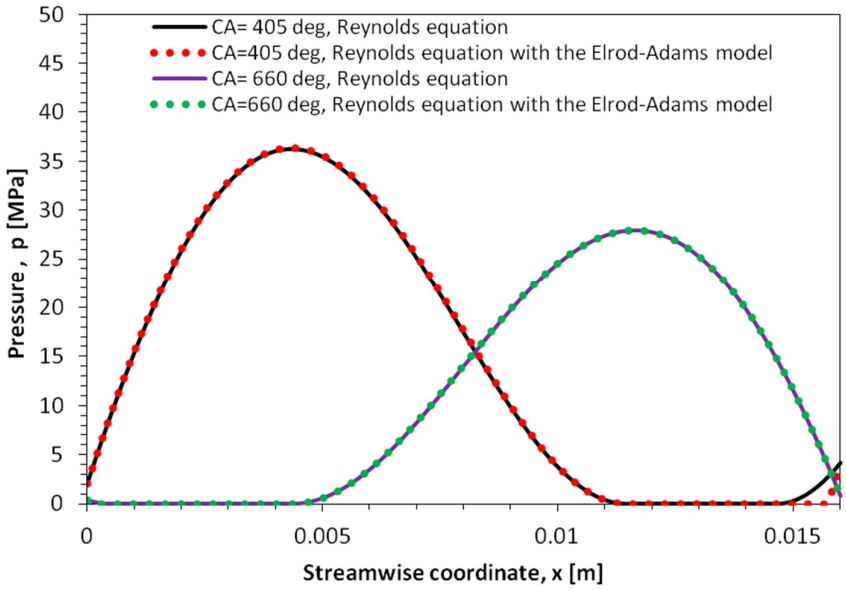

Fig. 51. Pressure distribution for CA=405º (downstroke) and CA=660º (upstroke): Calculations with the classic Reynolds equation and the Elrod-Adams mass conservation model.

4.3.4 Effect of time derivatives (squeeze film terms)

While most publications utilizing the Elrod -Adams mass conservation model solve the steady state problem, in the present work the full transient problem was solved. The main difference between the two approaches, is the inclusion in the latter of the squeeze film term, which is equal to the time derivative of film thickness.

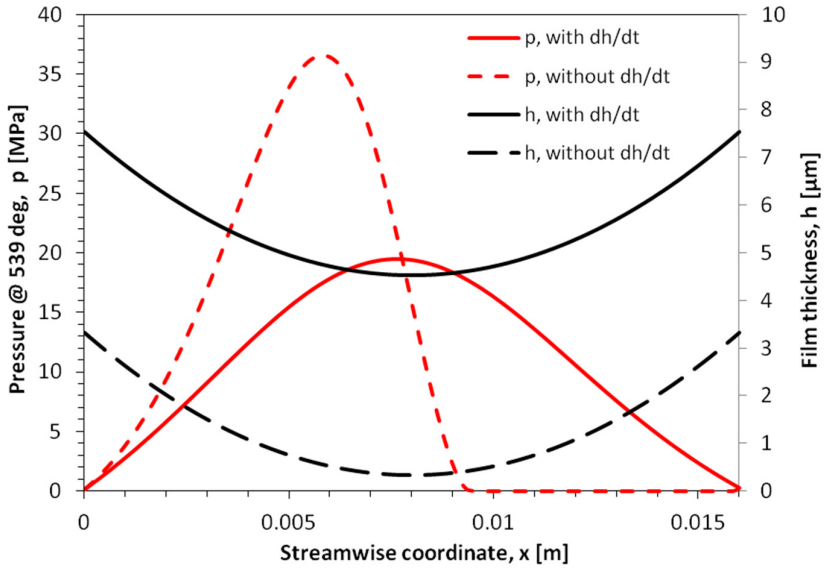

Fig. 52. Pressure and film thickness distribution at CA=539º (approximately zero sliding velocity). Effect of the squeeze film term on the solution.

In Fig. 52 the pressure and film thickness distributions are presented at a representative crank angle (CA=539^{o}). The crank angle of 539 degrees has been selected, because the piston speed is almost equal to zero and the piston is located very close to the BDC. When the speed is equal to zero, no pressure field can be produced from the phenomenon of hydrodynamic lubrication, because there is no sliding motion. Observing Fig. 52, when the time derivatives are excluded, the piston ring is practically in contact with the liner (film thickness is almost equal to the composite roughness r). In addition to this, the pressure distribution is very steep (red dotted line of Fig. 52), because of the generated steep hydrodynamic wedge, which also leads to a large cavitation region, being almost 50% of the total piston ring area.

On the other hand, when time derivatives are taken into consideration, due to the squeeze film term dh/dt, pressure field is developed (red continuous line of Fig. 52) capable of separating the two surfaces with a thicker film, eliminating the possibility of metal to metal contact and wear.

4.3.5 Comparison of different engine cycles

In the present study, simulations of the piston ring under transient conditions are performed. For engine operation at the given operating points, the combustion chamber pressure, and the pressure of the area between the first and the second ring, differ throughout the engine cycle. As shown in the previous section, the Reynolds equation includes time derivative terms (squeeze film terms) which, at the beginning of the simulation, are equal to zero. Therefore, the first simulation cycle is not accurately predicted. After a few cycles, the simulation results between two consecutive cycles are identical. In this section, calculations of the piston ring operational indices are performed for the reference piston ring design, for four full engine cycles.

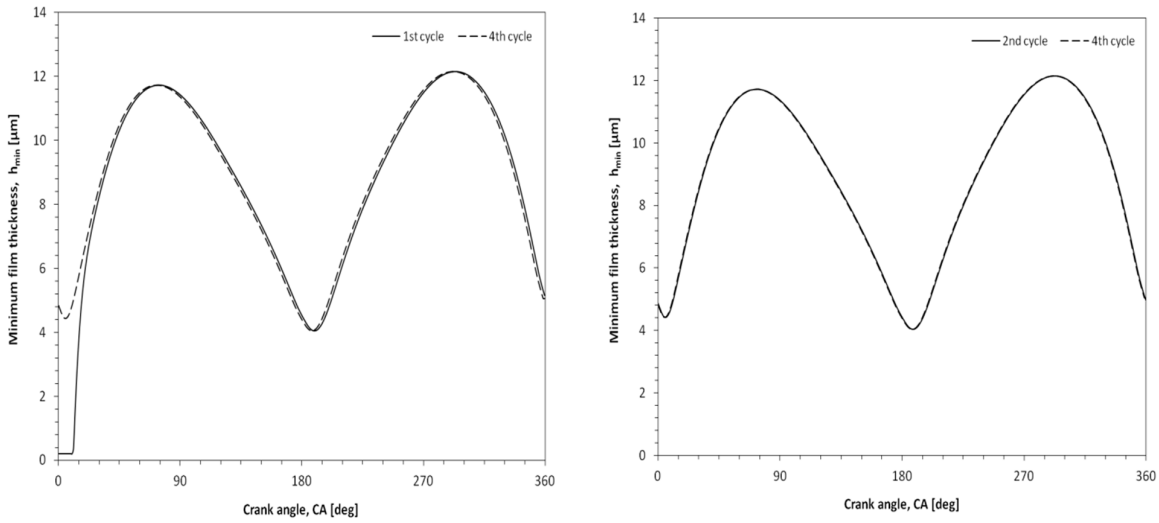

Fig. 53. Minimum film thickness versus crank angle: Comparison between simulation results corresponding to the first and the fourth engine cycle, and simulation results corresponding to the second and fourth engine cycle.

From Fig. 53 it can be concluded that only the first cycle has small deviation compared to the fourth and this deviation lies in the engine start (0^o crank angle), where the film thickness is equal to the composite roughness. At this point piston speed is almost zero and under these circumstances hydrodynamic lubrication cannot occur. In addition to this, there is no squeeze film motion, because the simulation has just started and time derivatives are equal to zero. Therefore, the simulations in the present work are performed for two engine cycles, and the presented results correspond to the second simulation engine cycle.

4.3.6 Reference piston ring design - 100% engine load

After adjusting all the essential parameters, the next step is to calculate the piston ring performance for the two different engine loading conditions (100% and 25% of the engine MCR). Here, the solution algorithm that solves the Reynolds equation with the Elrod-Adams mass conservation model is utilized. In Fig. 54, certain operational parameters of the piston ring are plotted versus crank angle, for a full engine cycle corresponding to the 100% engine loading condition at a rotational speed of 105 RPM. Minimum film thickness ranges from 5 μm το 12 μm approximately, and the maximum pressure acting on the back surface of the piston ring surface is observed at 11.5 degrees of crank angle, where the combustion phenomenon is intense. Friction force and friction coefficient exhibit their maximum values at values of CA equal to 64.6^o and 229.9^o, where the piston speed is maximum, and their minimum values at CA=0^o and CA=179.8^o, where the piston speed is zero.

In Fig. 55, film thickness, h, pressure distribution, p, and film fraction, θ, are plotted versus the streamwise coordinate at several representative crank angle values.

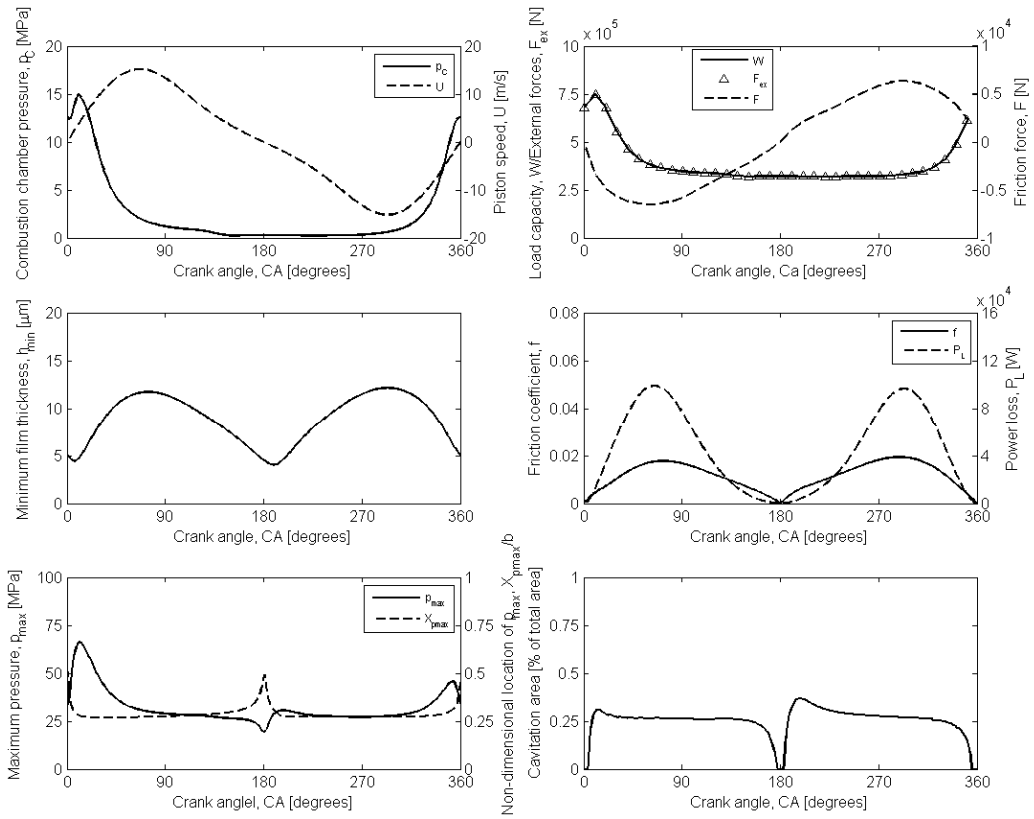

Fig. 54. Reference piston ring design, 100% engine load, 105 RPM: Operational indices versus engine crank angle.

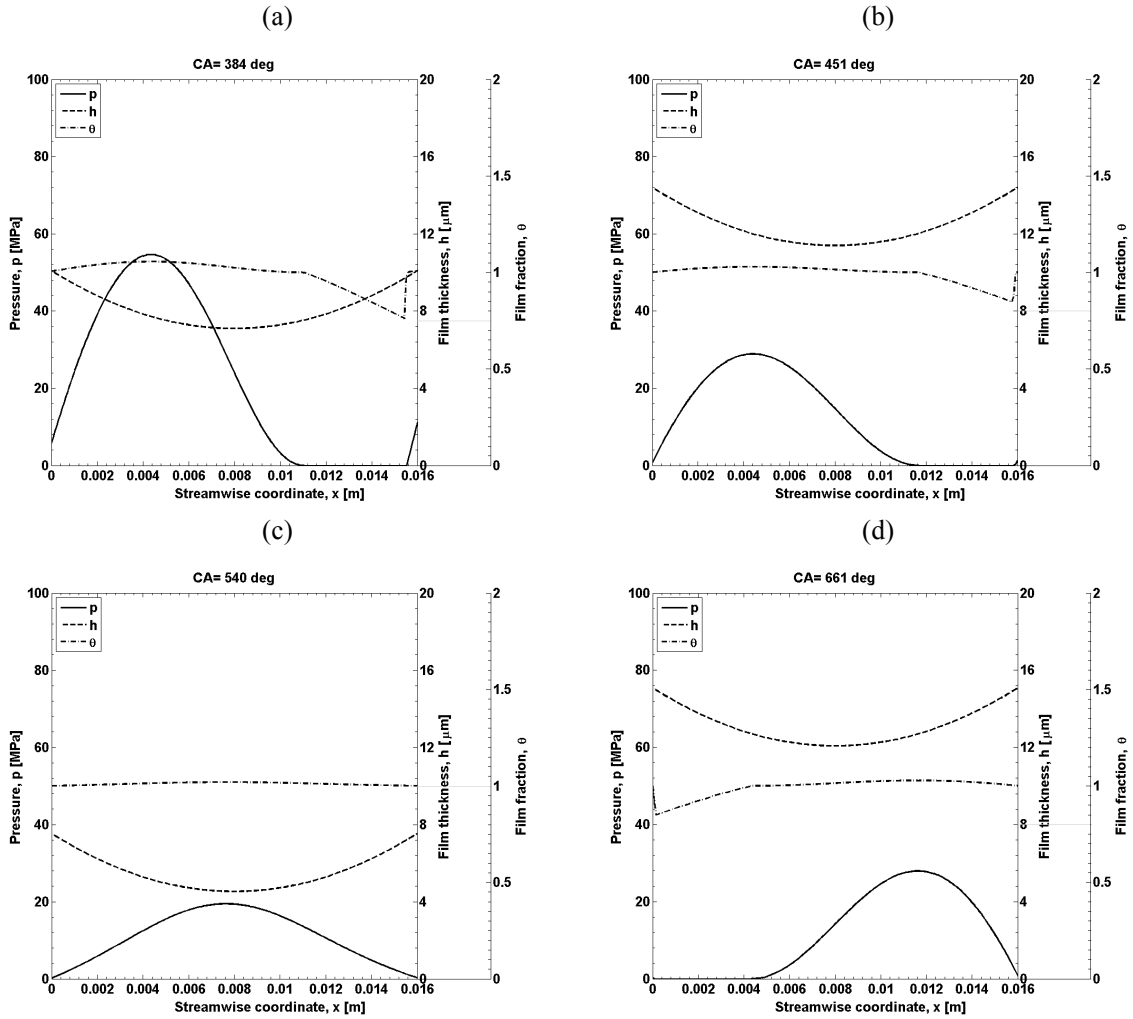

Fig. 55. Reference piston ring design, 100% engine load, 105 RPM: Distributions of pressure 'p', film thickness 'h' and film fraction 'θ' for crank angle values: (a) CA=384º, (b) CA=451º, (c) CA=540º, (d) CA=661º.

4.3.7 Reference piston ring design - 25% engine load

In the present section, the performance of the reference piston ring design is calculated for an engine load of 25% at a rotational speed of 66.1 RPM, using the Reynolds equation with the Elrod-Adams mass conservation algorithm. In Fig. 56, certain operational parameters of the piston ring are plotted versus crank angle, for a full engine cycle. Minimum film thickness ranges from 5 μm το 10 μm approximately and the maximum pressure acting on the piston ring surface is observed at 10.5 degrees of crank angle, where the combustion phenomenon is intense. Friction force, and friction coefficient exhibit a maximum at 65.6º and 292.9º of crank angle, where the piston speed is also maximum, and a minimum at CA=0º and CA=360º, where the piston speed is zero.

In Fig. 57, film thickness, h, pressure, p, and film fraction, θ, are plotted versus the streamwise coordinate, at several representative crank angle values.

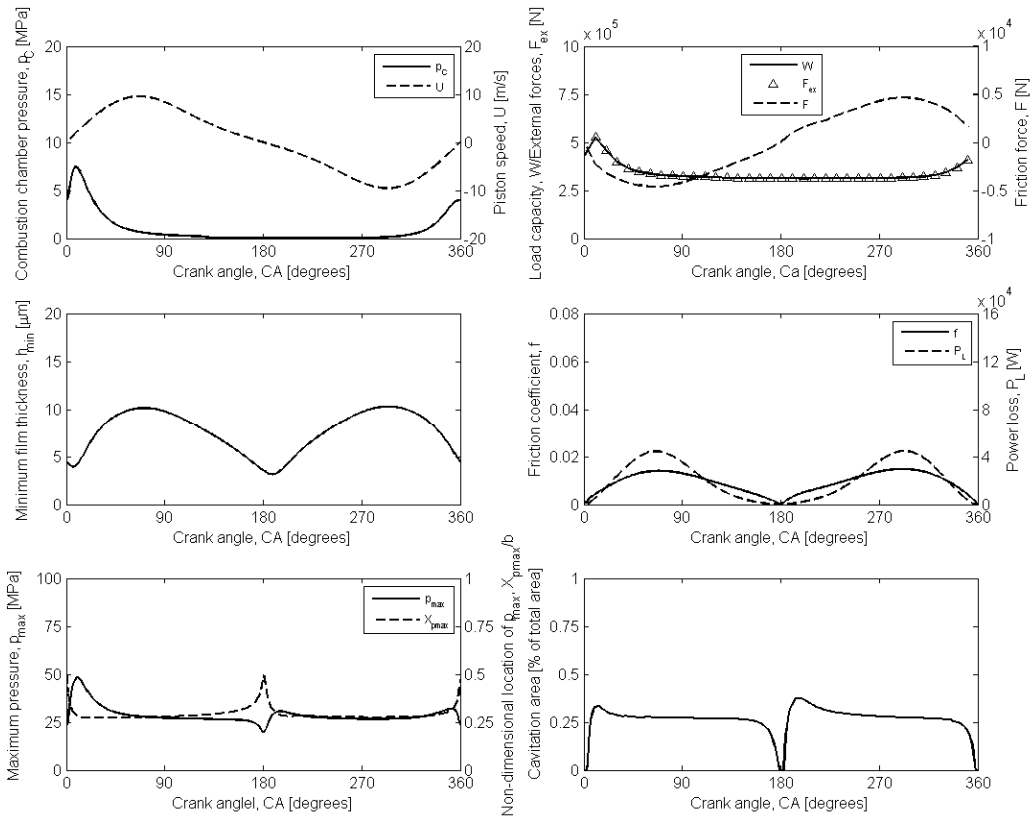

Fig. 56. Reference piston ring design, 25% engine load, 66.1 RPM: Operational indices versus engine crank angle.

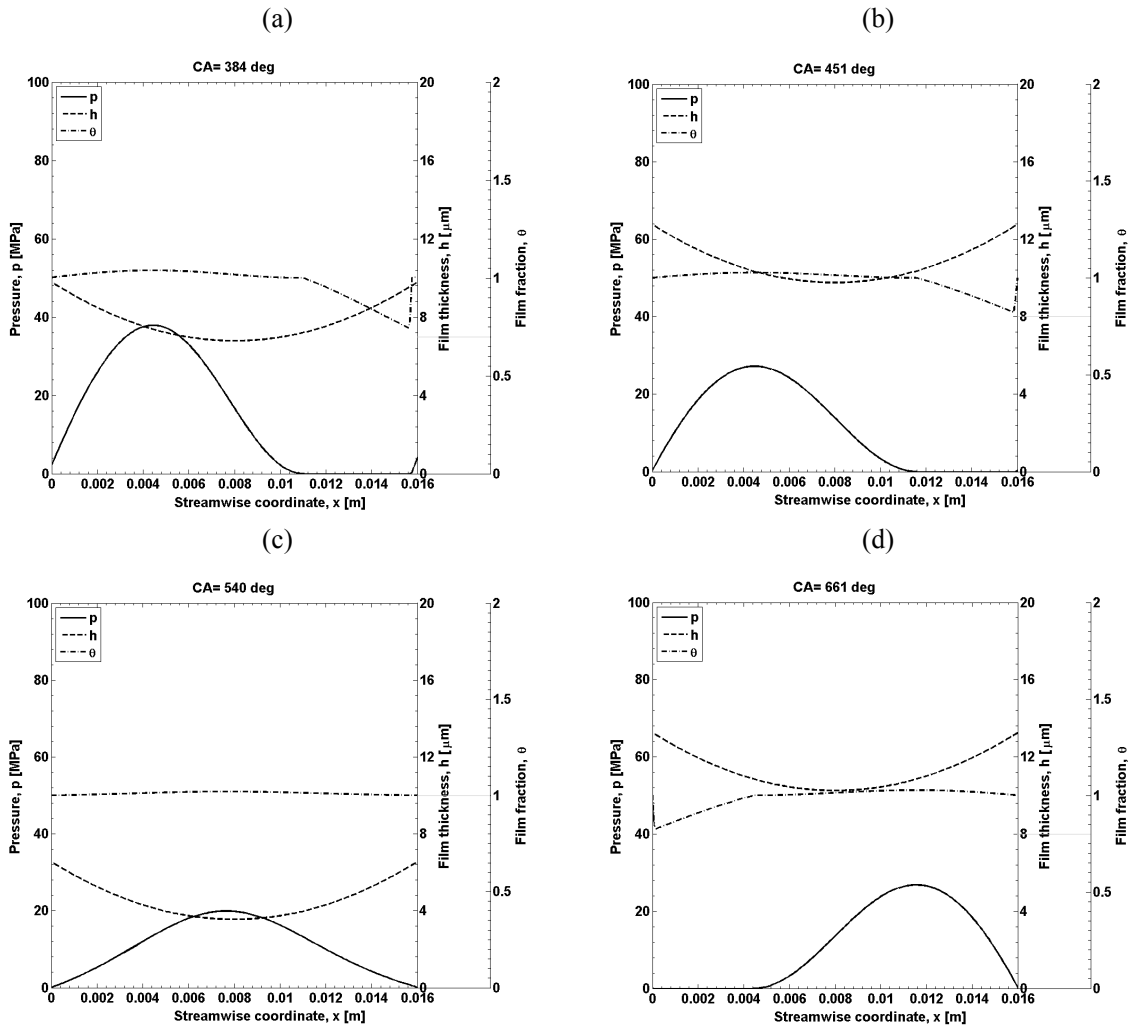

Fig. 57. Reference piston ring design, 25% engine load, 66.1 RPM: Distributions of pressure 'p', film thickness 'h' and film fraction 'θ' for crank angle values: (a) CA=384º, (b) CA=451º, (c) CA=540º, (d) CA=661º

4.4 Parametric analysis of geometric and operational parameters

In this section, a parametric analysis is conducted to identify the effect of different design and operational parameters of the piston ring on its tribological performance.

The parameters studied here are:

- Crown height 'c'
- Offset 'o'
- Pretension force 'T'
- Lubricant dynamic viscosity 'η'
- Composite roughness of the piston ring surface 'r'
- Pressure between the first and second ring '$p_{1\text{-}2}$'

A sketch of the piston ring geometry considered in this section has been presented in Fig. 41.

4.4.1 Crown height

The crown height of the piston ring controls the curvature of the ring surface, so it has an apparent effect on the film shape. The crown height of the reference piston ring is assumed equal to 3 μm; in the present section, crown height values of 1, 2, 5, 8, 12 and 20 μm are also considered.

In Fig. 58, the effect of different crown height values on the operational indices of the piston ring (minimum film thickness, power loss, maximum pressure and percentage of cavitation area) is presented.

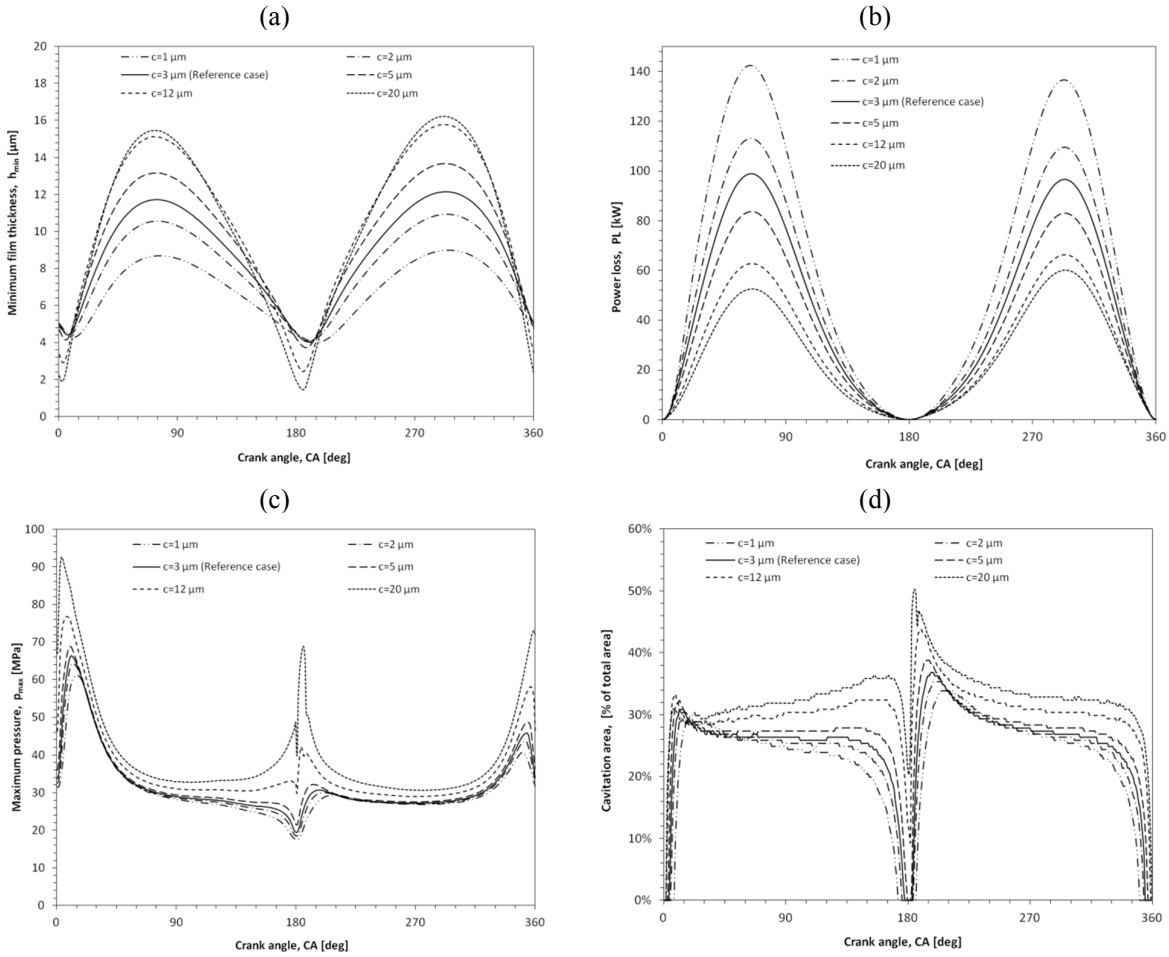

Fig. 58. (a) Minimum film thickness, (b) power loss, (c) maximum pressure and (d) percentage of cavitation area, against crank angle, for different crown height values.

Higher values of crown height lead to increased minimum film thickness and decreased power loss at regions of high piston velocity. However, at regions of low piston velocity (near the TDC and BDC), minimum film thickness is decreased, in comparison to the reference design, increasing the likelihood of asperity contact between the ring and the liner wall. Further, values of crown height higher than 12 μm will provide negligible additional

benefit. Maximum pressure follows the trend of minimum film thickness, whereas the cavitation area increases with increasing crown height, due to the resulting sharper diverging region geometry.

4.4.2 Offset

The ring controls the location of the minimum value of the parabola corresponding to the ring face geometry, see Fig. 41. The reference piston ring has no offset, o=0 mm; in the present section, offset values of 0.8 mm, 1.6 mm, 3.2 mm, -0.8 mm, -1.6 mm, -3.2 mm are considered.

In Fig. 59 and Fig. 60, the effect of different offset values on the operational indices of the piston ring (minimum film thickness, power loss, maximum pressure and percentage of cavitation area) is presented. The cases of positive and negative offset are presented in a different set of graphs, in order to detect the differences.

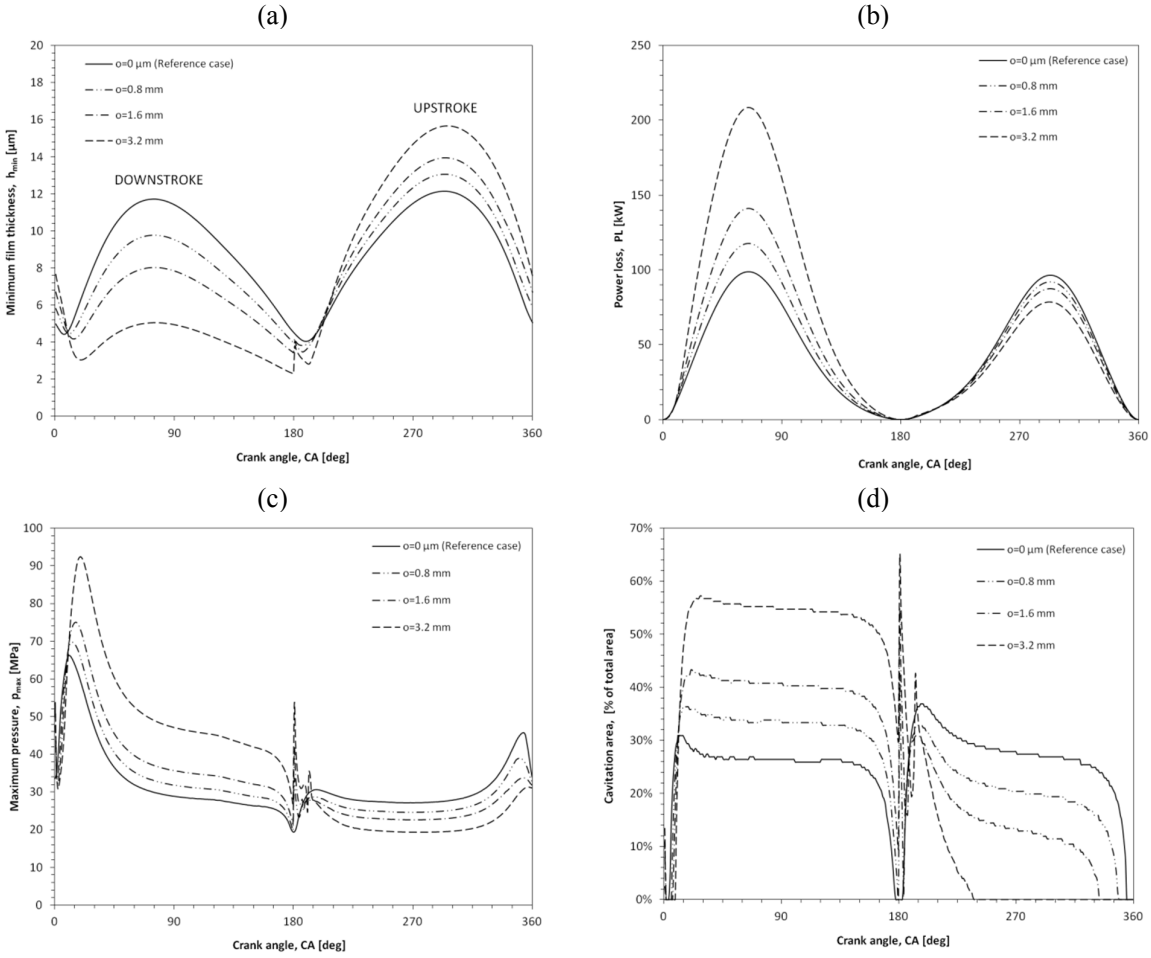

Fig. 59. (a) Minimum film thickness, (b) power loss, (c) maximum pressure and (d) percentage of cavitation area, against crank angle, for different positive offset values.

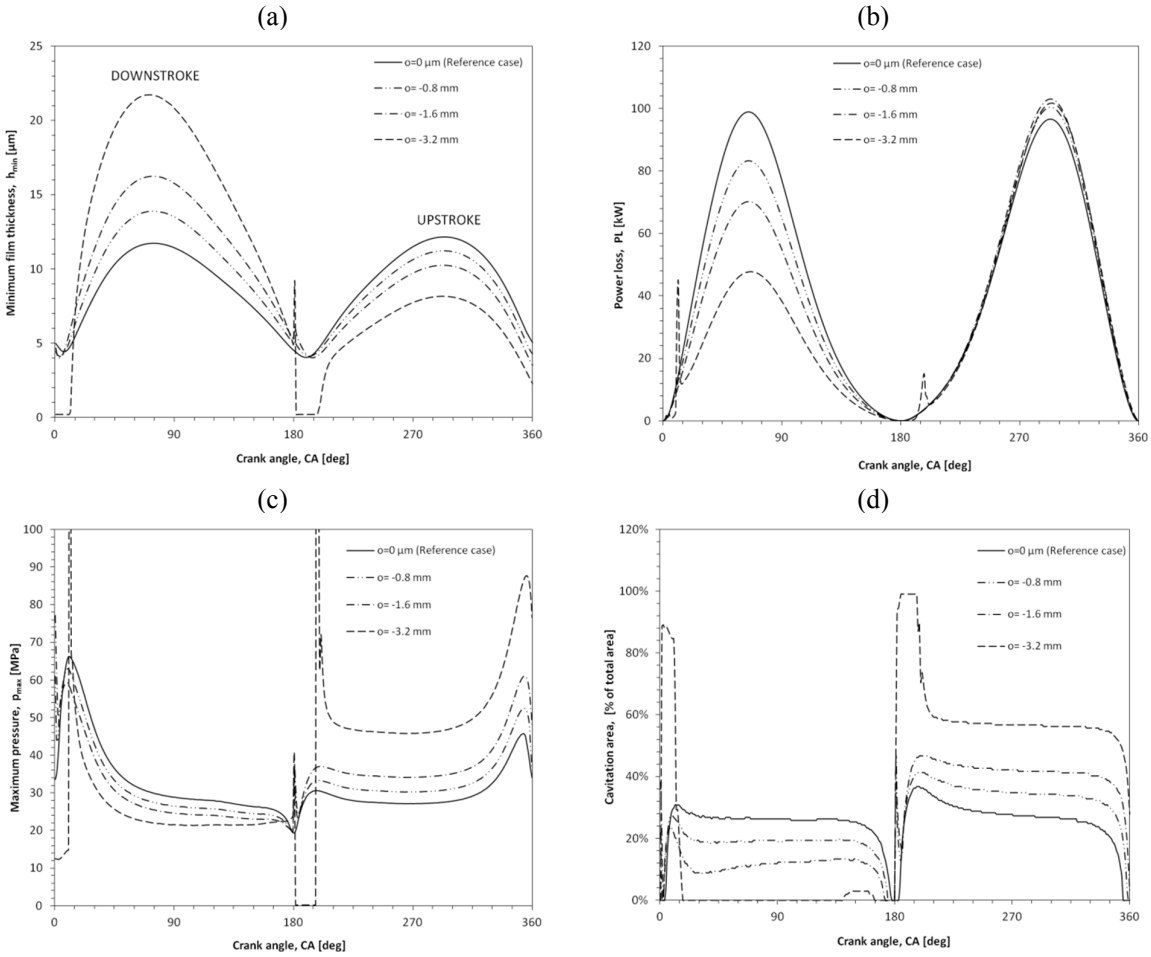

Fig. 60. (a) Minimum film thickness, (b) power loss, (c) maximum pressure and (d) percentage of cavitation area, against crank angle, for different negative offset values.

Based on Fig. 59, we observe that positive values of offset, o, lead to decreased minum film thickness at the first half of the engine cycle (0º-180º of CA), and to increased minimum film thickness at the second half of the engine cycle. At CA values close to 180º, where piston speed is minimum, positive values of offset lead to decreased values of minimum film thickness, which increases the likelihood of asperity contact between the ring and then liner. Power loss increases substantially at the first half of the engine cycle, whereas, at the second half, it exhibits a small decrease, in comparison to the reference case. Maximum pressure, increases substantially at the first half of the cycle, followed by a substantial increase of the cavitating ring area.

On the other hand, negative values of offset, o, lead to increased minimum film thickness at the first half of the engine cycle and to decreased (but in a less pronounced way) minimum film thickness at the second half of the engine cycle. The overall minimum film thickness, remains at the levels of that of the reference case, except for the case of o= -3.2 mm where asperity contact is observed at CA=180º. Power loss exhibits substantial reduction at the first

half of the engine cycle, whereas it is slightly increased at the second half of the engine cycle. For the case of o= -1.6 mm, the overall maximum pressure is less than that of the reference case, whereas the cavitation region is decreased at the first half of the engine cycle and increased at the second. Overall, this value of offset leads to an overall increased minimum film thickness, decreased power losses , without increase of maximum pressure.

4.4.3 Pretension force

In section 4.1, the tangential ring pretension force was calculated for the reference design, following the methodology of [25]. In the present section different values of this parameters are considered in order to study the effect of the ring pretension force on the tribological behavior of the system. The reference pretension force is 49744 N, and the additional values considered here are: 5000 N, 15000 N, 30000 N, 60000 N, 100000 N.

In Fig. 61, the effect of different pretension force values on the operational indices of the piston ring (minimum film thickness, power loss, maximum pressure and percentage of cavitation area) is presented.

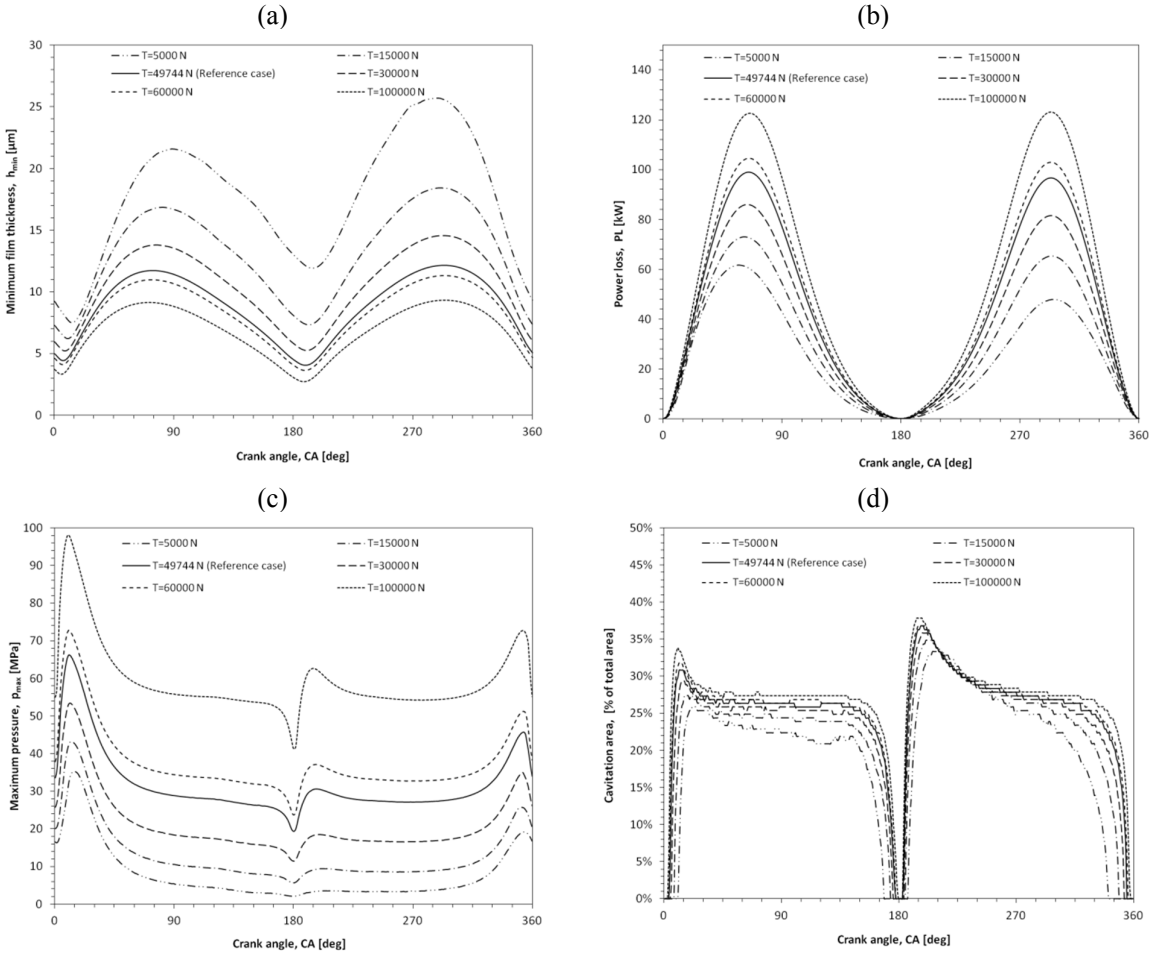

Fig. 61. (a) Minimum film thickness, (b) power loss, (c) maximum pressure and (d) percentage of cavitation area, against crank angle, for different ring pretension force values.

Higher pretension force results in lower minimum film thickness, higher power loss, higher maximum pressure and larger cavitation area. Increasing the ring pretension force, the ring gets closer to the liner wall, proving the above trends.

4.4.4 Viscosity

The lubricant oil selected for the reference case has a viscosity value of 0.19 Pa·s at the reference working temperature. Here, different values of oil viscosity are considered, namely those of 0.03, 0.05, 0.075, 0.12, 0.3 and 0.45 Pa·s. In Fig. 62, the effect of different oil viscosity on the operational indices of the piston ring (minimum film thickness, power loss, maximum pressure, percentage of cavitation area) is presented.

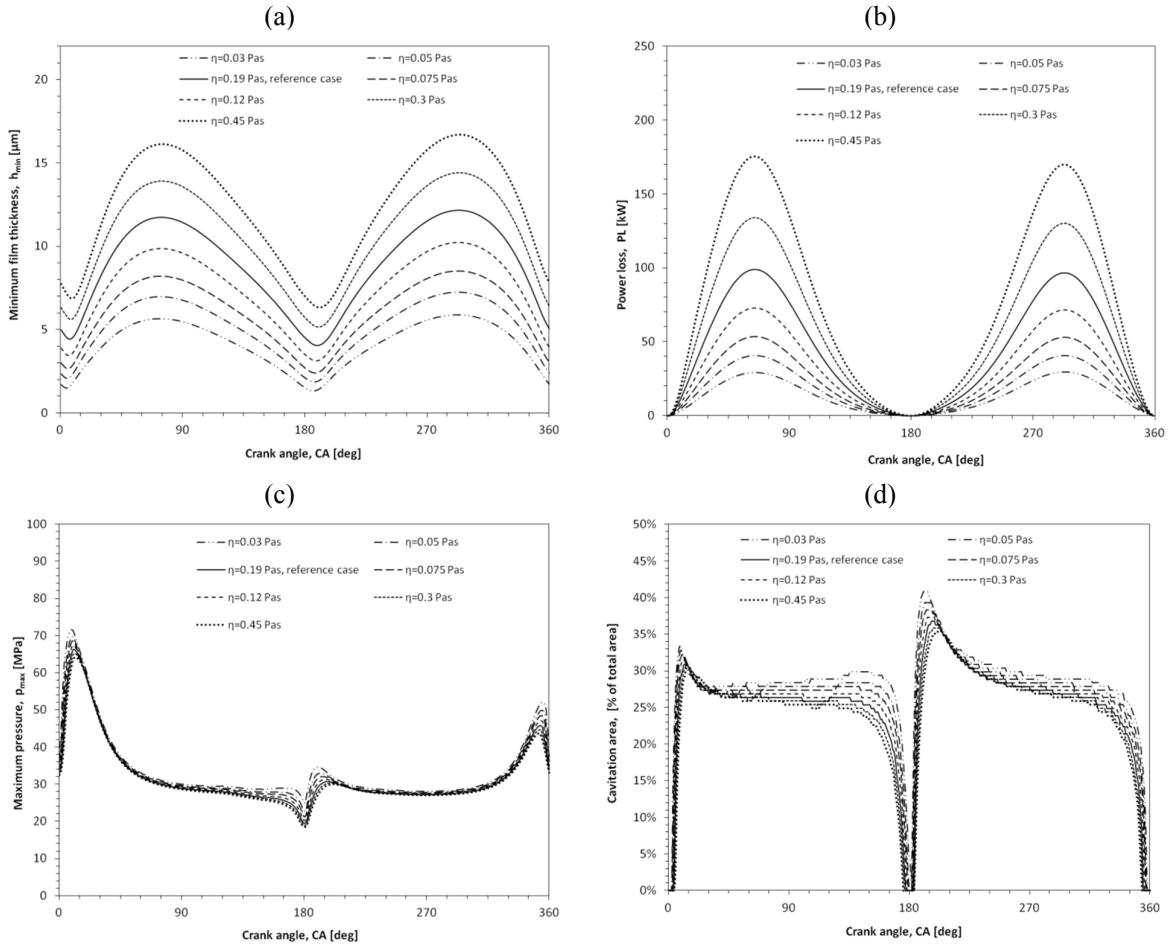

Fig. 62. (a) Minimum film thickness, (b) power loss, (c) maximum pressure and (d) percentage of cavitation area, against crank angle, for different values of viscosity.

As expected, higher values of viscosity create a thicker lubricating film (higher values of minimum film thickness) and exhibit higher values of power loss, because motion of a more viscous fluid yields higher friction drag. The opposite is observed for lower values of

viscosity. The effect of oil viscosity on maximum pressure and on the extent of cavitation region is negligible.

4.4.5 Pressure of area between first and second piston ring

For the calculations of the reference case the pressure after the first compression ring and before the second one ($p_{1\text{-}2}$) has been assumed equal to half of the combustion chamber pressure (p_{ch}), following the work of Jeng et al. [4]. This statement leads to an overestimation of the trailing pressure of the first ring, so in this section additional (lower) values are studied, namely 1/3, 1/5 and 1/10 of the combustion chamber pressure.

In Fig. 63, the effect of different values of pressure $p_{1\text{-}2}$ on the operational indices of the piston ring (minimum film thickness, power loss, maximum pressure and percentage of cavitation area) is presented. p_{ch}

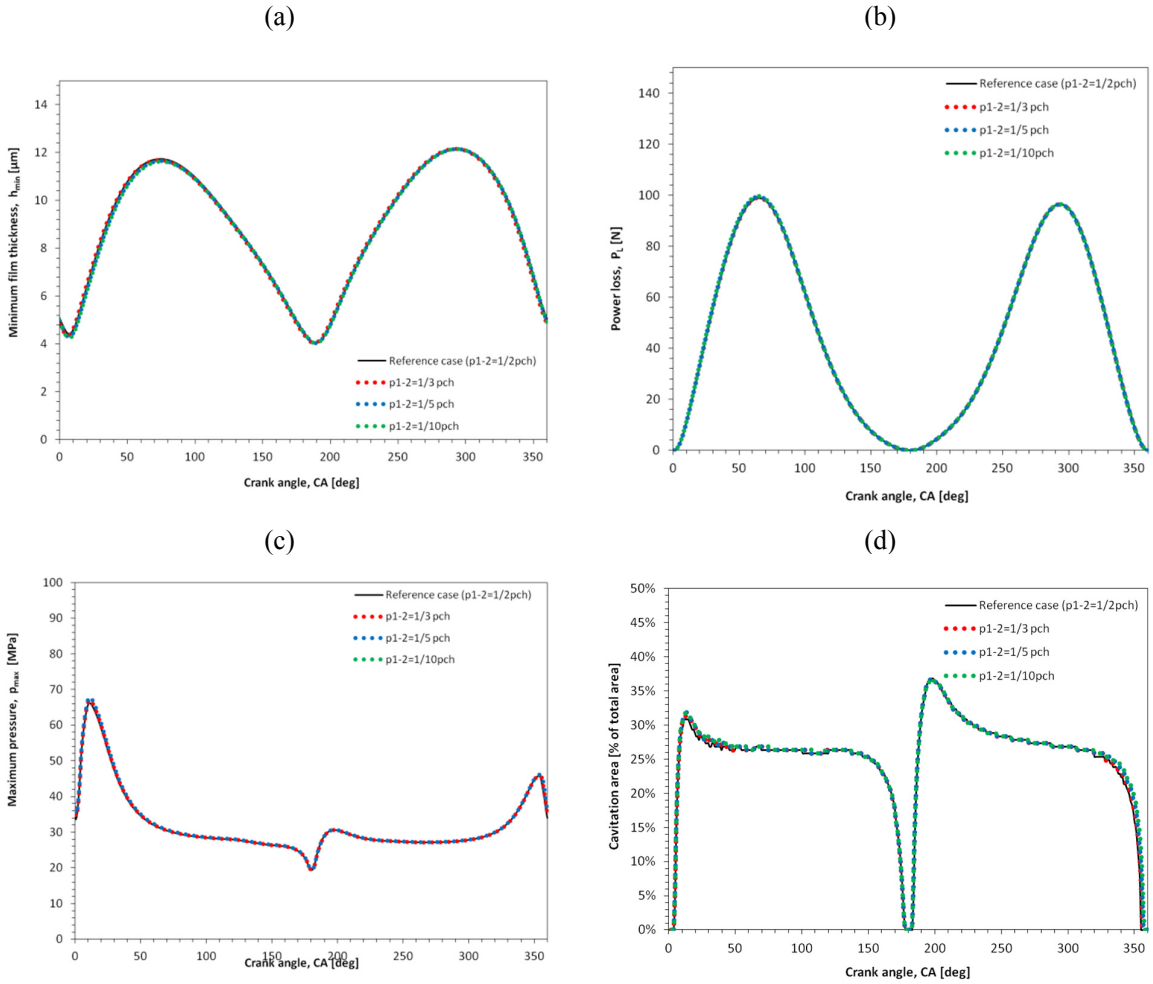

Fig. 63. (a) Minimum film thickness, (b) power loss, (c) maximum pressure and (d) percentage of cavitation area, against crank angle, for different values of pressure between first and second piston ring.

It is obvious from Fig. 63 that different values of the pressure between the first and second piston rings has negligible effect on the tribological behavior of the system. This is rather expected since as shown in Fig. 55, the maximum hydrodynamic pressure is almost two orders of magnitude higher than the pressure at the ring boundaries.

4.4.6 Composite roughness

The composite roughness of the reference piston ring is assumed to be 0.2 μm; in the present section, composite roughness values of 0.1 and 0.5 μm are also considered. In Fig. 64 the operational indices for these different values are plotted.

Composite roughness affects mainly the frequency of asperity contact (large values more frequent contacts and vice versa). As shown in previous sections, for the reference ring design, asperity contact is observed only at the first simulation cycle (where dh/dt=0). At the next engine cycles, the squeeze film effect aids in maintaining a thick lubricating film, even at instances of very low piston speed. Taking that into account, here, only the first cycle of the engine is presented. Different values of composite roughness affect the region of very small crank angle values, where asperity contact is observed. We see that a decrease of composite roughness will decrease the duration of asperity contact, and vice versa.

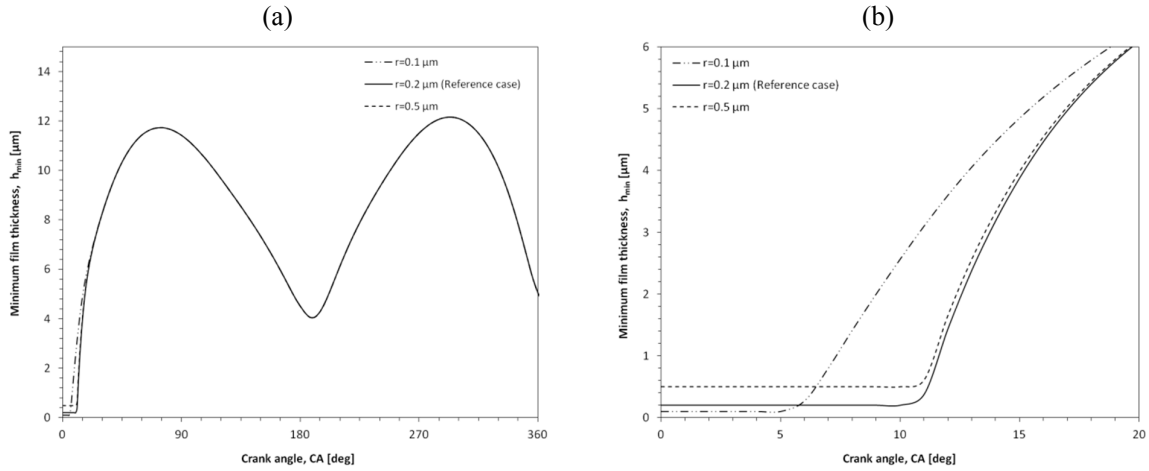

Fig. 64. (a) Minimum film thickness against crank angle, for different values of pressure between first and second piston ring, (b) zoom of 20 first crank angles of engine cycle

4.5 Effect of hydrophobicity at part of the ring surface

In this section, the effect of introducing hydrophobic properties at part of the rig face on the ring performance characteristics is investigated. Here, the Reynolds equation for hydrophobic surfaces with the Elrod-Adams mass conservation model is used, for the two different engine operating conditions considered in the present study. Fig. 65 presents a piston ring with two regions of hydrophobicity, one at the top half of the ring (near the combustion chamber), and one at the bottom half of the ring. The location and extent of those regions are controlled by the following non-dimensional parameters. Here, a slip length value b= 2 μm is assumed, corresponding to a non-dimensional value $b^* = \frac{b_s}{r} = 10$ (r: composite roughness of the ring face, here equal to 0.2 μm).

- b^*: Non-dimensional slip length: $b^*=b_s/r$
- SB_s: Bottom hydrophobic region: Non-dimensional x coordinate of slip start location
- SB_e: Bottom hydrophobic region: Non-dimensional x coordinate of slip end location
- ST_s: Top hydrophobic region: Non-dimensional x coordinate of slip start location
- ST_e: Top hydrophobic region: Non-dimensional x coordinate of slip end location

The initial values of SB_s, SB_e, ST_s, ST_e are given in Table 5.

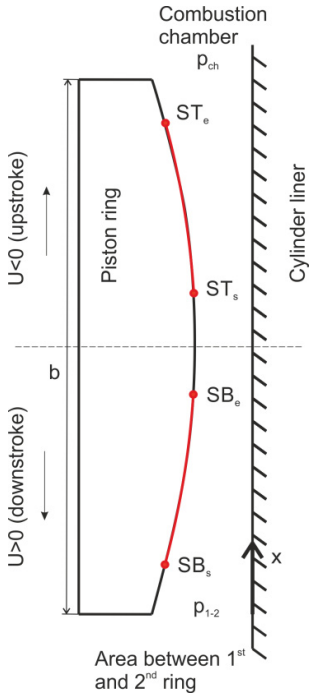

Fig. 65. Piston ring face profile with the regions of hydrophobicity highlighted; the four dots mark the start and end of each hydrophobic area; SB_s: start of bottom slip region, SB_e: end of bottom slip region, ST_s: start of top slip region, ST_e: end of top slip region

SB_s	0.1
SB_e	0.3
ST_s	0.7
ST_e	0.9

Table 5. Piston ring with hydrophobicity. Parameters controlling the location and extent of the hydrophobic regions of Fig. 65.

In Fig. 66 a comparison of the operational indices of the reference piston ring (section 4.3.6) with those of the hydrophobic ring corresponding to the design parameters of Table 5 is performed.

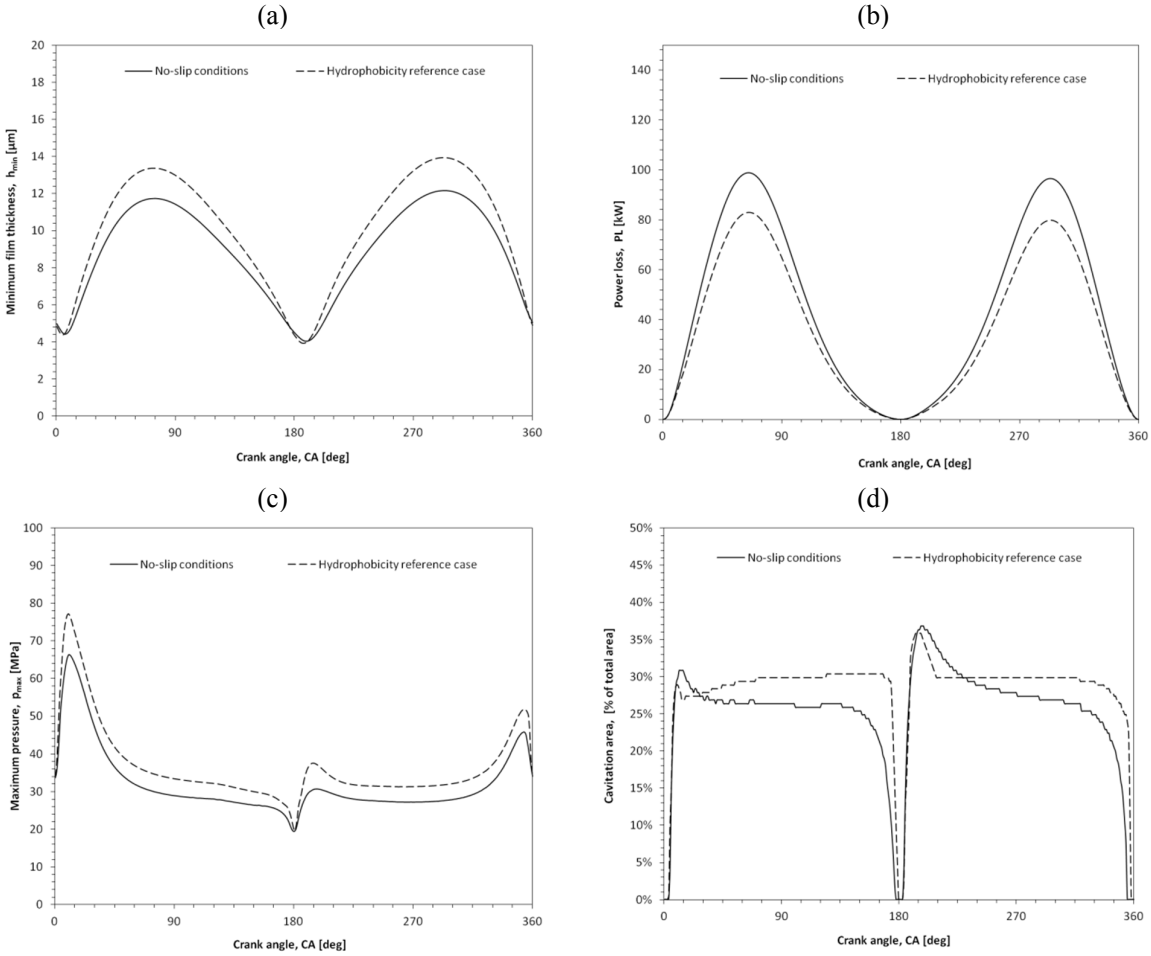

Fig. 66. (a) Minimum film thickness, (b) power loss, (c) maximum pressure and (d) percentage of cavitation area for 100% engine load, against crank angle, for the reference piston ring, and the hydrophobic ring with parameters those of Table 5.

The introduction of hydrophobicity is proved beneficial for the ring. In particular, minimum film thickness is increased, corresponding to higher load capacity, and power loss is substantially decreased, but with the cost of increased maximum pressure at the ring face. Cavitation area is also increased by approximately 5%.

In the following paragraphs, a parametric analysis is performed for different values of b^*, SB_s, SB_e, ST_s and ST_e to identify optimal design of the hydrophobic region.

4.5.1 Non-dimensional slip length, b*

Here values of b^* between 0 and 100 are considered, corresponding to dimensional slip length values of 0 to 20 μm. In Fig. 67, the piston ring operational characteristics are presented versus crank angle, for different values of b^*.

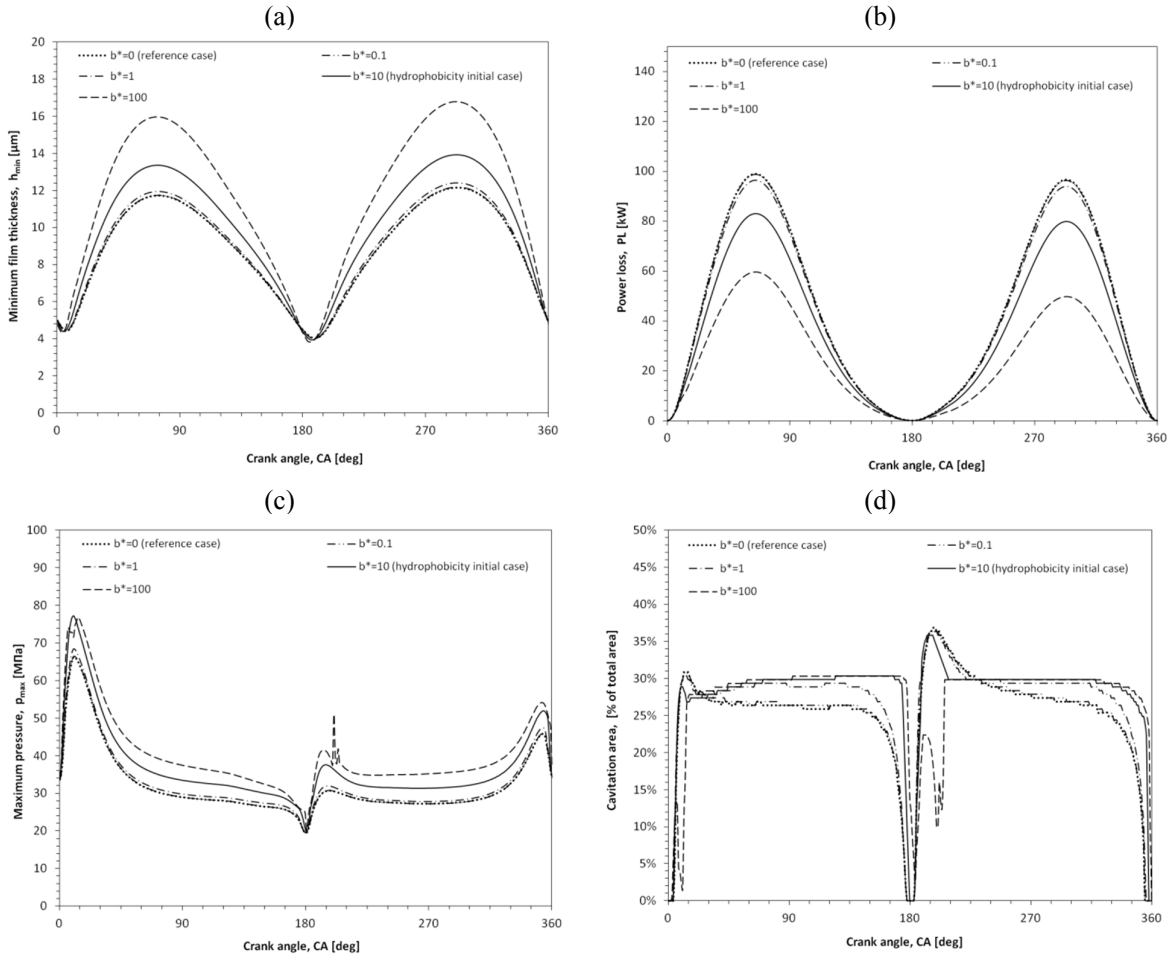

Fig. 67. (a) Minimum film thickness, (b) power loss, (c) maximum pressure and (d) percentage of cavitation area, against crank angle, for different values of non-dimensional slip length, b^*

Higher values of b^* are shown to further improve the tribological behavior of the ring. In particular, for b^*=100, minimum film thickness value is almost 20% higher than that corresponding to the case of b^*=10 and power loss is 25% less. Maximum pressure, on the other hand, exhibits a cycle maximum approximately equal to that corresponding to b^*=10. When b^* is decreased below the reference value (b^*=10), the results tend to those of the reference (non-hydrophobic) piston ring.

4.5.2 Bottom slip region: Variation of slip start location

Here, values of SB_s between 0 and 0.2 are considered (SB_s=0.2 corresponds to a x-coordinate of the start of the bottom slip region equal to 0.2xb, where b is the ring width). In Fig. 68, the piston ring operational characteristics are presented versus crank angle, for different values of SB_s.

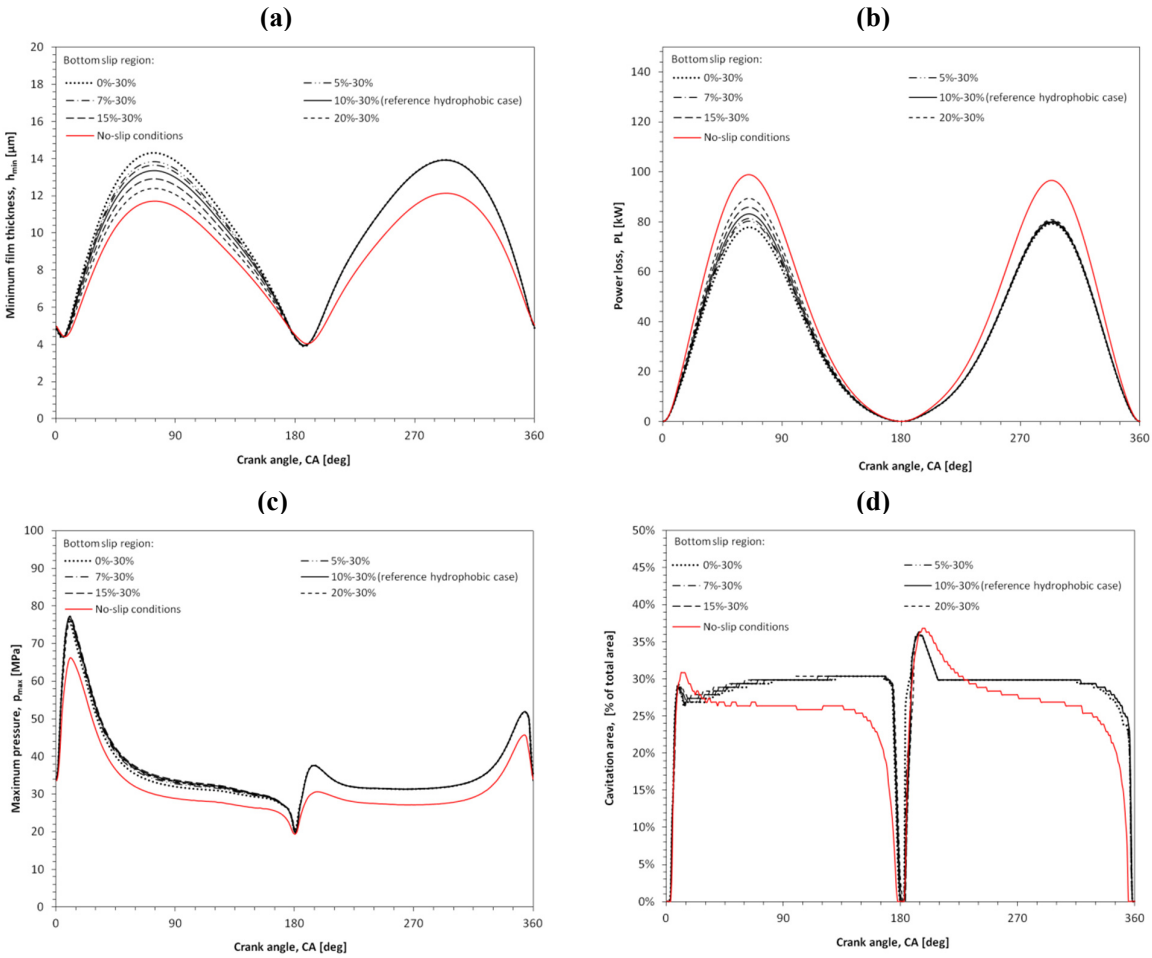

Fig. 68. (a) Minimum film thickness, (b) power loss, (c) maximum pressure and (d) percentage of cavitation area, against crank angle, for different values of start of bottom slip region, SB_s

The results of Fig. 71 suggest that SB_s affects the ring operation only during the downstroke. The largest hydrophobic area (0%-30%) has the best performance, since it further increases the minimum film thickness, decreases power loss, while affecting insignificantly the maximum pressure and the cavitation area.

4.5.3 Bottom slip region: Variation of slip end location

Here, values of SB_e between 0.2 and 0.4 are considered (SB_e=0.4 corresponds to a x-coordinate of the start of the bottom slip region equal to 0.4xb, where b is the ring width). In Fig. 69, the piston ring operational characteristics are presented versus crank angle, for different values of SB_e.

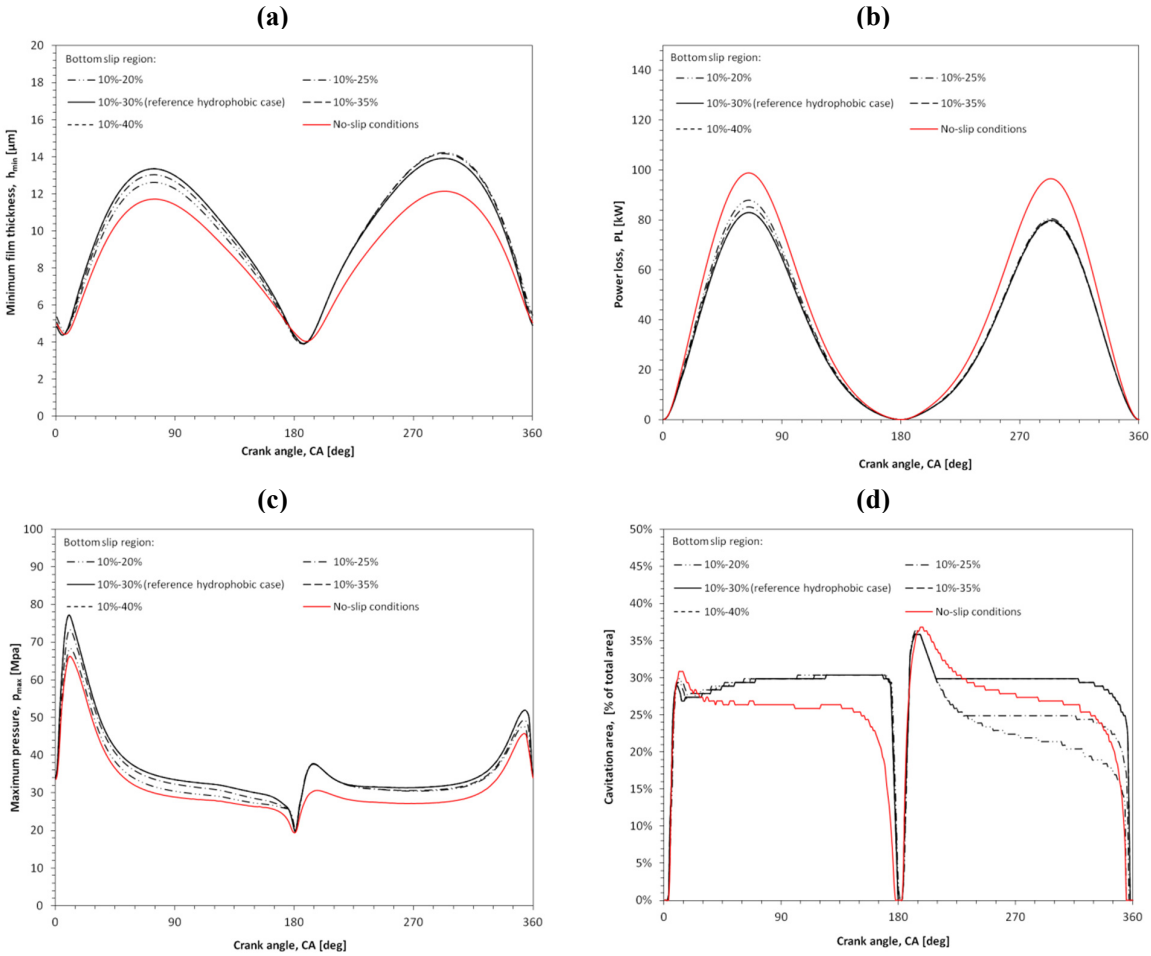

Fig. 69. (a) Minimum film thickness, (b) power loss, (c) maximum pressure and (d) percentage of cavitation area, against crank angle, for different values of the end of bottom slip region, SB_e.

From Fig. 69, it can be concluded that hydrophobic areas larger than the reference one (10%-30%) do not affect at all the operational parameters, whereas smaller areas reduce minimum film thickness and increase power loss.

Merging the observations of Fig. 68 and Fig. 69, the optimum design of the bottom slip region is the one that extends from the start of the piston ring face profile (SB_s=0) until 30% of its total length (SB_e=0.3).

4.5.4 Top slip region: Variation of slip start location

Here, values of ST_s between 0.6 and 0.8 are considered (ST_s=0.6 corresponds to a x-coordinate of the start of the top slip region equal to 0.6xb, where b is the ring width). In Fig. 70, the piston ring operational characteristics are presented versus crank angle, for different values of SB_s.

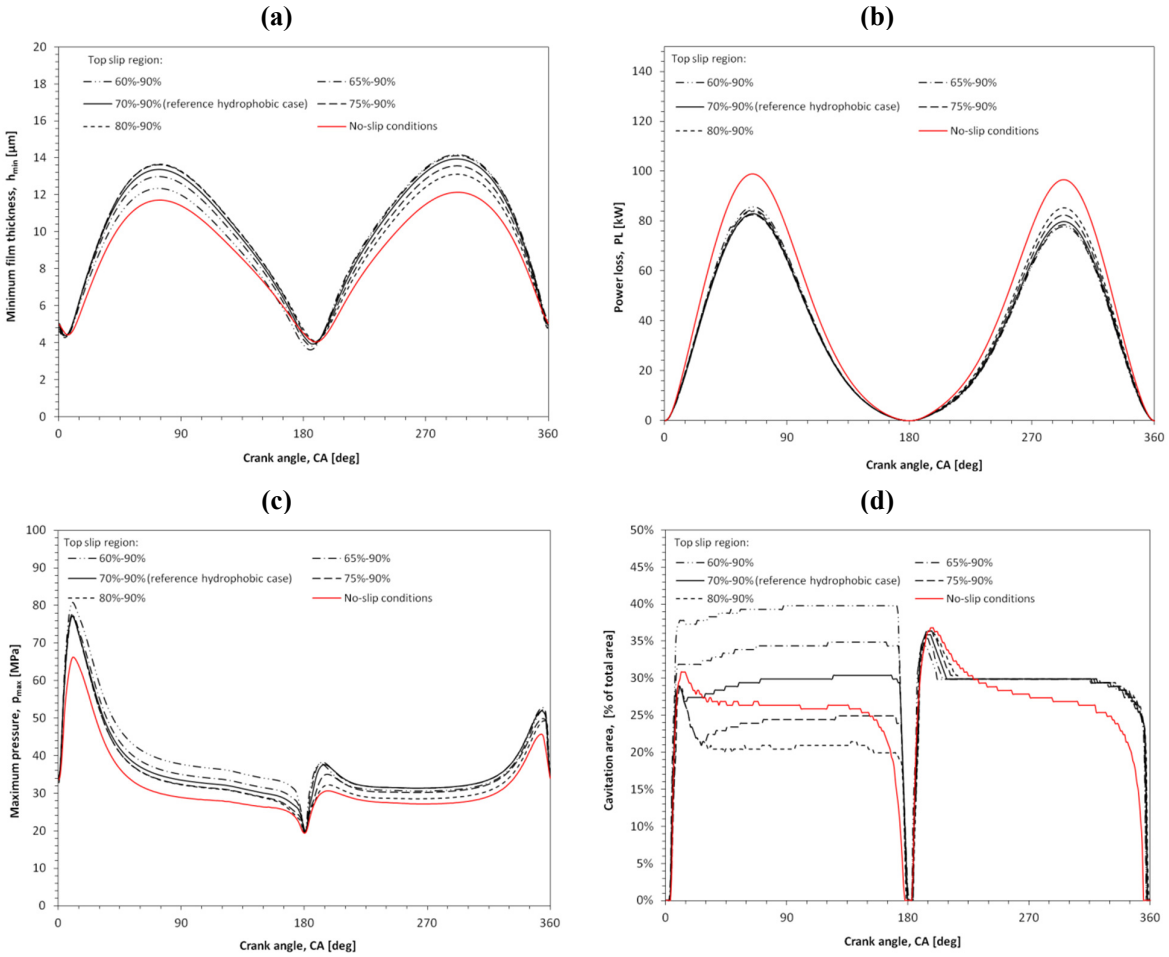

Fig. 70. (a) Minimum film thickness, (b) power loss, (c) maximum pressure and (d) percentage of cavitation area, against crank angle, for different values of the start of top slip region, ST_s.

Lower values of ST_s (top hydrophobic region between 60%-90% and 65%-90%), which are equivalent to larger slip areas, provide a small increase of the minimum film thickness and a small decrease of the power loss in the upstorke motion, while they decrease the former and increase the latter for the downstroke motion. Maximum pressure is decreased for all the cases during the upstroke, while it is slightly increased for increased slip areas during downstroke. Finally, cavitation region is largely increased, by almost 30%, for the cases of large slip areas and is decreased for the smaller ones.

4.5.5 Top slip region: Variation of slip end location

Here, values of ST_e between 0.8 and 1 are considered (ST_s=0.8 corresponds to a x-coordinate of the start of the top slip region equal to 0.8xb, where b is the ring width). In Fig. 71, the piston ring operational characteristics are presented versus crank angle, for different values of SB_e.

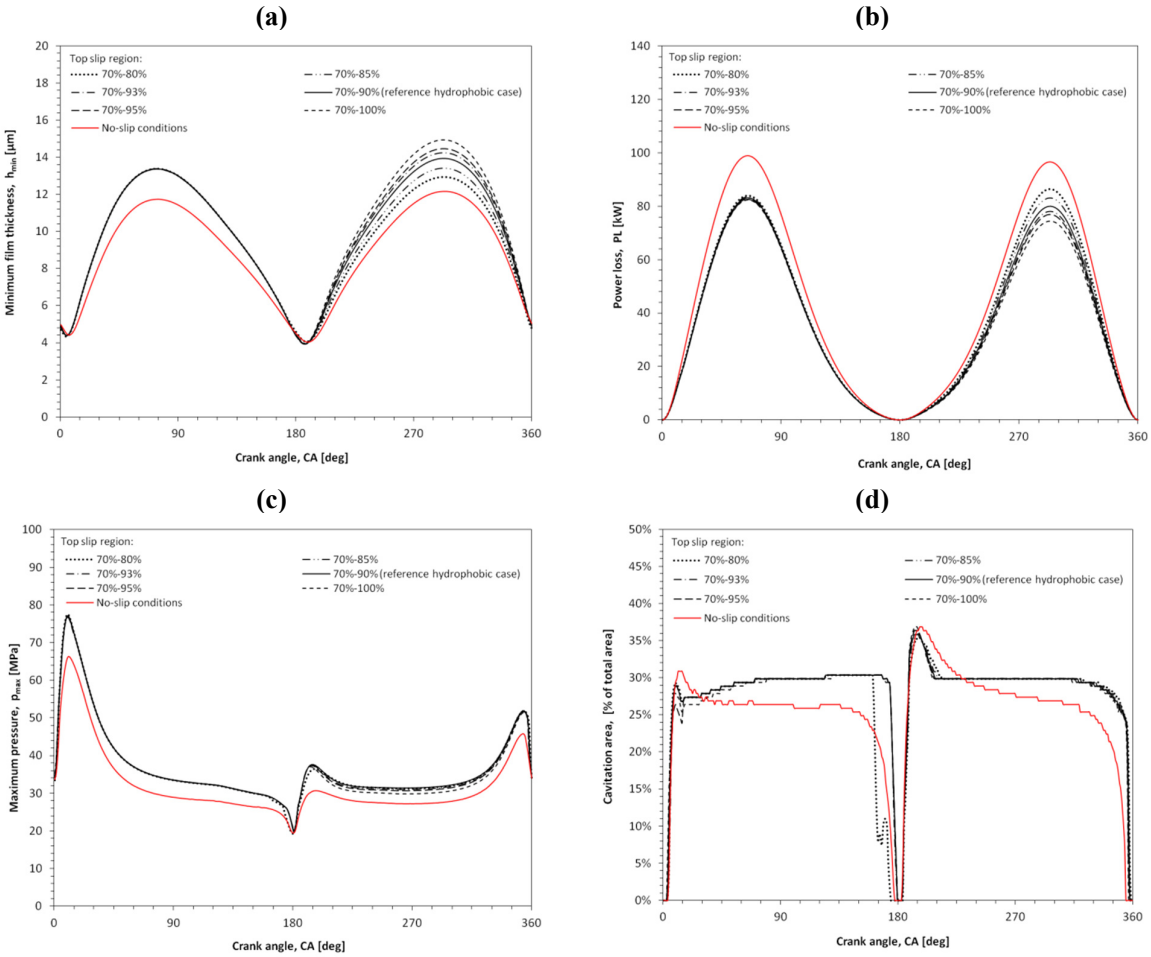

Fig. 71. (a) Minimum film thickness, (b) power loss, (c) maximum pressure and (d) percentage of cavitation area, against crank angle, for different values of end of top slip region, ST_e

Variation of the ST_e affects the ring operation only during the downstroke. According to Fig. 71, the largest hydrophobic area (70%-100%) has the best performance, since it further increases the minimum film thickness, decreases power loss, while affecting insignificantly the maximum pressure and the cavitation area.

4.5.6 Optimal design with hydrophobicity at the bottom and the top part of the piston ring

Summing up the results of the four previous sections (4.5.1-4.5.5), the optimum location of slip regions is from 0% up to 30% and from 70% to 100% of the total piston ring width. In Fig. 72, a comparison is made between the results of the reference no-slip case and of the optimal hydrophobic case. The operational characteristics of this optimum case of hydrophobicity, are presented in Fig. 73, whereas in Fig. 74 pressure distribution and film fraction at several representative crank angles are plotted, in order to further understand this phenomenon.

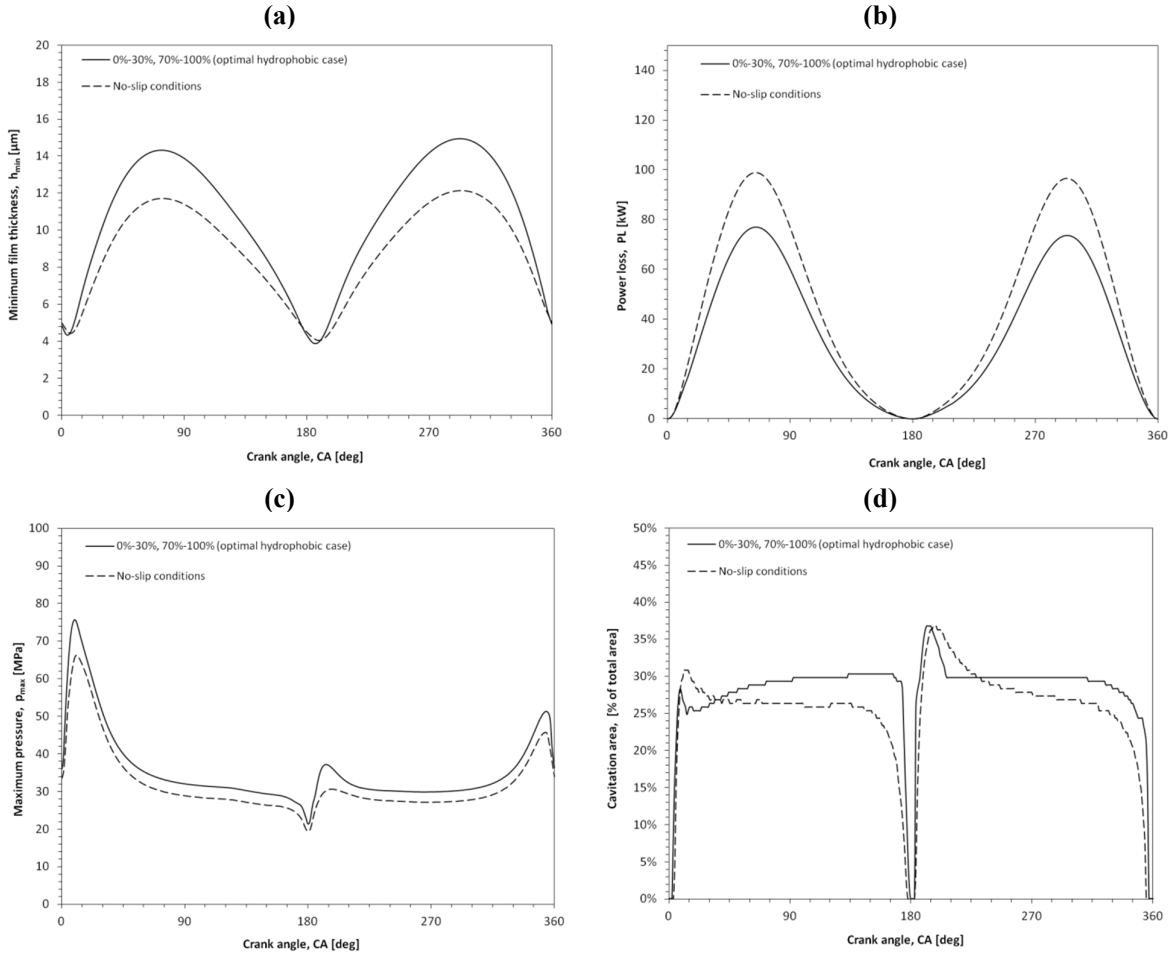

Fig. 72. (a) Minimum film thickness, (b) power loss, (c) maximum pressure and (d) percentage of cavitation area against crank angle, for 100% engine load: Comparison between the reference case (no-slip) piston ring design and the optimal hydrophobic design.

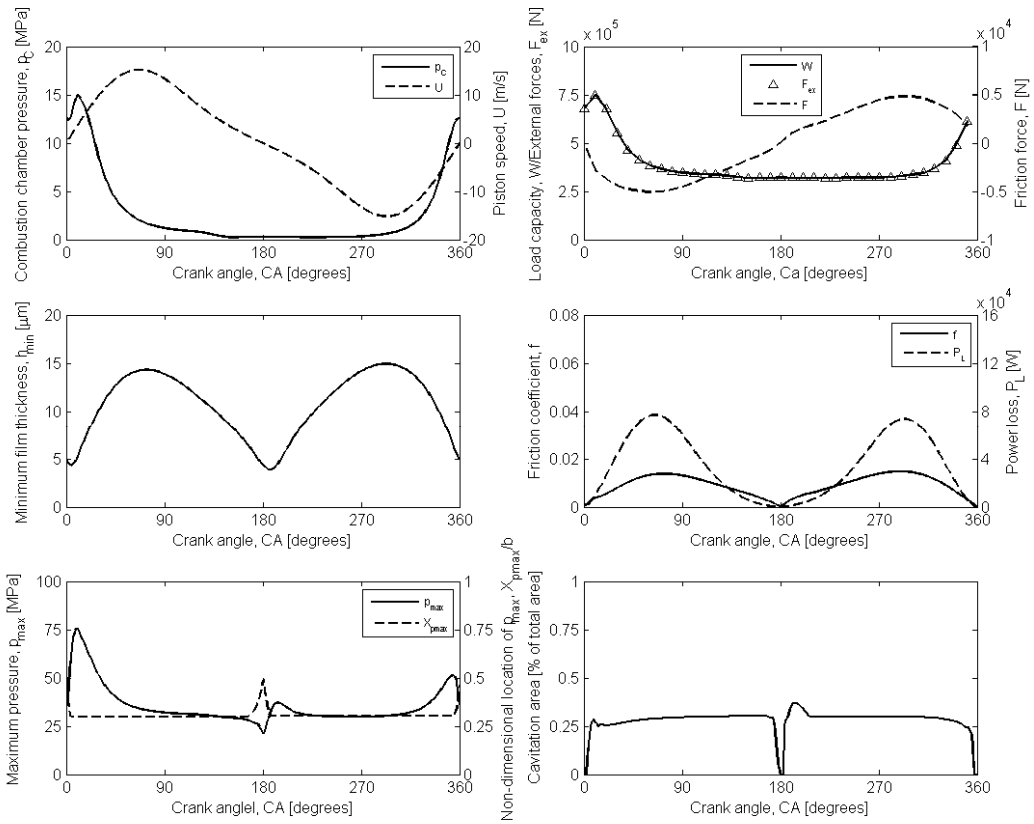

Fig. 73. Operational indices of the optimal hydrophobic case against crank angle for 100% engine load and 105 RPM; hydrophobic region from 0%-30% and 70%-100% and non-dimensional slip length b^*=10.

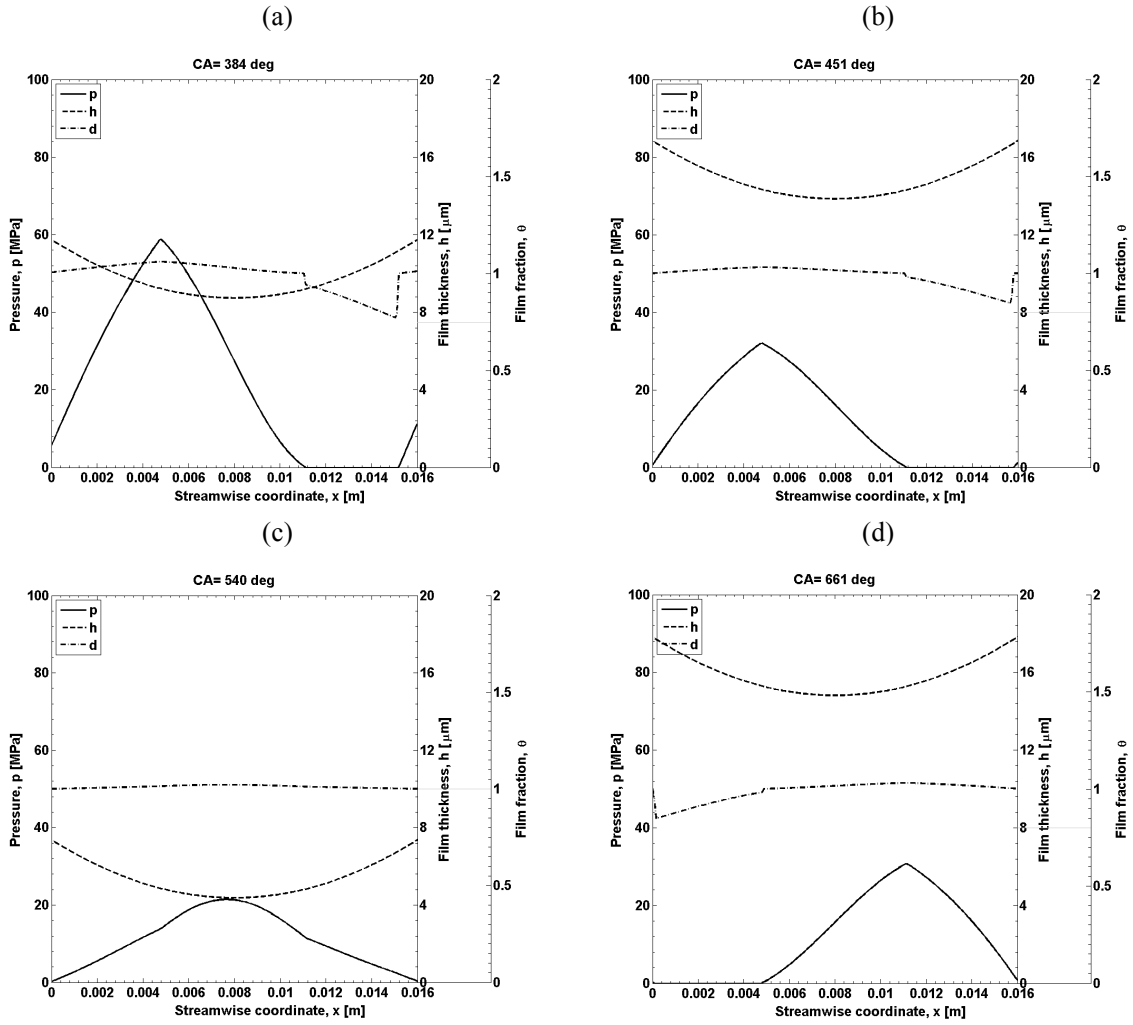

Fig. 74. Optimal hydrophobic design: Distributions of pressure, p, film thickness, h, and film fraction, θ, at crank angles (a) CA=384º, (b) CA=451º, (c) CA=540º and (d) CA=661º. Here, 100% load is assumed.

For the case of 100% engine load, the optimal hydrophobic ring design, increases the mean value of minimum film thickness over a full cycle by 20%, while mean power loss, over a full cycle, is decreased by **23%.**

The performance of the optimal hydrophobic ring design is also studied for the 25% engine load (25%). This is interesting, especially nowadays, since most ships operate in slow steaming, with the engine operating at very low loads, in order to decrease fuel consumption. The corresponding operational indices are compared in Fig. 75.

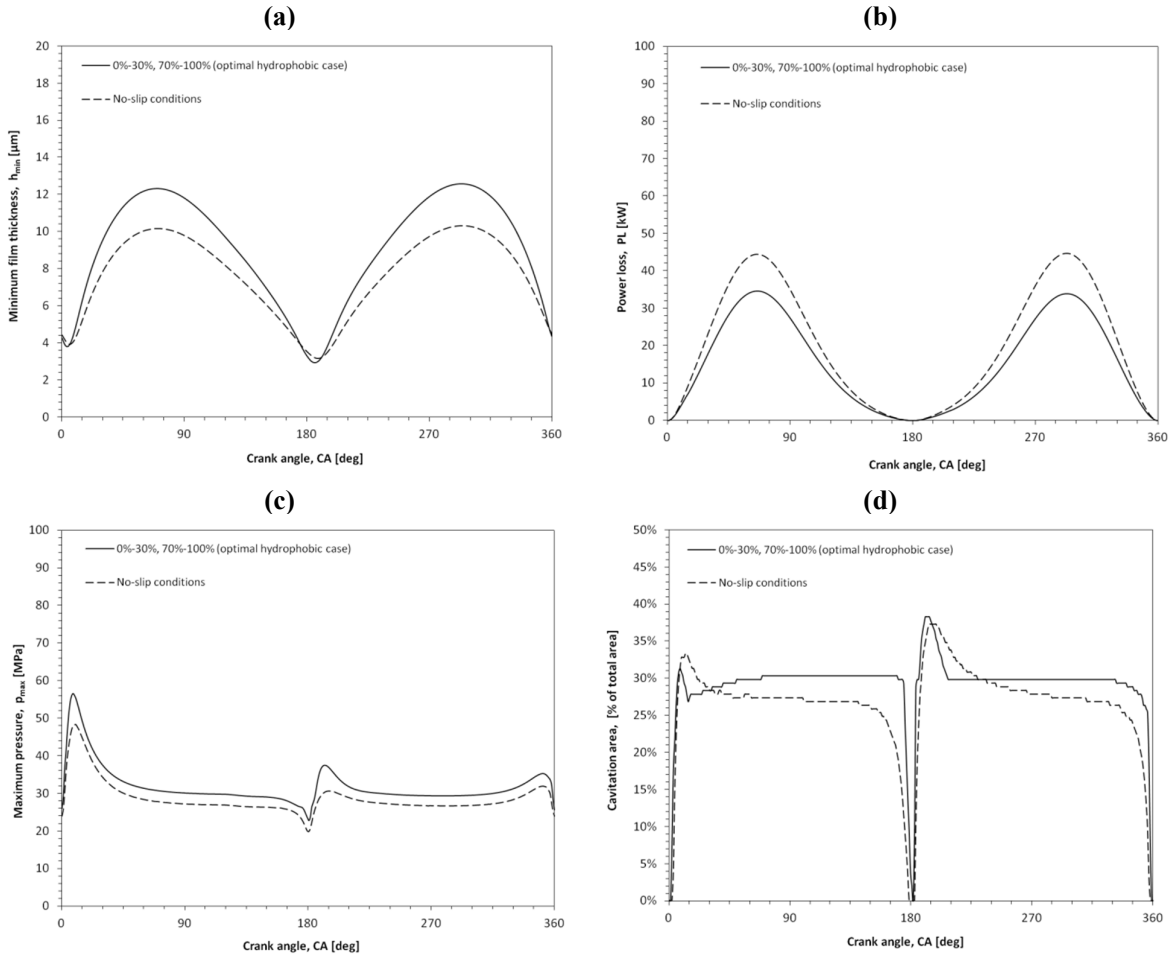

Fig. 75. (a) Minimum film thickness, (b) power loss, (c) maximum pressure and (d) percentage of cavitation area against crank angle, for 25% engine load: Comparison between the reference (no-slip) piston ring design and the optimal hydrophobic design.

The results of Fig. 75 verify that introduction of slip properties at both sides of piston ring substantially increase the minimum film thickness and decrease the power loss, for the case of engine load equal to 25% of the engine MCR.

Here, the optimal design exhibits a increase of the mean value of minimum film thickness over a full cycle by 19%, whereas mean power loss, over a full engine cycle, is decreased by **15%.**

4.6 Artificial surface texturing

In this section, the effect of introducing artificial surface texturing at part of the ring face on the ring performance characteristics is investigated. Computations are performed with the Reynolds equation with the Elrod-Adams mass conservation model.

Fig. 76 presents a piston ring with two artificially textured regions, one at the top half of the ring, and one at the bottom half. The location and extent of those regions are controlled by the following non-dimensional parameters:

- TB_s: Bottom textured region: Non-dimensional x coordinate of texture start location
- TB_e: Bottom textured region: Non-dimensional x coordinate of texture end location
- TT_s: Top textured region: Non-dimensional x coordinate of texture start location
- TT_e: Top textured region: Non-dimensional x coordinate of texture end location

Once those parameters are defined, the length of each textured area can be calculated. Next, this length is divided by the selected number of dimples, d_{num}, yielding the length of each dimple cell, d_{cl}. Finally, multiplying the length of dimple cell with the dimple density, $d_{density}$, yields the length of each dimple, d_{length}. Each dimple has a depth of d_{depth}. The corresponding texture geometry is presented in Fig. 76. The initial values of TB_s, TB_e, TT_s, TT_e, d_{num}, $d_{density}$ and d_{depth} are given in Table 6.

d_{num}	3
$d_{density}$	0.5
d_{depth}	5 μm
TB_s	0.1
TB_e	0.3
TT_s	0.7
TT_e	0.9

Table 6. Piston ring with artificial surface texturing: Parameters controlling the location and extent of the textured regions of Fig. 76, as well as the position, length and depth of the dimples.

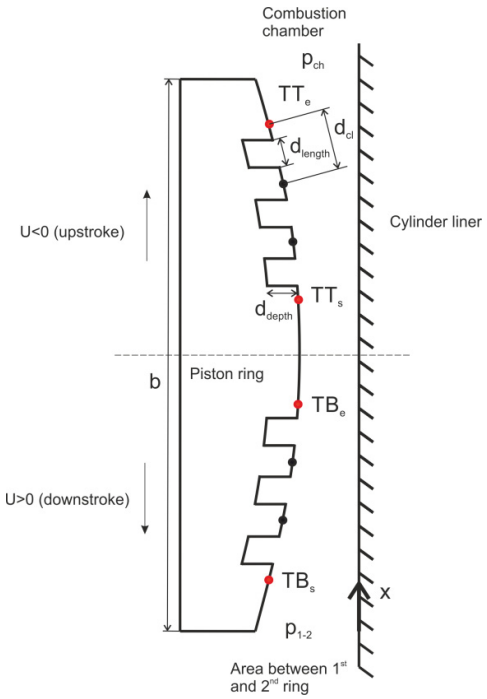

Fig. 76. Piston ring face profile including the geometry of the textured regions; the four dots mark the start and end of each hydrophobic area; TB_s: start of bottom textured region, TB_e: end of bottom textured region, TT_s: start of top textured region, TT_e: end of top textured region, d_{depth}: dimple depth, d_{cl}: length of each dimple cell, d_{length}: length of each dimple.

In Fig. 77, a comparison of the operational indices of the reference piston ring (section 4.3.6) with those of the textured ring corresponding to the design parameters of Table 6 is performed.

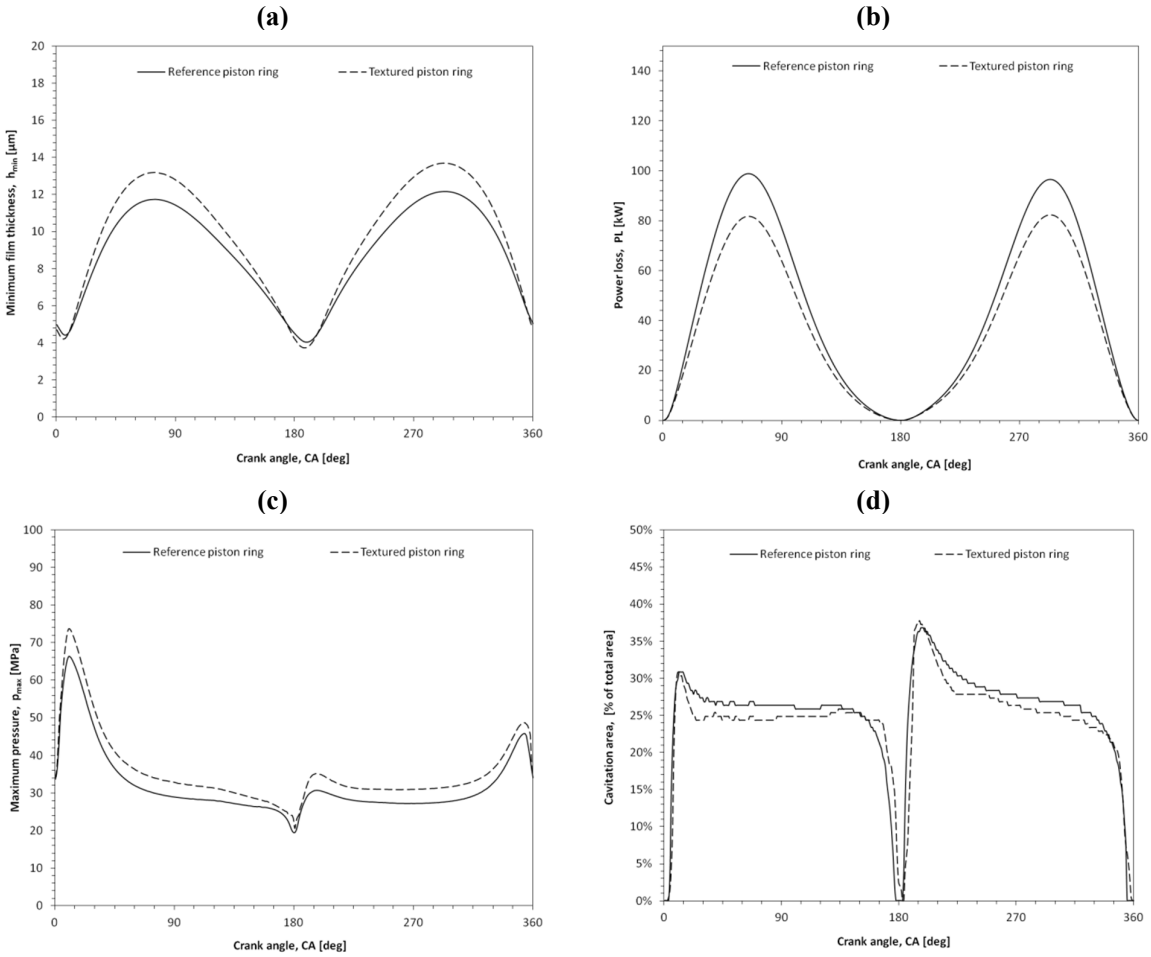

Fig. 77. (a) Minimum film thickness, (b) power loss, (c) maximum pressure and (d) percentage of cavitation area for 100% engine load, against crank angle, for the reference piston ring, and for the textured ring with parameters those of Table 6.

the introduction of artificial surface texturing is proved beneficial for the ring. In particular, minimum film thickness is increased, corresponding to higher load capacity, and power loss is substantially decreased. Maximum pressure is slightly increased, while the cavitation area is decreased for approximately 5%.

In the following paragraphs, a parametric analysis is performed for different values of TS_s, TB_e, TT_s, TT_e and d_{depth} to identify optimal design of the textured region.

4.6.1 Bottom textured region: Variation of texture start location

Here, values of TB_s between 0 and 0.2 are considered (TB_s=0.2 corresponds to a x-coordinate of the start of the bottom textured region equal to 0.2xb, where b is the ring width). In Fig. 78, the piston ring operational characteristics are presented versus crank angle, for different values of TB_s.

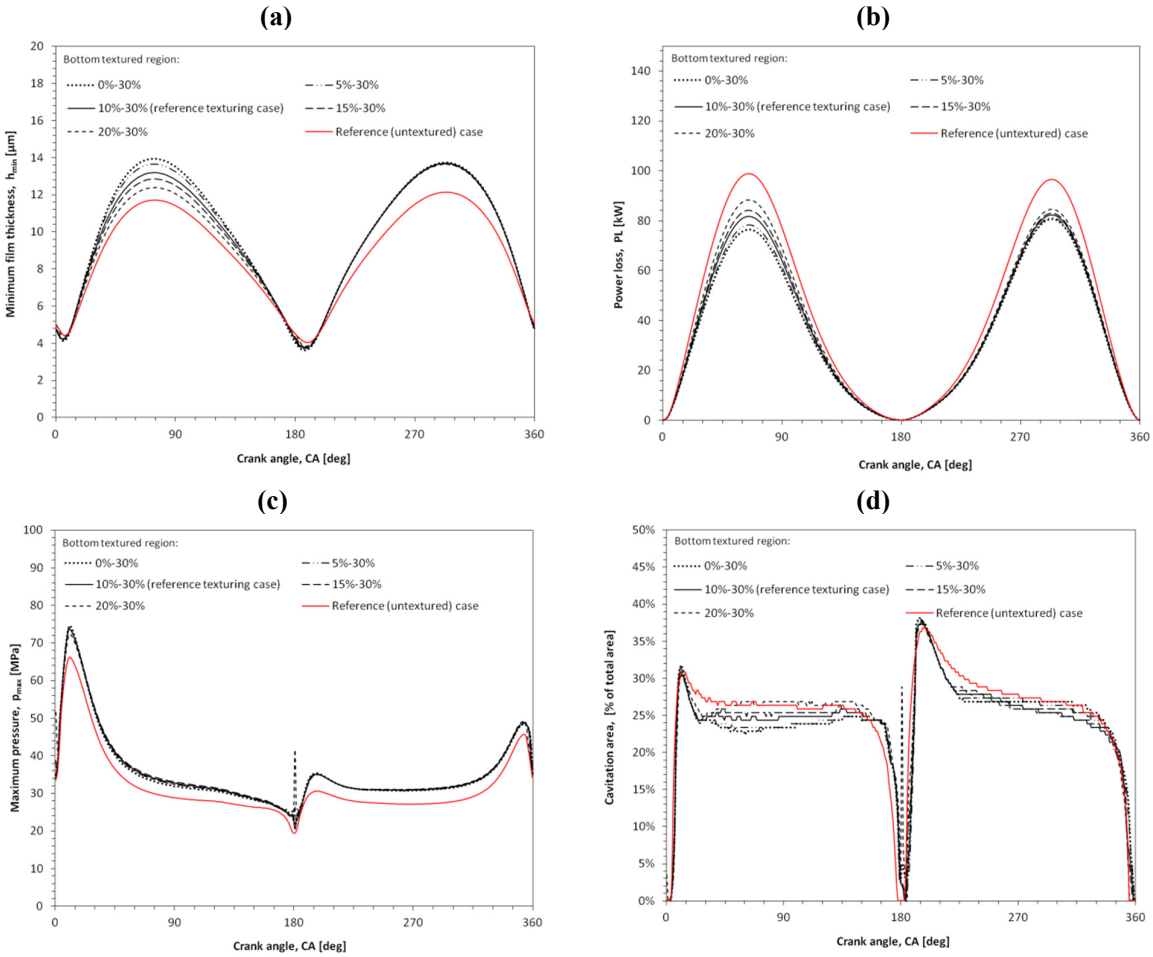

Fig. 78. (a) Minimum film thickness, (b) power loss, (c) maximum pressure and (d) percentage of cavitation area, against crank angle, for different values of the start of bottom textured region, TB_s.

The results of Fig. 78 suggest that variation of the start of the bottom textured area affects the ring operation only during the downstroke period. The largest textured area (0%-30%) has the best performance, since it further increases the minimum film thickness, decreases power loss, while affecting insignificantly the maximum pressure and the cavitation area.

4.6.2 Bottom textured region: Variation of texture end location

Here, values of TB_e between 0.2 and 0.4 are considered (TB_s=0.4 corresponds to a x-coordinate of the start of the bottom textured region equal to 0.4xb, where b is the ring width). In Fig. 79, the piston ring operational characteristics are presented versus crank angle, for different values of TB_e.

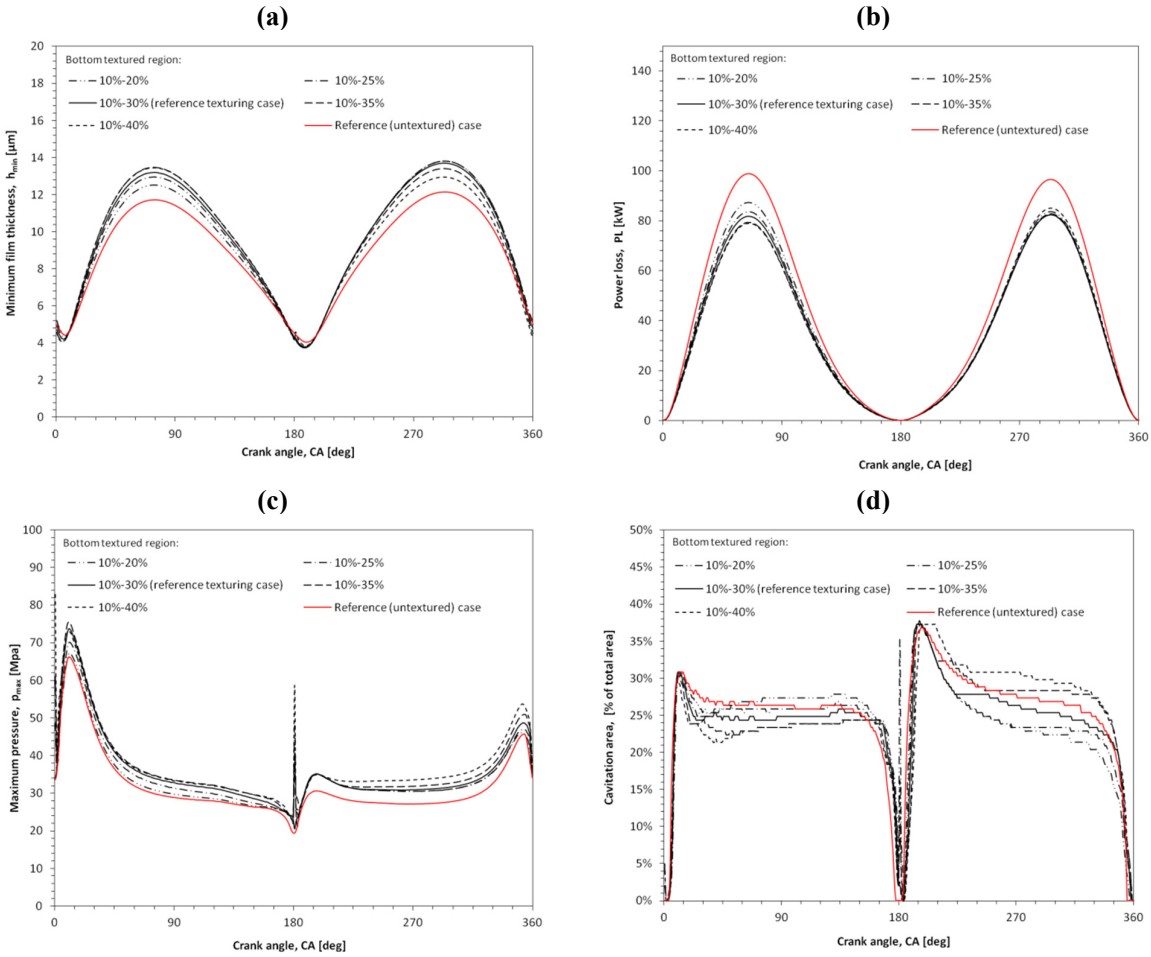

Fig. 79. (a) Minimum film thickness, (b) power loss, (c) maximum pressure and (d) percentage of cavitation area, against crank angle, for different values of the end of bottom textured region, TB_e.

From Fig. 79, it can be concluded that textured areas larger than the reference one (10%-30%) affect insignificantly the operational parameters, whereas smaller textured areas reduce minimum film thickness and increase power loss.

Merging the observations of Fig. 78 and Fig. 79, the optimum design of the bottom textured area is the one that extends from the start of the piston ring face profile (TB_s=0) until 30% of its total length (TB_e=0.3).

4.6.3 Top textured region: Variation of texture start location

Here, values of TT_s between 0.6 and 0.8 are considered (TT_s=0.6 corresponds to a x-coordinate of the start of the top textured region equal to 0.6xb, where b is the ring width). In Fig. 80, the piston ring operational characteristics are presented versus crank angle, for different values of TT_s.

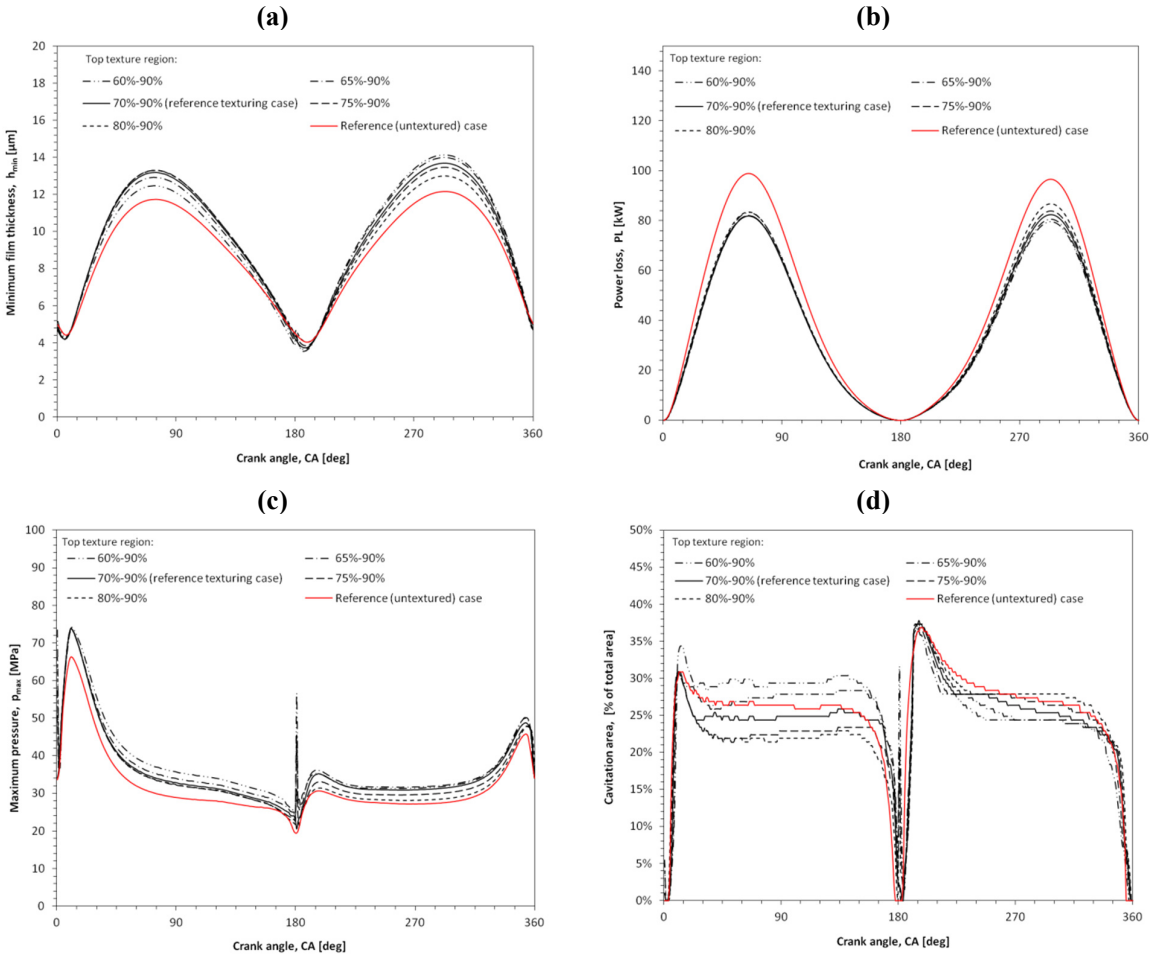

Fig. 80. (a) Minimum film thickness, (b) power loss, (c) maximum pressure and (d) percentage of cavitation area, against crank angle, for different values of the start of top textured region, TT_s.

Lower values TT_s (60%-90% and 65%-90%), which are equivalent to larger textured areas, provide a small increase of the minimum film thickness and a small decrease of power loss in the upstroke motion, while they decrease the former and increase the latter for the downstroke motion. Maximum pressure is decreased for larger textured region during the upstroke, while is increased during the downtroke for smaller textured region. Finally, cavitation region decreases for almost all the cases during the upstroke and it is increased for large textured regions during the downstroke.

4.6.4 Top textured region: Variation of texturing end location

Here, values of TT_e between 0.8 and 1 are considered (TT_e=0.8 corresponds to a x-coordinate of the start of the top textured region equal to 0.8xb, where b is the ring width). In Fig. 81, the piston ring operational characteristics are presented versus crank angle, for different values of TT_e.

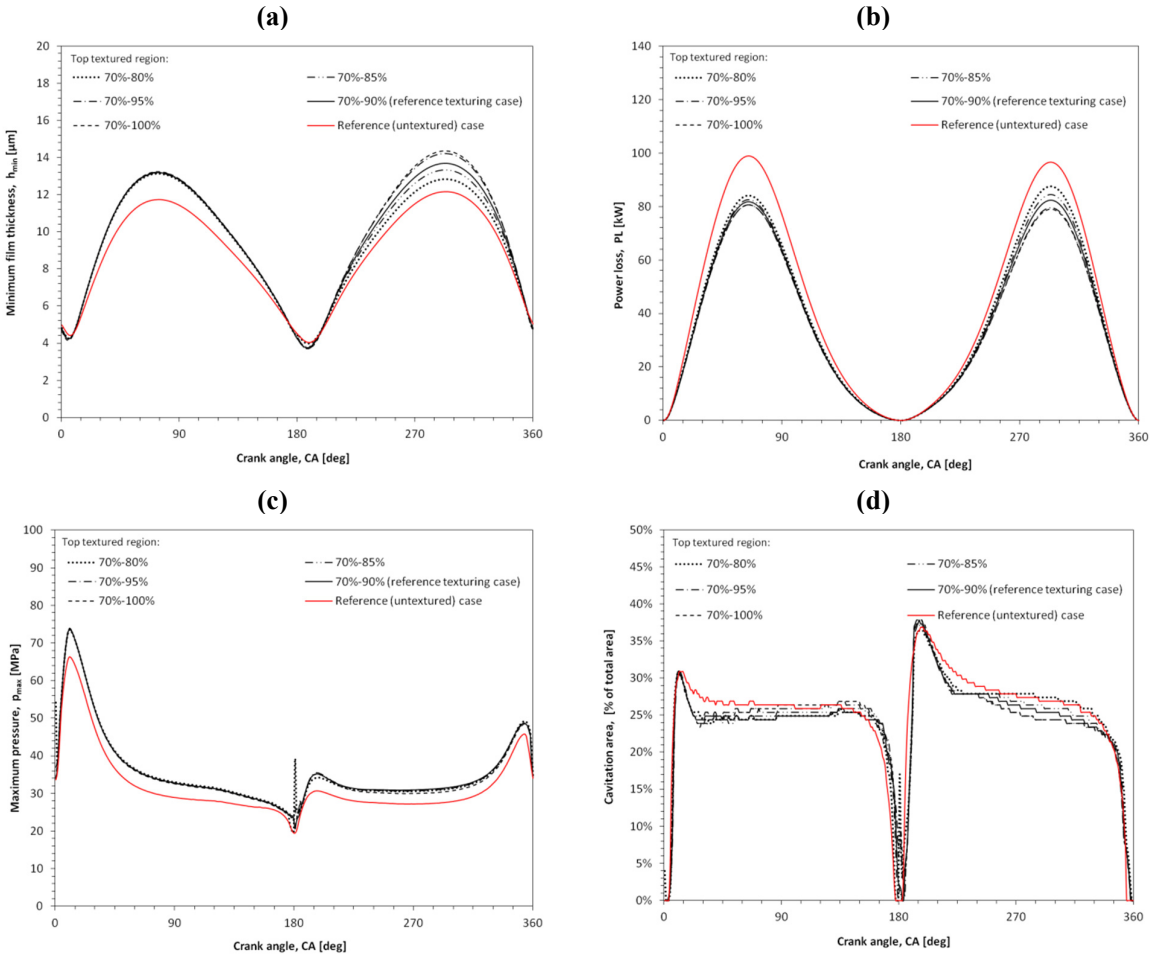

Fig. 81. (a) Minimum film thickness, (b) power loss, (c) maximum pressure and (d) percentage of cavitation area, against crank angle, for different values of the end of top textured region, TT_e.

Variation of TT_e affects the ring operation only during the downstroke. According to Fig. 81, the largest textured area (70%-100%) has the best performance, since it further increases the minimum film thickness, decreases power loss, while affecting insignificantly the maximum pressure and the cavitation area.

4.6.5 Texture depth

It is resulted from sections 4.6.1 to 4.6.4 that the best piston ring design with surface texturing is the one with textured areas expanding from 0% to 30%, which improves the operation of the downstroke motion, and from 70% to 100%, which improves the operation of the upstroke motion. These results were obtained for a texture depth equal to 5 μm; in the present section texture depth values of 2, 8, 10 and 15 μm are also considered.

In Fig. 82, the effect of different texture depth values on the operational indices of the piston ring (minimum film thickness, power loss, maximum pressure and percentage of cavitation area) is presented.

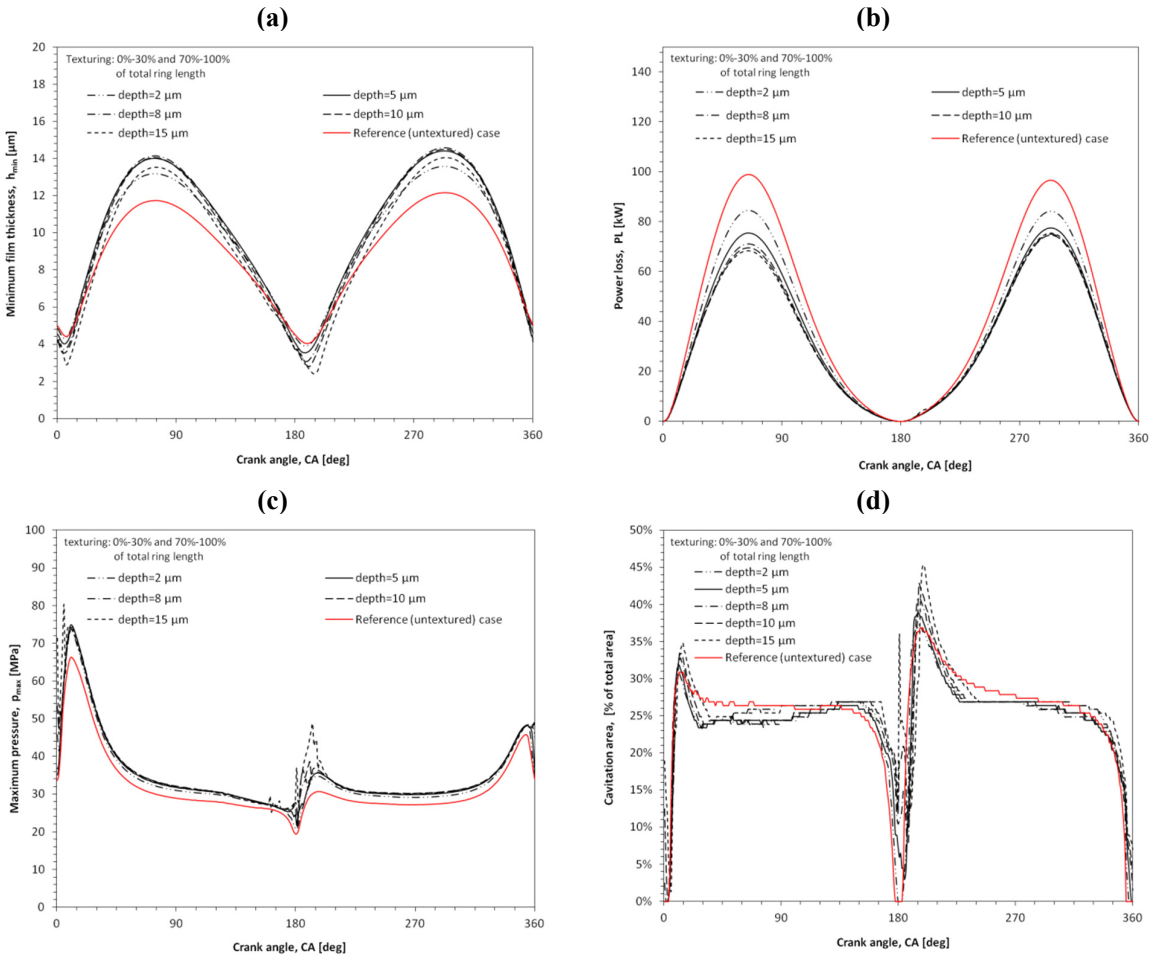

Fig. 82. (a) Minimum film thickness, (b) power loss, (c) maximum pressure and (d) percentage of cavitation area against crank angle, for different values of dimple depth. Here, the optimal textured ring is considered.

From Fig. 82 can be noticed that increasing dimple depth beyond 5 μm does not minimum film thickness (h_{min} is actually decreased for a dimple depth value of 15 μm). However, power loss maintains a decreasing trend with increasing dimple depth, achieving a decrease of approximately 30% for d_{depth}=15 μm . Maximum pressure and cavitation region are practically is not affected by the variation of dimple depth.

4.6.6 Optimal design with artificial surface texturing at the bottom and at the top part of the piston ring

From the parametric analysis of previous sections (4.6.1-4.6.5), the resultant optimal design is characterized by artificial surface texturing from 0% to 30% and 70% to 100% of the total piston ring surface, with a dimple depth value equal to 10 μm.

In Fig. 83, a comparison is made between the results of the reference (untextured) and of the optimal textured case. The operational characteristics of the optimally textured ring are summarized in Fig. 84, whereas in Fig. 85, pressure distribution and film fraction at several representative crank angles are plotted, in order to further understand this phenomenon.

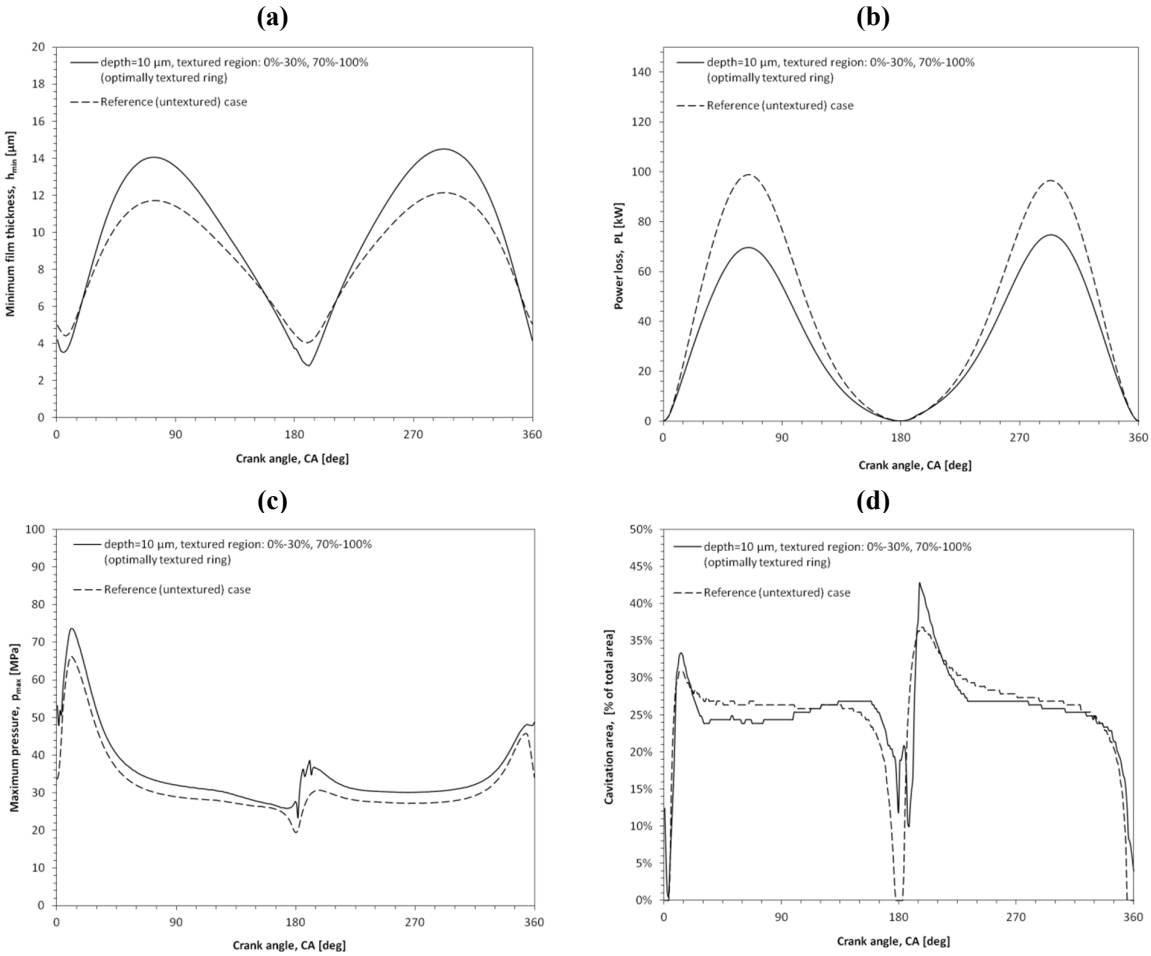

Fig. 83. (a) Minimum film thickness, (b) power loss, (c) maximum pressure and (d) percentage of cavitation area against crank angle, for 100% engine load: Comparison between the reference case (untextured) piston ring and the optimal textured design.

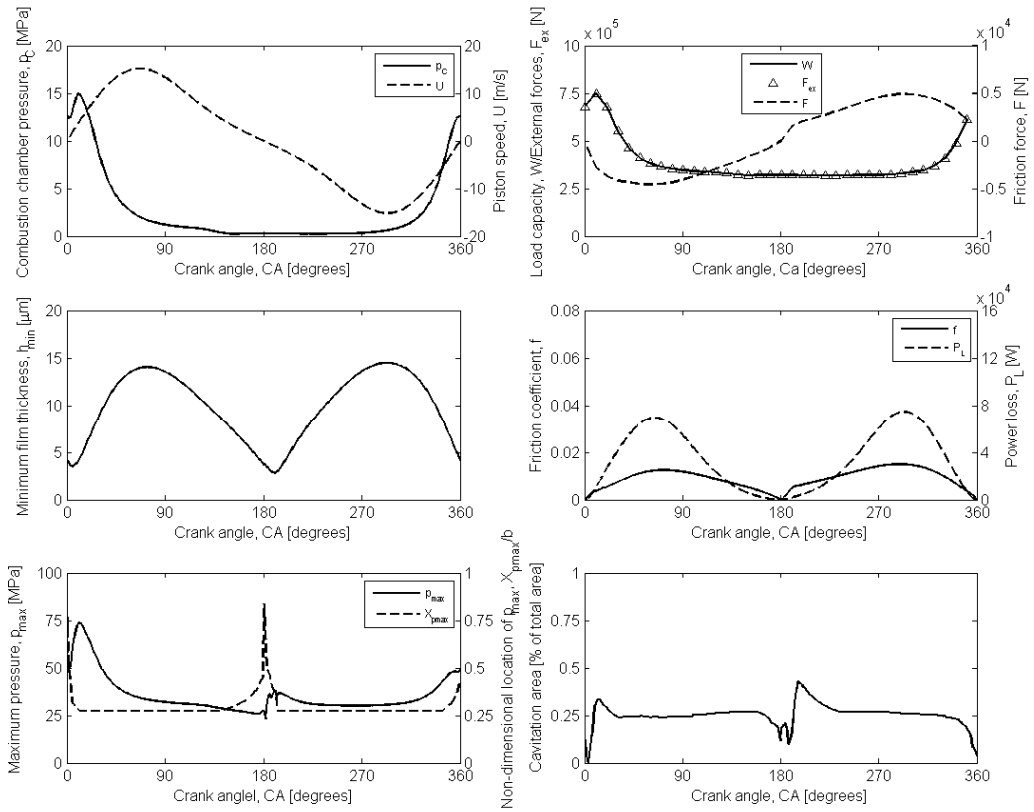

Fig. 84. Operational indices of the optimal texturing case against crank angle for 100% engine load and 105 RPM; textured region from 0%-30% and 70%-100% of the total ring length, and a dimple depth value of 10 µm.

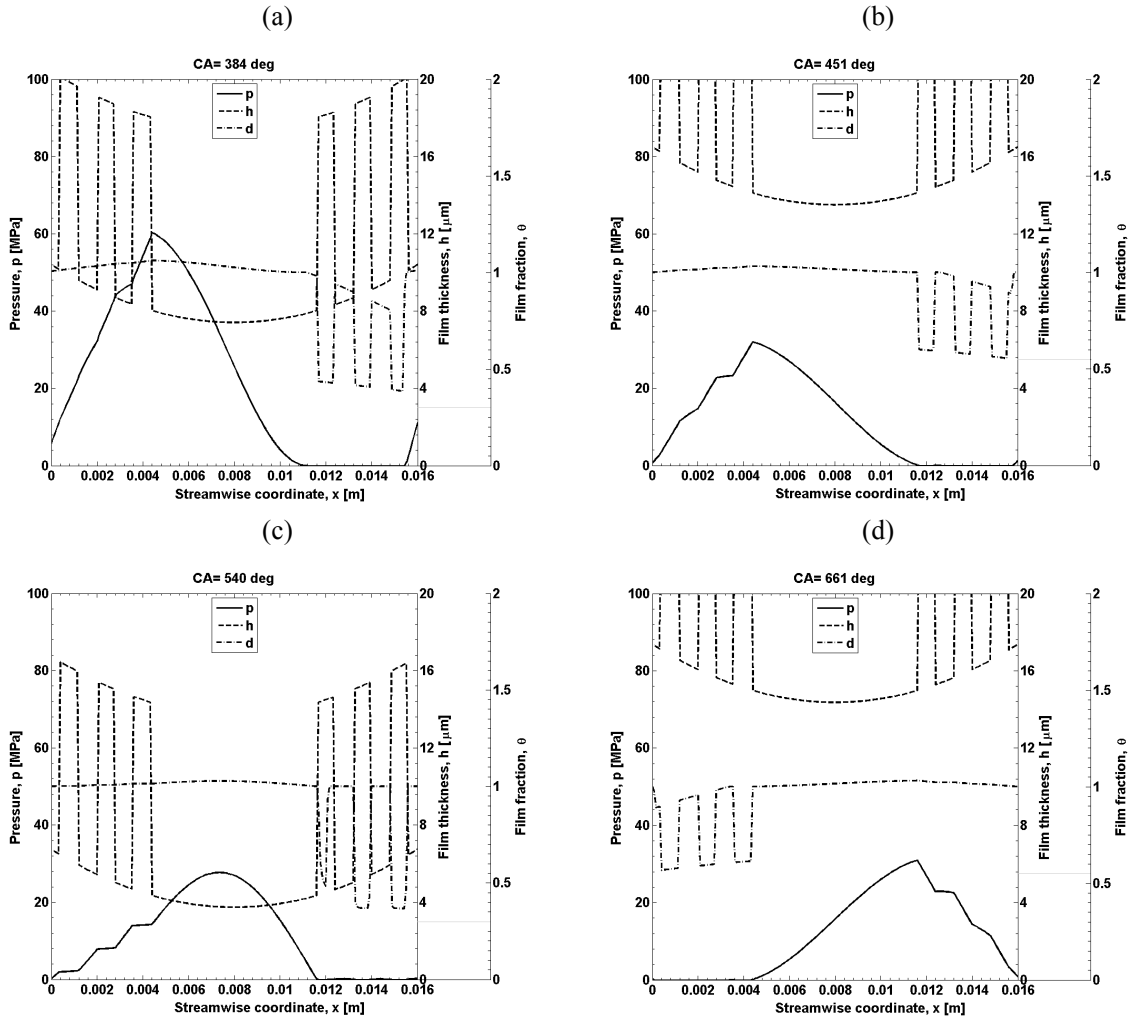

Fig. 85. Optimal textured ring design: Distributions of pressure, p, film thickness, h, and film fraction, θ, at crank angle values (a) CA=384º, (b) CA=451º, (c) CA=540º and (d) CA=661º. Here, 100% engine load is assumed.

For the case of 100% engine load, the optimally textured ring design, increases the mean value of minimum film thickness over a full cycle by 11%, while mean power loss, over a full cycle, is decreased by **25%.**

The performance of the optimally textured ring design is also studied for the 25% engine load. The corresponding operational indices are compared in Fig. 86.

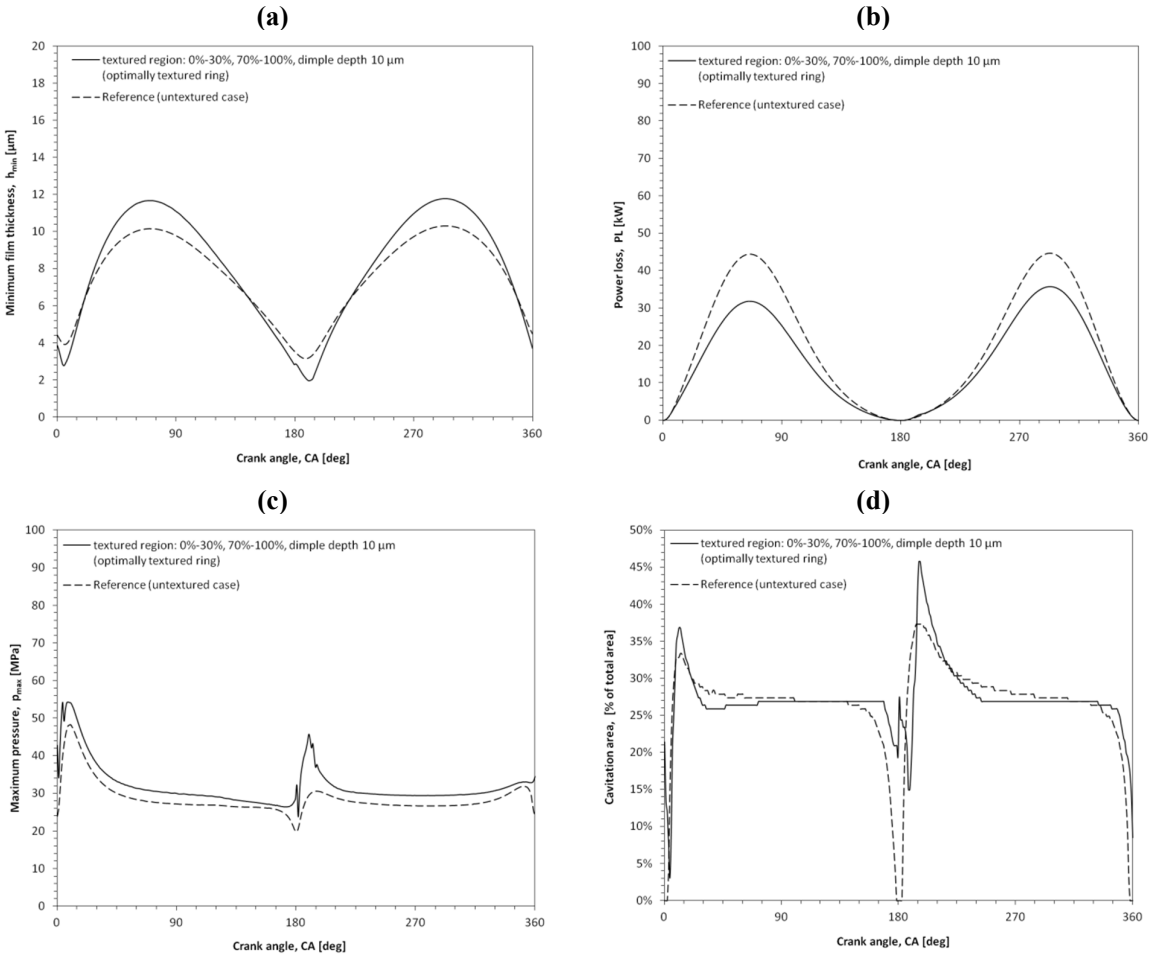

Fig. 86. (a) Minimum film thickness, (b) power loss, (c) maximum pressure and (d) percentage of cavitation area for against crank angle for 25% engine load: Comparison between the reference (untextured) piston ring and the optimally textured design.

Artificial texturing at both sides of the piston ring substantially increase minimum film thickness and decrease power loss, for the case of engine load equal to 25% of the engine MCR.

Here, the optimal design exhibits an increase of the mean value of minimum film thickness over a full cycle by 7%, whereas mean power loss, over a full cycle, is decreased by **15%.**

5. Conclusions and future work

5.1 Conclusions

In the framework of the present thesis, software tools have been developed for the solution of hydrodynamic lubrication problems in piston rings under transient loading conditions. Two different solution algorithms were formulated, namely one for the classic Reynolds equation with Reynolds boundary conditions, and a second for the Reynolds equation with the Elrod-Adams mass conservation model. The Elrod-Adams model handles more effectively the cavitation boundaries and takes into account the lubricant density. Both solvers have been extended to account for ring surface with hydrophobic parts, and the differential equations are solved using the Finite Difference Model (FDM). The calculations of each solver have been validated against results from the international literature; a very good agreement was found for all the considered cases.

The developed software has been applied to compute the performance characteristics of the piston rings of a large two-stroke marine Diesel engine, for two loading conditions, corresponding to power output of 100% and 25% of the engine MCR. First, a mesh study has been performed to decide the proper discretization that results in a mesh independent solution. Next, a study of the lubricant bulk modulus, a basic parameter of the Elrod-Adams model, has been performed to identify its effect on the computed ring performance. Further, comparisons were made between the two previously mentioned solution algorithms, and the effect of time derivatives (squeeze film terms) has also been investigated.

The reference piston ring design has been extensively studied to identify the effect of its main design parameters (curvature, offset, viscosity) on performance (minimum film thickness, power loss, maximum pressure, etc.). After this parametric analysis, part of the ring surface has been assumed to have hydrophobicity or artificial surface texturing. A detailed parametric study has been performed to identify the corresponding optimum design parameters. The results demonstrate a substantial reduction of power loss, of the order of 23%, when hydrophobicity is applied properly to the ring surface, and of the order of 25%, when parts of the ring surface are properly textured. At the same time, the mean value of minimum film thickness is increased by approximately 20% and 11%, respectively, meaning that load carrying capacity is also substantially increased. The decrease in friction loss and the simultaneous increase of load capacity result in decreased values of friction coefficient.

5.2 Future work

In the present work, the piston ring was assumed to operate under fully flooded lubrication conditions. In practice, an engine has a series of piston rings, therefore oil starvation conditions are anticipated at several of those rings. A future study could aim at proper modification of the Elrod-Adams mass conservation model to account for oil starvation boundary conditions.

A further enhancement of the present work would be the study of the whole ring pack, assuming mass conservation conditions in the whole piston ring assembly.

Finally, the tilt motion and mechanical deformations of the piston ring, neglected in the present thesis, could be taken into account in the framework of an elastohydrodynamic (EHD) analysis approach.

5. Literature

1. Σταματελόπουλος Δ., "Πειραματική Μελέτη Υδροδυναμικής Λίπανσης σε Ακτινικά Έδρανα", Αθήνα, Ιούλιος, 2013.
2. Yukio H., "Hydrodynamic Lubrication", Springer, Japan, 2005.
3. Stachowiak G., Batchelor A., "Engineering Tribology", Butterworth Heinemann, 2011.
4. Jeng Y.-R., "Theoretical Analysis of Piston-Ring Lubrication Part-I Fooly Flooded Lubrication", Tribology Transactions, Vol. 35(4), pp 696-706, 1992.
5. Jeng Y.-R., "Theoretical Analysis of Piston-Ring Lubrication Part-II Staeved Lubrication and Its Application to a Complete Ring Pack", STLE Tribology Transactions, Vol. 35(4), pp 707-714, 1992.
6. Wakuri Y et al, "Piston ring friction in internal combustion engines", Tribology International, Vol. 25, pp 299-308, 1992.
7. Elrod H.G, Adams M.L., "A computer program for cavitation and starvation problems", Cavitation and Related Phenomena in Lubrication, pp 37-41,1974.
8. Elrod H.G., "A Cavitation Algorithm", ASME Journal of Lubrication Technology, Vol. 103(3), pp 350-354,1981.
9. Vijayaraghavan D. and Keith T.G. Jr., "Development and Evaluation of a Cavitation Algorithm", STLE Triboligal Transactions, Vol. 32(2), pp 225-233, 1989.
10. Khonsari M. M. and Feshangary M., "A Modification of the Switch Function in the Elrod Cavitation Algorithm", ASME Journal of Tribology, Vol. 133, 024501, pp 1-4, 2011.
11. Giacopini M. et al, "A Mass-Conserving Complementarity Formulation to Study Lubricant Films in the Presence of Cavitation", ASME Journal of Tribology, Vol. 132, 041702, pp 1-12, 2010.
12. Fatu A., et al, "Wall slip effects in (elasto) hydrodynamic journal bearings", Tribology International, doi: 10.1016/j.triboint.2011.03.003 2011.
13. Pavlioglou S.K. et al, "Tribological Optimization of Thrust Bearings Operated with Lubricants of Spatially Varying Viscosity", ASME GT2014-25292, pp 1-10, 2014.
14. GuoJun M., Cheng W.W, Ping Z., "Hydrodynamics of slip wedge and optimization of surface slip property", Sci China-Phys Mech Astron, Vol. 50(3), pp 321-330, 2007.
15. Etsion I., Kligerman Y., Shinkarenko A., "Improved Tribological Performance of Piston Rings by Partial Surface Texturing" Transactions of the ASME, Vol. 127, pp 632-638, 2005.
16. Papadopoulos C.I., Efstathiou E.E., Nikolakopoulos P. G., Kaiktsis L., "Geometry Optimization of Textured Three-Dimensional Micro-thrust Bearings", ASME Journal of Tribology, Vol. 133, 041702, pp 1-14, 2011.
17. Xiong S., Wang Q.J., "Steady-state Hydrodynamic Lubrication Modeled with the Payvar-Salant Mass Conservation Model", ASME Journal of Tribology, Vol. 134, 031703, pp1-16.
18. Κυρτάτος Ν., "Ναυτικοί Κινητήρες Diesel - Θέματα Σχεδίασης και Λειτουργίας", Αθήνα, Νοέμβριος 1993.
19. US Department of Energy, "DOE Fundamentals Handbook - Mechanical Science Vol. 1 of 2, Diesel Engine Fundamentals", Washington 1993.
20. Anderson P., Tamminen J., Sandström C. E., "Piston ring tribology - A literature survey", VTT Industrial Systems.

21. Bharat Bhushan, “Modern Triblogy Handbook, Two volume set”, CRC Press, 2000.
22. Bertocchi L., Strozzi A., “A Linear Complementarity Approach to Solve Elastohydrodynamic Lubrication Problems in the Presence of Cavitation”, March 2013.
23. Dhunput A., Teodorescu M., Arcoumanis C., “Investigation of cavitation development in the lubricant film of piston-ring assemblies”, IOP Publishing, 2005.
24. Khonsari M. M. and Booser E. R., “Applied Tribology: Bearing Design and Lubrication”, Second Edition, Wiley, 2008.
25. Petrovsky N., "Marine Internal Combustion Engines", MIR Publishers, 1976.
26. Christensen O., "Cylinder lubrication of two-stroke crosshead marine Diesel engines", Wartsila Technical Journal, 2010.
27. http://www.ringleader.net/piston-ring-materials/3/index.phtml.
28. Kontoulis P., Chrysakis C., Kaiktsis L., "Evaluation of Pilot Injections in a Large Two-Stroke Marine Diesel Engine, Using CFD and T-φ Mapping", COMODIA, 2008.
29. Etsion I., "Laser Surface Texturing" (presentation).
30. http://en.wikipedia.org/wiki/Lotus_effect.

Appendix A

Derivation of Reynolds equation for hydrophobic surfaces

Starting from Eq. (9) of section 2.2.3, velocity u can be calculated:

$$\frac{\partial p}{\partial x}=\frac{\partial}{\partial z}\left(\eta\frac{\partial u}{\partial z}\right)=>\left(\frac{\partial p}{\partial x}\right)\partial z=\partial\left(\eta\frac{\partial u}{\partial z}\right)=>\frac{\partial p}{\partial x}z+C_1=\eta\frac{\partial u}{\partial z}=>\left(\frac{\partial p}{\partial x}z+C_1\right)\partial z=\eta\partial u=>$$

$$\frac{\partial p}{\partial x}\frac{z^2}{2}+C_1z+C_2=\eta u=>u=\frac{\partial p}{\partial x}\frac{z^2}{2\eta}+\frac{C_1}{\eta}z+\frac{C_2}{\eta} \tag{61}$$

Differentiating Eq. (61) yields:

$$\frac{\partial p}{\partial x}z+C_1=\eta\frac{\partial u}{\partial z} \tag{62}$$

The boundary conditions at the liner and ring surfaces are:

$$u_{z=0}=U-a_l\left(-\eta\left.\frac{\partial u}{\partial z}\right|_{z=0}-\tau_{C,l}\right) \tag{63}$$

$$u_{z=h}=a_r\left(-\eta\left.\frac{\theta u}{\theta z}\right|_{z=h}-\tau_{C,r}\right) \tag{64}$$

where $\tau_{C,l}$ and $\tau_{C,r}$ are the critical shear stress values for the liner and the piston ring, respectively.

The first derivative of velocity at z=0 is:

$$\eta\left.\frac{\partial u}{\partial z}\right|_{z=0}=C_1 \tag{65}$$

Similarly, the first derivative of velocity at z=h is:

$$\eta\left.\frac{\partial u}{\partial z}\right|_{z=h}=C_1+\frac{\partial p}{\partial x}h \tag{66}$$

Velocities at z=0 and z=h can be calculated as:

$$u_{z=0}=\frac{C_2}{\eta} \tag{67}$$

$$u_{z=h}=\frac{\partial p}{\partial x}\frac{h^2}{2\eta}+\frac{C_1}{\eta}h+\frac{C_2}{\eta} \tag{68}$$

Use of Eq. (63), (65) and (67) results in:

$$U - a_l\left[-C_1 - \tau_{C,l}\right] = \frac{C_2}{\eta} \tag{69}$$

From Eq. (64), (66) and (68):

$$a_r\left[-C_1 - \frac{\partial p}{\partial x}h - \tau_{C,r}\right] = \frac{\partial p}{\partial x}\frac{h^2}{2\eta} + \frac{C_1}{\eta}h + \frac{C_2}{\eta} \tag{70}$$

Solving Eq. (69) for C_2:

$$C_2 = U\eta - \eta a_l\left(-C_1 - \tau_{C,l}\right) \tag{71}$$

Substituting Eq. (71) into Eq. (70) yields:

$$-a_r\frac{\partial p}{\partial x}h - a_r\tau_{C,r} - \frac{\partial p}{\partial x}\frac{h^2}{2\eta} - U - a_l\tau_{C,l} = a_lC_1 + a_rC_1 + \frac{C_1}{\eta}h \Rightarrow$$

$$C_1 = -\frac{a_r\frac{\partial p}{\theta x}h\eta + a_r\tau_{C,r}\eta + \frac{\partial p}{\partial x}\frac{h^2}{2} + U\eta + a_l\tau_{C,l}\eta}{h + \eta(a_l + a_r)} \tag{72}$$

C_2 can be calculated from Eq. (71):

$$C_2 = U\eta - \eta a_l\left[\frac{a_h\frac{\partial p}{\partial x}h\eta + \frac{\partial p}{\partial x}\frac{h^2}{2} + U\eta + \eta a_r\left(\tau_{C,r} - \tau_{C,l}\right) - \tau_{C,l}h}{h + \eta(a_l + a_r)}\right] \tag{73}$$

Substituting constants C_1 and C_2 into Eq. (61) yields the velocity along direction x:

$$\begin{aligned} u = {} & \frac{\partial p}{\partial x}\frac{z^2}{2\eta} - z\left[\frac{\partial p}{\partial x}\frac{h}{2\eta}\frac{2\eta a_r + h}{h + \eta(a_l + a_r)} + \frac{U}{h + \eta(a_l + a_r)} + \frac{a_r\tau_{C,r} + a_l\tau_{C,l}}{h + \eta(a_l + a_r)}\right] + \\ & + U\frac{h + \eta a_r}{h + \eta\left(a_l + a_r\right)} - \frac{\partial p}{\partial x}\frac{h}{2\eta}\frac{2a_la_r\eta^2 + a_lh\eta}{h + \eta\left(a_l + a_r\right)} - a_l\frac{\eta a_r\left(\tau_{C,r} - \tau_{C,l}\right) - \tau_{C,l}h}{h + \eta\left(a_l + a_r\right)} \end{aligned} \tag{74}$$

Continuity of mass demands that:

$$\int_0^h \frac{\partial(\rho u)}{\partial x}dz + \int_0^h \frac{\partial(\rho v)}{\partial y}dz + \int_0^h \frac{\partial(\rho w)}{\partial z}dz + \int_0^h \frac{\partial \rho}{\partial t}dz = 0 \tag{75}$$

Using the Leibnitz rule for differentiation of integrals, the first term of Eq. (75) can be written as:

$$\int_0^h \frac{\partial(\rho u)}{\partial x} dz = \frac{\partial}{\partial x}\int_0^h \rho u(z) dz - \rho u(h)\frac{\partial h}{\partial x} \tag{76}$$

Substituting Eq. (74) into the first part of Eq. (76) results in:

$$\begin{aligned}
&\int_0^h \rho u(z) dz = \rho \frac{\partial p}{\partial x}\frac{h^3}{6\eta} - \rho \frac{h^2}{2}\left[\frac{\partial p}{\partial x}\frac{h}{2\eta}\frac{2\eta a_r + h}{h+\eta(a_l+a_r)} + \frac{U}{h+\eta(a_l+a_r)} + \frac{a_r\tau_{C,r} + a_l\tau_{C,l}}{h+\eta(a_l+a_r)}\right] + \\
&+\rho U h \frac{h+\eta a_r}{h+\eta\left(a_l+a_r\right)} - \rho h \frac{\partial p}{\partial x}\frac{h}{2\eta}\frac{2a_l a_r\eta^2 + a_l h\eta}{h+\eta\left(a_l+a_r\right)} - \rho h a_l \frac{\eta a_r\left(\tau_{C,r}-\tau_{C,l}\right) - \tau_{C,l}h}{h+\eta\left(a_l+a_r\right)} = \\
&-\rho\frac{h^2}{12\mu}\frac{\partial p}{\partial x}\frac{h^2 + 4\eta\left(a_l+a_r\right)h + 12\eta^2 a_l a_r}{h+\eta\left(a_l+a_r\right)} + \rho\frac{Uh}{2}\frac{h+2\eta a_r}{h+\eta\left(a_l+a_r\right)} + \\
&+\rho\frac{1}{2}\frac{h^2\left(a_l\tau_{C,l} - a_r\tau_{C,r}\right) + 2a_l a_r\eta\left(\tau_{C,l}-\tau_{C,r}\right)h}{h+\eta\left(a_l+a_r\right)}
\end{aligned} \tag{77}$$

Substituting Eq. (74) into the second part of Eq. (76) results in:

$$\begin{aligned}
&\rho u(h) = \rho\frac{\partial p}{\partial x}\frac{h^2}{2\eta} - \rho h\left[\frac{\partial p}{\partial x}\frac{h}{2\eta}\frac{2\eta a_r + h}{h+\eta(a_l+a_r)} + \frac{U}{h+\eta(a_l+a_r)} + \frac{a_r\tau_{C,r} + a_l\tau_{C,l}}{h+\eta(a_l+a_r)}\right] + \\
&+\rho U\frac{h+\eta a_r}{h+\eta\left(a_l+a_r\right)} - \rho\frac{\partial p}{\partial x}\frac{h}{2\eta}\frac{2a_l a_r\eta^2 + a_l h\eta}{h+\eta\left(a_l+a_r\right)} - \rho a_l\frac{\eta a_r\left(\tau_{C,r}-\tau_{C,l}\right) - \tau_{C,l}h}{h+\eta\left(a_l+a_r\right)} \Rightarrow \\
&\rho u(h) = -\rho\frac{\partial p}{\partial x}\frac{h}{2\eta}\frac{\eta a_r h + 2a_l a_r\eta^2}{h+\eta\left(a_l+a_r\right)} + \rho U\frac{\eta a_r}{h+\eta\left(a_l+a_r\right)} - \rho\frac{\eta a_r a_l\left(\tau_{C,r}-\tau_{C,l}\right) + a_r\tau_{C,r}h}{h+\eta\left(a_l+a_r\right)}
\end{aligned} \tag{78}$$

Thus the first term of Eq. (75) is written as:

$$\begin{aligned}
&\int_0^h \frac{\partial(\rho u)}{\theta x} dz = -\frac{\partial}{\partial x}\left(\frac{\rho h^2}{12\eta}\frac{\theta p}{\theta x}\frac{h^2 + 4\eta\left(a_l+a_r\right)h + 12\eta^2 a_l a_r}{h+\eta\left(a_l+a_r\right)}\right) + \frac{\partial}{\partial x}\frac{U}{2}\left(\rho h\frac{h+2\eta a_r}{h+\eta\left(a_l+a_r\right)}\right) + \\
&+\frac{\partial}{\partial x}\frac{1}{2}\left(\rho h\frac{h\left(a_l\tau_{C,l} - a_r\tau_{C,r}\right) + 2a_l a_r\eta\left(\tau_{C,l}-\tau_{C,r}\right)}{h+\eta\left(a_l+a_r\right)}\right) + \\
&+\frac{\partial h}{\partial x}\frac{\partial p}{\partial x}\frac{\rho h}{2\eta}\frac{\eta a_r h + 2a_l a_r\eta^2}{h+\eta\left(a_l+a_r\right)} - \frac{\partial h}{\partial x}\rho U\frac{\eta a_r}{h+\eta\left(a_l+a_r\right)} + \frac{\partial h}{\partial x}\rho\frac{\eta a_r a_l\left(\tau_{C,r}-\tau_{C,l}\right) + a_r\tau_{C,r}h}{h+\eta\left(a_l+a_r\right)}
\end{aligned} \tag{79}$$

A similar procedure is followed for the derivation of velocity v along the y direction.

$$\frac{\partial p}{\partial y}=\frac{\partial}{\partial z}\left(\eta\frac{\partial v}{\partial z}\right)=>\left(\frac{\partial p}{\partial y}\right)\partial z=\partial\left(\eta\frac{\partial v}{\partial z}\right)=>\frac{\partial p}{\partial y}z+C_1=\eta\frac{\partial v}{\partial z}=>\left(\frac{\partial p}{\partial y}z+C_1\right)\partial z=\eta\partial v=>$$

$$\frac{\partial p}{\partial y}\frac{z^2}{2}+C_1z+C_2=\mu v=>v=\frac{\partial p}{\partial y}\frac{z^2}{2\eta}+\frac{C_1}{\eta}z+\frac{C_2}{\eta} \tag{80}$$

The first derivative of velocity along y direction is:

$$\frac{\partial p}{\partial y}z+C_1=\eta\frac{\partial v}{\partial z} \tag{81}$$

The boundary conditions are derived from similar considerations, as those made for the boundary conditions of the velocity u along the x direction. The only difference now is that the velocity is caused only from the pressure gradient dp/dy (see Fig. 20), since no wall velocity V exists in the y direction.

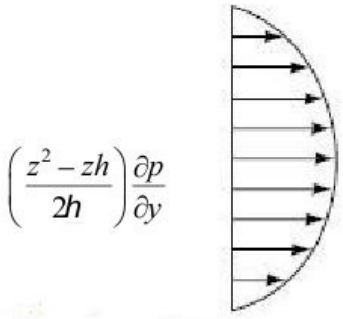

Fig. 87. Velocity parabolic profile caused from the pressure derivative

$$v_{z=0}=a_l\left(\eta\left.\frac{\partial v}{\partial z}\right|_{z=0}-\tau_{C,l}\right) \tag{82}$$

$$v_{z=h}=a_r\left(-\eta\left.\frac{\partial v}{\partial z}\right|_{z=h}-\tau_{C,r}\right) \tag{83}$$

The first derivative of velocity at z=0 is:

$$\eta\left.\frac{\partial v}{\partial z}\right|_{z=0}=C_1 \tag{84}$$

Similarly, the first derivative of velocity at z=h is:

$$\eta\left.\frac{\partial v}{\partial z}\right|_{z=h}=C_1+\frac{\partial p}{\partial y}h \tag{85}$$

Eq. (80) yields:

$$v_{z=0} = \frac{C_2}{\eta} \tag{86}$$

$$v_{z=h} = \frac{\partial p}{\partial y}\frac{h^2}{2\eta} + \frac{C_1}{\eta}h + \frac{C_2}{\eta} \tag{87}$$

Eq. (82), (84) and (86) result in:

$$a_l\left[C_1 - \tau_{C,l}\right] = \frac{C_2}{\eta} \tag{88}$$

From (83), (85) and (87):

$$a_r\left[-C_1 - \frac{\partial p}{\partial y}h - \tau_{C,r}\right] = \frac{\partial p}{\partial y}\frac{h^2}{2\eta} + \frac{C_1}{\eta}h + \frac{C_2}{\eta} \tag{89}$$

Solving Eq. (88) for C_2:

$$C_2 = \eta a_l\left(C_1 - \tau_{C,l}\right) \tag{90}$$

Substituting Eq. (90) into Eq. (89):

$$-a_r\frac{\partial p}{\partial y}h - a_r\tau_{C,r} - \frac{\partial p}{\partial y}\frac{h^2}{2\eta} + a_l\tau_{C,l} = \frac{C_1}{\eta}h + a_lC_1 + a_rC_1 \Rightarrow$$

$$C_1 = -\frac{a_r\frac{\partial p}{\partial y}h\eta + a_r\tau_{C,r}\eta + \frac{\partial p}{\partial y}\frac{h^2}{2} - a_l\tau_{C,l}\eta}{h + \eta(a_r + a_l)} \tag{91}$$

C_2 can be calculated from Eq. (90):

$$C_2 = -\eta a_l\left[\frac{a_r\frac{\partial p}{\partial y}h\eta + \frac{\partial p}{\partial y}\frac{h^2}{2} + \eta a_r\left(\tau_{C,r} + \tau_{C,l}\right) + \tau_{C,l}h}{h + \eta\left(a_r + a_l\right)}\right] \tag{92}$$

Substituting constants C_1 and C_2 into Eq. (80), the velocity along the y direction is:

$$v=\frac{\partial p}{\partial y}\frac{z^2}{2\eta}-z\left(\frac{\partial p}{\partial y}\frac{h}{2\eta}\frac{2\eta a_r+h}{h+\eta\left(a_r+a_l\right)}+\frac{a_r\tau_{C,r}-a_l\tau_{C,l}}{h+\eta\left(a_r+a_l\right)}\right)$$

$$-\frac{\partial p}{\partial y}\frac{h}{2\eta}\frac{2a_la_r\eta^2+ha_l\eta}{h+\eta\left(a_r+a_l\right)}-\frac{\eta a_ra_l\left(\tau_{C,r}+\tau_{C,l}\right)+a_l\tau_{C,l}h}{h+\eta\left(a_r+a_l\right)} \tag{93}$$

Using the Leibnitz rule for differentiation of integrals, the second term of Eq. (75) can be written as:

$$\int_0^h\frac{\partial v}{\partial y}dz=\frac{\partial}{\partial y}\int_0^h\rho v(z)dz-\rho v(h)\frac{\partial h}{\partial y} \tag{94}$$

Substituting equation of velocity (93) into the first part of Eq. (94) results in:

$$\int_0^h\rho v(z)dz=$$

$$=\frac{\partial p}{\partial y}\frac{\rho h^3}{6\mu}-\rho\left(\frac{\partial p}{\partial y}\frac{h^3}{4\eta}\frac{2\eta a_r+h}{h+\eta\left(a_r+a_l\right)}+\frac{h^2}{2}\frac{a_r\tau_{C,r}-a_l\tau_{C,l}}{h+\eta\left(a_r+a_l\right)}\right)-\frac{\partial p}{\partial y}\frac{\rho h^2}{2\eta}\frac{2a_la_r\eta^2+ha_l\eta}{h+\eta\left(a_r+a_l\right)}$$

$$-\rho\frac{\eta a_ra_l\left(\tau_{C,r}+\tau_{C,l}\right)h+a_l\tau_{C,l}h^2}{h+\eta\left(a_r+a_l\right)}=$$

$$-\frac{\partial p}{\partial y}\frac{\rho h^2}{12\eta}\left(\frac{h^2+4\eta h\left(a_r+a_l\right)+12a_la_r\eta^2}{h+\eta\left(a_r+a_l\right)}\right)-\frac{\rho h}{2}\frac{\left(a_r\tau_{C,r}+a_l\tau_{C,l}\right)h+2\eta a_ra_l\left(\tau_{C,r}+\tau_{C,l}\right)}{h+\eta\left(a_r+a_l\right)} \tag{95}$$

and for the term v(h)

$$\rho v\left(h\right)=\frac{\partial p}{\partial y}\frac{\rho h^2}{2\eta}-\rho\left(\frac{\partial p}{\partial y}\frac{h^2}{2\eta}\frac{2\eta a_r+h}{h+\eta\left(a_r+a_l\right)}+\frac{a_r\tau_{C,r}h-a_l\tau_{C,l}h}{h+\eta\left(a_r+a_l\right)}\right)-\frac{\partial p}{\partial y}\frac{\rho h}{2\eta}\frac{2a_la_r\eta^2+ha_l\eta}{h+\eta\left(a_r+a_l\right)}$$

$$-\rho\frac{\eta a_ra_l\left(\tau_{C,r}+\tau_{C,l}\right)+a_l\tau_{C,l}h}{h+\eta\left(a_r+a_l\right)}=\frac{\partial p}{\partial y}\frac{\rho h}{2\eta}\left(h-\frac{2\eta a_rh+h^2}{h+\eta\left(a_r+a_l\right)}-\frac{2a_la_r\eta^2+ha_l\eta}{h+\eta\left(a_r+a_l\right)}\right)=$$

$$=-\frac{\partial p}{\partial y}\frac{\rho h}{2\eta}\left(\frac{\eta a_rh+2a_la_r\eta^2}{h+\eta\left(a_r+a_l\right)}\right)-\rho\frac{a_r\tau_{C,r}h+\eta a_ra_l\left(\tau_{C,r}+\tau_{C,l}\right)}{h+\eta\left(a_r+a_l\right)} \tag{96}$$

Thus the second term of Eq. (75) is written in total:

$$\int_0^h \frac{\partial(\rho v)}{\theta y} dz = -\frac{\partial}{\partial y}\left[\frac{\partial p}{\partial y}\frac{\rho h^2}{12\eta}\left(\frac{h^2 + 4\eta h(a_r + a_l) + 12 a_l a_r \eta^2}{h + \eta(a_r + a_l)}\right)\right] - \frac{\partial}{\partial y}\left[\frac{\rho h}{2}\frac{(a_r\tau_{C,r} + a_l\tau_{C,l})h + 2\eta a_r a_l(\tau_{C,r} + \tau_{C,l})}{h + \eta(a_r + a_l)}\right] +$$

$$+\frac{\partial p}{\partial y}\frac{\partial h}{\partial y}\frac{\rho h}{2\eta}\left(\frac{\eta a_r h + 2 a_l a_r \eta^2}{h + \eta(a_r + a_l)}\right) + \rho\frac{a_r\tau_{C,r}h + \eta a_r a_l(\tau_{C,r} + \tau_{C,l})}{h + \eta(a_r + a_l)}\frac{\partial h}{\partial y} \quad (97)$$

For the third term of Eq. (75) the following is valid, as the squeeze motion only occurs:

$$\int_0^h \frac{\partial(\rho w)}{\theta z} dz = \rho w = \rho\frac{\partial h}{\partial t} \quad (98)$$

The final term of Eq. (75) is the accumulation ratio, as mentioned during the derivation of the Reynolds equation and is equal to:

$$\int_0^h \frac{\partial \rho}{\partial t} dz = \frac{\partial \rho}{\partial t} h \quad (99)$$

Substituting all the three terms for x, y and z directions in the Eq. (75) of continuity of flow the result is the Reynolds equation for slip conditions on the solid boundary.

$$\frac{\partial}{\partial x}\left(\frac{\rho h^2}{12\eta}\frac{\theta p}{\theta x}\frac{h^2 + 4\eta(a_l + a_r)h + 12\eta^2 a_l a_r}{h + \eta(a_l + a_r)}\right) + \frac{\partial}{\partial y}\left(\frac{\partial p}{\partial y}\frac{\rho h^2}{12\eta}\frac{h^2 + 4\eta h(a_r + a_l) + 12 a_l a_r \eta^2}{h + \eta(a_r + a_l)}\right) =$$

$$= \frac{U}{2}\frac{\partial}{\partial x}\left(\rho\frac{h^2 + 2\eta a_r h}{h + \eta(a_l + a_r)}\right) - U\rho\frac{\eta a_r}{h + \eta(a_l + a_r)}\frac{\partial h}{\partial x} + \frac{\rho h}{2\eta}\frac{\eta a_r h + 2 a_l a_r \eta^2}{h + \eta(a_l + a_r)}\left(\frac{\partial h}{\partial x}\frac{\partial p}{\partial x} + \frac{\partial p}{\partial y}\frac{\partial h}{\partial y}\right) +$$

$$+\frac{\partial}{\partial x}\frac{1}{2}\left(\rho\frac{h^2(a_l\tau_{C,l} - a_r\tau_{C,r}) + 2 a_l a_r \eta h(\tau_{C,l} - \tau_{C,r})}{h + \eta(a_l + a_r)}\right) + \rho\frac{\eta a_r a_l(\tau_{C,r} - \tau_{C,l}) + a_r\tau_{C,r}h}{h + \eta(a_l + a_r)}\frac{\partial h}{\partial x} -$$

$$-\frac{\partial}{\partial y}\left[\frac{\rho h}{2}\frac{(a_r\tau_{C,r} + a_l\tau_{C,l})h + 2\eta a_r a_l(\tau_{C,r} + \tau_{C,l})}{h + \eta(a_r + a_l)}\right] + \rho\frac{a_r\tau_{C,r}h + \eta a_r a_l(\tau_{C,r} + \tau_{C,l})}{h + \eta(a_r + a_l)}\frac{\partial h}{\partial y} + \frac{\partial(\rho h)}{\partial t} \quad (100)$$

Appendix B

Finite difference formulation of the Reynolds equation with the Elrod-Adams mass conservation algorithm.

The Reynolds equation with the Elrod-Adams mass conservation algorithm is presented in Eq. (101):

$$\frac{\partial}{\partial x}\left(\frac{g(\theta)\beta h^3}{12\eta}\frac{\partial\theta}{\partial x}\right)+\frac{\partial}{\partial y}\left(\frac{g(\theta)\beta h^3}{12\eta}\frac{\partial\theta}{\partial y}\right)=\frac{U}{2}\frac{\partial(\theta h)}{\partial x}+\frac{\partial(\theta h)}{\partial t} \tag{101}$$

Pressure Term

The terms of the pressure induced flow from Reynolds Eq. (101) are:

$$\frac{\partial}{\partial x}\left(\frac{\rho_c g(\theta)\beta h^3}{12\eta}\frac{\partial\theta}{\partial x}\right)+\frac{\partial}{\partial y}\left(\frac{g(\theta)\beta h^3}{12\eta}\frac{\partial\theta}{\partial y}\right) \tag{102}$$

According to Vijayaraghavan and Keith [9], the optimum way to handle the switch function g(θ), is the following:

$$g\frac{\partial\theta}{\partial x}=g\frac{\partial(\theta-1)}{\partial x}=\frac{\partial g(\theta-1)}{\partial x}-(\theta-1)\frac{\partial g}{\partial x} \tag{103}$$

In Eq. (103) the term $(\theta-1)\frac{\partial g}{\partial x}$ is always equal to zero, because outside the boundary between the active and cavitation regions g is constant (1 or 0), therefore $\partial g/\partial x=0$, whereas on the cavitation boundary, fraction θ is equal to unity, therefore (θ-1)=0. Consequently, the following is valid:

$$g\frac{\partial\theta}{\partial x}=\frac{\partial g(\theta-1)}{\partial x} \tag{104}$$

Inserting Eq. (104) in Eq. (102) and utilizing a half-step finite difference method:

$$\frac{\partial}{\partial x}\left(\frac{g(\theta)\beta h^3}{12\eta}\frac{\partial\theta}{\partial x}\right)=\frac{\partial}{\partial x}\left(\frac{\beta h^3}{12\eta}\frac{\partial g(\theta-1)}{\partial x}\right)=$$

$$\frac{\beta}{12\eta}\frac{h(i+1/2,j)^3\left.\frac{\partial g(\theta-1)}{\partial x}\right|_{i+1/2,j}-h(i-1/2,j)^3\left.\frac{\partial g(\theta-1)}{\partial x}\right|_{i-1/2,j}}{\Delta x} \tag{105}$$

The following operator may be used to calculate the quantities introduce in Eq. (105):

$$\left(\ \right)_{i\pm1/2}=\frac{\left(\ \right)_{i\pm1}+\left(\ \right)_{i}}{2} \tag{106}$$

Finally, Eq. (105), with the aid of Eq. (106) yields:

$$\frac{\partial}{\partial x}\left(\frac{g(\theta)\beta h^3}{12\eta}\frac{\partial\theta}{\partial x}\right)=\frac{\partial}{\partial x}\left(\frac{\beta h^3}{12\eta}\frac{\partial g(\theta-1)}{\partial x}\right)=\frac{\beta}{12\eta}\frac{h(i+1/2,j)^3\left.\frac{\partial g(\theta-1)}{\partial x}\right|_{i+1/2,j}-h(i-1/2,j)^3\left.\frac{\partial g(\theta-1)}{\partial x}\right|_{i-1/2,j}}{\Delta x}=$$

$$=\frac{\beta}{12\eta}\frac{h(i+1/2,j)^3\frac{g(i+1,j)(\theta(i+1,j)-1)-g(i,j)(\theta(i,j)-1)}{x(i+1)-x(i)}-h(i-1/2,j)^3\frac{g(i,j)(\theta(i,j)-1)-g(i-1,j)(\theta(i-1,j)-1)}{x(i)-x(i-1)}}{x(i+1/2)-x(i-1/2)}=$$

$$=\frac{\beta}{12\eta}\frac{h(i+1/2,j)^3\frac{g(i+1,j)(\theta(i+1,j)-1)-g(i,j)(\theta(i,j)-1)}{\Delta x}-h(i-1/2,j)^3\frac{g(i,j)(\theta(i,j)-1)-g(i-1,j)(\theta(i-1,j)-1)}{\Delta x}}{\Delta x}=$$

$$=\frac{\beta}{12\eta\Delta x^2}\left(h(i+1/2,j)^3\left(g(i+1,j)(\theta(i+1,j)-1)-g(i,j)(\theta(i,j)-1)\right)-h(i-1/2,j)^3\left(g(i,j)(\theta(i,j)-1)-g(i-1,j)(\theta(i-1,j)-1)\right)\right)=$$

$$=\frac{\beta}{12\eta\Delta x^2}\left((\theta(i+1,j)-1)g(i+1,j)h(i+1/2,j)^3-(\theta(i,j)-1)g(i,j)\left(h(i+1/2,j)^3+h(i-1/2,j)^3\right)+(\theta(i-1,j)-1)g(i-1,j)h(i-1/2,j)^3\right)=$$

$$=\frac{\beta}{12\eta\Delta x^2}\left(\theta(i+1,j)g(i+1,j)h(i+1/2,j)^3-\theta(i,j)g(i,j)\left(h(i+1/2,j)^3+h(i-1/2,j)^3\right)+\theta(i-1,j)g(i-1,j)h(i-1/2,j)^3\right)-$$

$$\frac{\beta}{12\eta\Delta x^2}\left(g(i+1,j)h(i+1/2,j)^3-g(i,j)\left(h(i+1/2,j)^3+h(i-1/2,j)^3\right)+g(i-1,j)h(i-1/2,j)^3\right) \tag{107}$$

The same procedure can be used for the pressure term in the y direction:

$$\frac{\partial}{\partial y}\left(\frac{g(\theta)\beta h^3}{12\eta}\frac{\partial\theta}{\partial y}\right)=$$

$$\frac{\beta}{12\eta\Delta y^2}\left(\theta(i,j+1)g(i,j+1)h(i,j+1/2)^3-\theta(i,j)g(i,j)\left(h(i,j+1/2)^3+h(i,j-1/2)^3\right)+\theta(i,j-1)g(i,j-1)h(i,j-1/2)^3\right)$$

$$-\frac{\beta}{12\eta\Delta y^2}\left(g(i,j+1)h(i,j+1/2)^3-g(i,j)\left(h(i,j+1/2)^3+h(i,j-1/2)^3\right)+g(i,j-1)h(i,j-1/2)^3\right) \tag{108}$$

Shear Term

The term of the shear induced flow of Eq. (101) is:

$$\frac{U}{2}\frac{\partial(\theta h)}{\partial x} \tag{109}$$

According to the Elrod-Adams model, the mass flux due to the velocity of the liner (Fig. 22) is given by the following equation:

$$(m_x)_{conv} = \rho_c \frac{U}{2}\left(\theta(i-1,j)h(i-1,j)(1-g(i-1,j)) + g(i-1,j)h(i-1,j) + g(i,j)g(i-1,j)\frac{h(i,j)-h(i-1,j)}{2}\right) \tag{110}$$

This algorithm is the result of the following three special cases:

a) If the upstream point is in the cavitation zone ($g(i-1,j)=0$), then, regardless of the downstream state:

$$(m_x)_{conv} = \rho_c \frac{U}{2}\theta(i-1,j)h(i-1,j)$$

b) If the upstream point is in the full film region ($g(i-1,j)=1$) and the downstream point is in the cavitation zone ($g(i,j)=0$):

$$(m_x)_{conv} = \rho_c \frac{U}{2}h(i-1,j)$$

c) If both points are in the full film region:

$$(m_x)_{conv} = \rho_c \frac{U}{2}\frac{h(i-1,j)+h(i,j)}{2}$$

Therefore, the shear flow term of Reynolds equation can be written in the following form:

$$\frac{U}{2}\frac{\partial(\theta h)}{\partial x}=\frac{1}{\rho_c}\frac{\partial\left(\frac{U}{2}\rho_c\theta h\right)}{\partial x}=\frac{1}{\rho_c}\frac{\partial(m_x)_c}{\partial x}=\frac{1}{\rho_c}\frac{\Delta(m_x)_c}{\Delta x}=$$

$$=\frac{U}{2}\frac{\left(\theta(i,j)h(i,j)(1-g(i,j))+g(i,j)h(i,j)+g(i+1,j)g(i,j)\frac{h(i+1,j)-h(i,j)}{2}\right)}{\Delta x}$$

$$-\frac{\left(\theta(i-1,j)h(i-1,j)(1-g(i-1,j))+g(i-1,j)h(i-1,j)+g(i,j)g(i-1,j)\frac{h(i,j)-h(i-1,j)}{2}\right)}{\Delta x}$$

$$=\frac{U}{2\Delta x}\left(\theta(i,j)h(i,j)(1-g(i,j))+g(i,j)h(i,j)+\frac{g(i+1,j)g(i,j)h(i+1,j)}{2}-\frac{g(i+1,j)g(i,j)h(i,j)}{2}\right)$$

$$-\frac{U}{2\Delta x}\left(\theta(i-1,j)h(i-1,j)(1-g(i-1,j))+g(i-1,j)h(i-1,j)+\frac{g(i-1,j)g(i,j)h(i,j)}{2}-\frac{g(i-1,j)g(i,j)h(i-1,j)}{2}\right)=$$

$$=\frac{U}{2\Delta x}\left[\theta(i,j)h(i,j)(1-g(i,j))-\theta(i-1,j)h(i-1,j)(1-g(i-1,j))-\frac{g(i-1,j)h(i-1,j)}{2}(2-g(i,j))\right]$$

$$+\frac{U}{2\Delta x}\left[-\frac{g(i,j)h(i,j)}{2}(g(i-1,j)-2+g(i+1,j))+\frac{g(i+1,j)g(i,j)h(i+1,j)}{2}\right]$$

$$=-\frac{U}{2\Delta x}\left[\theta(i-1,j)h(i-1,j)(1-g(i-1,j))-\theta(i,j)h(i,j)(1-g(i,j))+\frac{g(i-1,j)h(i-1,j)}{2}(2-g(i,j))\right]$$

$$-\frac{U}{2\Delta x}\left[\frac{g(i,j)h(i,j)}{2}(g(i-1,j)-2+g(i+1,j))-\frac{g(i+1,j)g(i,j)h(i+1,j)}{2}\right]$$

Squeeze film term

The squeeze film term can be written as:

$$\frac{\partial(\theta h)}{\partial t}=\theta\frac{\partial h}{\partial t}+h\frac{\partial\theta}{\partial t}=\theta(i,j)\Big|_t\frac{dh}{dt}+h(i,j)\frac{3\theta(i,j)\Big|_t-4\theta(i,j)\Big|_{t-1}+\theta(i,j)\Big|_{t-2}}{2\Delta t}=\theta(i,j)\Big|_t\left(\frac{dh}{dt}+\frac{3h(i,j)}{2\Delta t}\right)+h(i,j)\frac{-4\theta(i,j)\Big|_{t-1}+\theta(i,j)\Big|_{t-2}}{2\Delta t}$$

Terms dh/dt and $\partial\theta/\partial t$ of the previous equation are computed utilizing a second-order backward difference scheme.

Inserting all the above terms into Reynolds equation the result is the following:

$$\left[\frac{\beta}{12\eta\Delta x^2}g(i+1,j)h\left(i+1/2,j\right)^3\right]\theta(i+1,j)+\left[\frac{\beta}{12\eta\Delta x^2}g(i-1,j)h\left(i-1/2,j\right)^3+\frac{U}{2\Delta x}h(i-1,j)(1-g(i-1,j))\right]\theta(i-1,j)$$
$$+\left[\frac{\beta}{12\eta\Delta y^2}g(i,j+1)h\left(i,j+1/2\right)^3\right]\theta(i,j+1)+\left[\frac{\beta}{12\eta\Delta y^2}g(i,j-1)h\left(i,j-1/2\right)^3\right]\theta(i,j-1)$$
$$+\left[-\frac{\beta}{12\eta\Delta x^2}g(i,j)\left(h\left(i+1/2,j\right)^3+h\left(i-1/2,j\right)^3\right)-\frac{\beta}{12\eta\Delta y^2}g(i,j)\left(h\left(i,j+1/2\right)^3+h\left(i,j-1/2\right)^3\right)-\left(\frac{dh}{dt}+\frac{3h(i,j)}{2\Delta t}\right)\right]\theta(i,j)=$$
$$=\frac{\beta}{12\eta\Delta x^2}\left(g(i+1,j)h\left(i+1/2,j\right)^3-g(i,j)\left(h\left(i+1/2,j\right)^3+h\left(i-1/2,j\right)^3\right)+g(i-1,j)h\left(i-1/2,j\right)^3\right)$$
$$+\frac{\beta}{12\eta\Delta y^2}\left(g(i,j+1)h\left(i,j+1/2\right)^3-g(i,j)\left(h\left(i,j+1/2\right)^3+h\left(i,j-1/2\right)^3\right)+g(i,j-1)h\left(i,j-1/2\right)^3\right)$$
$$-\frac{U}{2\Delta x}\left[\frac{g(i-1,j)h(i-1,j)}{2}\left(2-g(i,j)\right)+\frac{g(i,j)h(i,j)}{2}\left(g(i-1,j)-2+g(i+1,j)\right)-\frac{g(i+1,j)g(i,j)h(i+1,j)}{2}\right]$$

$$+h(i,j)\frac{-4\,\theta(i,j)\big|_{t-1}+\theta(i,j)\big|_{t-2}}{2\Delta t} \qquad (111)$$